DESIGN, CONTROL, AND FAILURE MITIGATION FOR SEGMENTED SPACE TELESCOPES

A Dissertation

Presented to the Faculty of the Graduate School

of Cornell University

in Partial Fulfillment of the Requirements for the Degree of

Doctor of Philosophy

by

Jessica Ann Gersh-Range

May 2014

DESIGN, CONTROL, AND FAILURE MITIGATION FOR SEGMENTED SPACE TELESCOPES

Jessica Ann Gersh-Range, Ph.D.

Cornell University 2014

Future astrophysics missions will require the construction of larger space telescopes, which poses numerous technical challenges including: mirror stability, packaging and deployment, active mirror control, and segment actuator failure mitigation. To address these challenges, this dissertation presents the results of four research projects. The first project considers the problems of packaging and deployment and mirror stability, presenting a segmented mirror architecture in which the segments are connected edgewise by mechanisms analogous to damped springs. For low to intermediate stiffnesses, the stiffness and damping contributions from the mechanisms improve both the natural frequency and disturbance response of the segmented mirror. At higher stiffnesses, the segmented mirror performs comparably to or better than a monolith, with the modular design enabling on-orbit assembly and scalability.

The second project addresses the mirror stability challenge for cryogenic mirrors in particular, presenting flux-pinning mechanisms designed to increase the mirror stiffness and damping. These mechanisms consist of a collection of magnets and superconductors, and like flexures, preferentially allow motion in specific degrees of freedom. With typical stiffness and damping values on the order of $5,000$ N/m and 5 kg/s, respectively, these mechanisms provide modest improvements to the mirror performance.

The third project investigates improvements to mirror control algorithms for active space telescopes at L2. I show that the wavefront for these telescopes can be controlled passively by introducing scheduling constraints and describe the implementation of a predictive con-

troller designed to prevent the wavefront error from exceeding a desired threshold. This controller outperforms simpler algorithms even with substantial model error, achieving a lower wavefront error without requiring significantly more corrections.

The fourth project discusses how the effects of actuator failures can be mitigated by using the remaining segment actuators to optimize the pose of each affected segment. When one actuator fails, the affected segment can still attain a pose with zero wavefront error by exploiting the rotational symmetry of the primary. Monte Carlo simulations of many failures randomly distributed across an initially well-phased segmented primary show that more than 10% of the actuators must fail before the root-mean-square wavefront error degrades significantly.

BIOGRAPHICAL SKETCH

Jessica Gersh-Range is a Ph.D. candidate in Mechanical Engineering at Cornell University. She received a B.A. with Honors in Physics from Swarthmore College in 2006, with a minor in mathematics. Her research interests include space optical systems, which combines her physics and engineering background. Specific areas of interest include mirror segment actuators, mechanisms that enable on-orbit construction of large segmented space mirrors, active mirror control algorithms, cryogenic optics, and optics fabrication. Ms. Gersh-Range was the recipient of a NASA Graduate Student Researchers Program fellowship at Marshall Space Flight Center. She has also worked at the Space Telescope Science Institute as a Graduate Student.

To my family

ACKNOWLEDGEMENTS

First and foremost, I would like to thank the NASA Graduate Student Researchers Program and the Space Telescope Science Institute (STScI) for providing the incredible research opportunities that resulted in this work. I would also like to thank the members of my dissertation committee (Mason Peck, Gordon Stacey, James Lloyd, and Ephrahim Garcia) for the various insights they have offered during my time at Cornell.

The edgewise-connected mirror and flux-pinning mechanism projects presented in Chapters 1 and 2 were funded by NASA Grants NNX09AJ18H and NNX12AC61G, and they were products of a collaboration with Phil Stahl, Bill Arnold, and Dave Lehner at NASA's Marshall Space Flight Center (MSFC). I would also like to thank Charlie Griffith, for teaching the fine art of grinding and polishing Zerodur; and Bob Engberg and his team, for their support of the vibration measurements.

The mirror control and actuator failure mitigation projects presented in Chapters 3 and 4 resulted from collaborations at STScI. I would like to thank Marshall Perrin for his contributions to both projects, and Erin Elliot and Roeland van der Marel for their contributions to the actuator failure project. I would also like to thank Mark Clampin, Mike Menzel, and Mark McGinnis of Goddard Space Flight Center for reviewing the thermal and wavefront model.

It has been my pleasure to learn and research at MSFC and STScI, and I would like to offer my sincerest thanks to everyone who took the time to work with me and answer whatever questions I might have. I look forward to continuing to put the acquired skills and knowledge to use.

TABLE OF CONTENTS

PREFACE

At the dawn of the Space Age, scientists began using satellites to explore the universe over much of the electromagnetic spectrum. Since this time, space telescopes have proven to be an invaluable tool. They have been used to answer questions about the age and evolution of the universe, investigate black holes and dark matter, and study galaxy formation, among many other things. NASA's next flagship observatory, the James Webb Space Telescope (JWST), will be used to study topics including the ionization history of the universe, galaxy evolution, early stellar evolution, and the potential for life in nearby planetary systems. As space-based technology continues to evolve, it is expected that future astrophysics missions will address these topics in greater detail, using space telescopes with greater sensitivity and angular resolution. These missions will require the construction of larger space telescopes, which poses numerous technical challenges.

Some of these challenges, such as mirror stability, are directly related to the mirror size. In order for a telescope to take science data, the primary mirror surface error must remain below a fraction of the observing wavelength. However, for a fixed areal density, larger mirrors are increasingly flexible, and they are typically so lightly damped that vibrations can persist for some time. The challenge is even greater for cryogenic mirrors, which by their nature have negligible damping.

Other challenges, such as packaging and deployment, are related to the choice of launch vehicle. Fairing restrictions determine the maximum diameter of a monolithic mirror that can be launched–larger primaries must be segmented and either deployed or assembled on orbit.

While segmentation may enable larger primary mirrors, it introduces additional challenges. The performance of a segmented space telescope depends in part upon the ability to maintain the alignment and phasing of its primary mirror segments. Active control enables larger primaries by maintaining optical performance in the presence of perturbations, but active control algorithms for space telescopes are less mature than those for large ground telescopes due to differences in the wavefront control problems. Additionally, failures of the segment control actuators pose a threat to mission success since these actuators cannot be replaced or repaired on orbit, and it is desirable to prepare workarounds for any failures that do occur.

To address these challenges of segmented space mirror design, control, and failure mitigation, this dissertation presents the results of four research projects. The first project (Chapter 1) considers the problems of packaging and deployment and mirror stability. It presents a segmented mirror architecture in which the segments are connected edgewise by mechanisms analogous to damped springs. These mechanisms can be damped springs, flux-pinning mechanisms, virtual mechanisms, or any other device with the same basic behavior. Using a parametric finite-element model, I show that for low to intermediate stiffnesses, the stiffness and damping contributions from the mechanisms improve both the natural frequency and disturbance response of the segmented mirror. At higher stiffnesses, the mechanisms structurally connect the segments, leading to a segmented mirror that performs comparably to a monolith–or better, depending on the mechanism damping–with the modular design enabling on-orbit assembly and scalability.

The second project (Chapter 2) addresses the mirror stability challenge for cryogenic mirrors in particular, presenting flux-pinning mechanisms designed to increase the mirror stiffness and damping. These mechanisms consist of a collection of magnets and superconductors, and like flexures, they preferentially allow motion in specific degrees of freedom.

Motion in non-preferred degrees of freedom is resisted by a force analogous to a damped spring force, and the stiffness and damping can be adjusted independently. As an example, this chapter considers simple mechanisms consisting of an inexpensive magnet and a single superconductor. These mechanisms provide increasing resistance as the magnet and superconductor–or mirror segments attached to each–come closer to colliding. With typical stiffness and damping values on the order of $5,000$ N/m and 5 kg/s, respectively, these mechanisms also provide modest improvements to the mirror performance. Greater gains can be achieved by using stronger magnets or smaller separations, or by placing nonmagnetic conductive materials near the mechanism.

The third project (Chapter 3) investigates mirror control algorithms for active space telescopes at L2. The control problem for these telescopes requires weighing control costs against the benefits of correcting wavefront perturbations that are a predictable byproduct of the observing schedule, which is known and determined in advance. To improve the control algorithms for these telescopes, I have developed a model that calculates the temperature and wavefront evolution during a hypothetical mission, assuming the dominant wavefront perturbations are due to changes in the spacecraft attitude with respect to the sun. Using this model, I show that the wavefront can be controlled passively by introducing scheduling constraints that limit the allowable sun angles for an observation based on the observation duration and the mean telescope temperature. I also describe the implementation of a predictive controller designed to prevent the wavefront error from exceeding a desired threshold. This controller outperforms simpler algorithms even with substantial model error, achieving a lower wavefront error without requiring significantly more corrections. Though not explicitly designed for noise rejection, the predictive controller functions successfully even with measurement noise levels as high as half the correction threshold; the optical performance is limited primarily by the number of corrections required.

The fourth project (Chapter 4) discusses how the effects of actuator failures can be mitigated by using the remaining segment actuators to optimize the pose of each affected segment. This chapter considers the effect of actuator failures on the final wavefront error of a segmented space telescope whose primary mirror consists of 18 hexagonal segments, each controlled by a 3-6 hexapod. Optimization algorithms that minimize the wavefront error for single- and multiple-actuator failure cases are developed, and simulation results are presented. When one actuator fails, the affected segment can still attain a pose with zero wavefront error by exploiting the rotational symmetry of the primary. When two actuators fail, the resulting wavefront error depends upon which hexapod legs fail and at what lengths; cases where both legs of a bipod fail are an order of magnitude worse than other cases. Finally, Monte Carlo simulations of many failures randomly distributed across an initially well-phased segmented primary show that more than 10% of the actuators must fail before the root-mean-square wavefront error degrades significantly.

This dissertation is a compilation of four articles that have been or will be submitted to peer-reviewed journals. The material relating to actuator failure mitigation (Chapter 4 and corresponding parts of the Preface) has been published as J. Gersh-Range, E. Elliott, M. Perrin, and R. van der Marel, "Minimizing the Wavefront Error Degradation for Primary Mirror Segments with Failed Hexapod Actuators," *Optical Engineering* **51**(1), 011005 (2012).

CHAPTER 1

EDGEWISE CONNECTIVITY: AN APPROACH TO IMPROVING SEGMENTED PRIMARY MIRROR PERFORMANCE

1.1 Introduction

As future astrophysics missions require space telescopes with greater sensitivity and angular resolution, the corresponding increase in the primary mirror diameter presents numerous design challenges. Some of these challenges, such as packaging and deployment, are related to the choice of launch vehicle. Since fairing restrictions determine the maximum diameter of a monolithic mirror that can be launched, larger primaries must be segmented and either deployed or assembled on orbit. The 6.6 m primary for the James Webb Space Telescope, for example, consists of 18 segments mounted on a backplane that folds to satisfy the constraints of its 4.57 m diameter shroud.[1,2] While scaling this approach and developing more sophisticated packaging strategies may enable launching even larger future observatories,[3,4] an upper limit on the mirror diameter remains. Ultimately, there is a need for on-orbit assembly techniques that decouple the diameter from the choice of launch vehicle. Proposed methods include formation flight and electromagnetic formation flight, which treat the mirror as an array of free-floating segments and use active control to prevent collisions and maintain optical alignment.[5–7]

The material in this chapter has been submitted to a peer-reviewed journal as J. Gersh-Range, W. R. Arnold, Sr., and H. P. Stahl, "Edgewise connectivity: an approach to improving segmented primary mirror performance" (2014).

Additional challenges are related to the mirror itself. The image quality, for example, depends upon the stability of the mirror surface. In order to take science data, the surface error must remain below a specified tolerance even in the presence of vibrations, which can be excited by thermal snap, motion of an internal spacecraft mechanism, or the reaction wheels.[8–10] However, larger mirrors are not only more susceptible to vibrations, but they are also so lightly damped that the vibrations could persist for some time in the absence of control. Since the mirror flexibility scales as D^4/h^2, where D is the mirror diameter and h is the mirror thickness, the natural frequency is proportional to h/D^2, and the damping is close to pure material damping, with a damping ratio on the order of 0.01.[9,11] Methods for stiffening the mirror include increasing the thickness, which may not be possible if the additional mass conflicts with the launch vehicle restrictions, and actuating the segments.[12]

To address these challenges, we present a segmented mirror architecture in which the segments are connected edgewise by mechanisms analogous to damped springs, as shown in Figure 1.1. To compare the performance of this segmented mirror to that of a monolith with the same size and shape, we have developed a parametric finite-element model that calculates the mode shapes, natural frequencies, and disturbance response for either mirror, as outlined in Section 1.2. Using this tool, we show that the mechanisms can serve one of two functions: structurally connecting the segments or providing supplemental stiffness and damping (Sections 1.3-1.4). The particular application is determined by the mechanism stiffness, which affects the mirror at the segment level as well as globally (Section 1.3). For low to intermediate stiffnesses, the stiffness and damping contributions from the mechanisms improve both the natural frequency and the disturbance response of the segmented mirror.

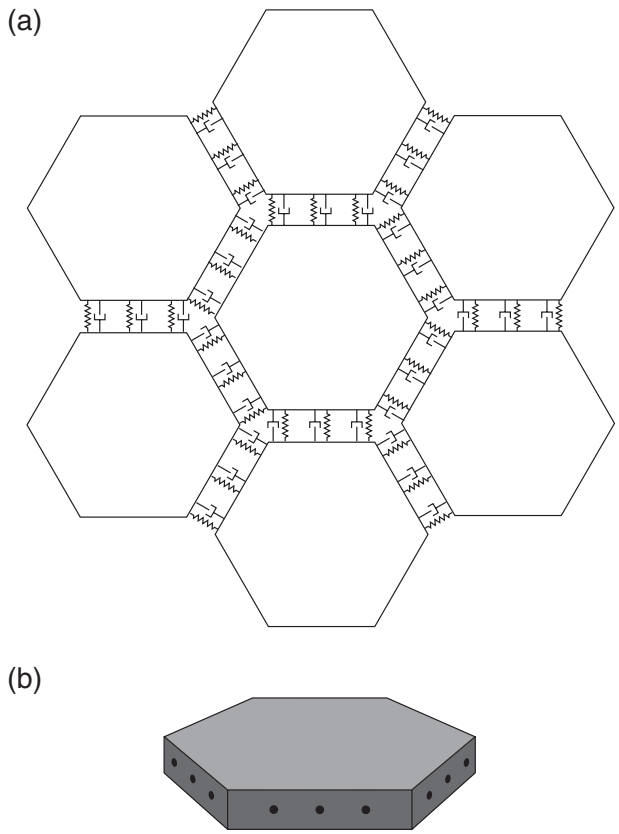

Figure 1.1: The edgewise-connected mirror. In this architecture, neighboring segments are connected by mechanisms analogous to damped springs, shown as spring-damper pairs in (a). These mechanisms are installed along the segment edges, as represented by dots in (b), and can consist of actual springs and dampers, flux-pinning mechanisms, or any other device with the same behavior. While the segments could be mounted to a backplane in addition, the question of segmented mirror mount design is beyond the scope of this paper.

At higher stiffnesses, the mechanisms structurally connect the segments, leading to a segmented mirror that performs comparably to or better than the monolith depending upon the amount of damping, with the modular design enabling on-orbit assembly and scalability (Section 1.4).

1.2 Mirror Model

To evaluate the performance of an edgewise-connected mirror, we consider the first natural frequency, which is directly related to the overall mirror stiffness, and the impulse response, which provides insights into the mirror stability. Since the performance is affected by the mirror geometry, mechanism properties, and mechanism placement, we have developed a parametric finite-element model in order to investigate how the mirror design affects the performance. As a basis for comparison, we consider the performance of a monolith of the same size and shape.

The finite-element model consists of submodels for the mirror, mount, and mechanisms. In the mirror model, a basic mirror is composed of rings of hexagonal segments and can be either segmented or monolithic depending upon how these segments are connected. For a segmented mirror, the segments are separated by a gap, and the edges of adjacent segments are connected at discrete locations by a collection of damped spring elements that represent the mechanisms [Figure 1.2(b)]. For a monolithic mirror, there is no gap between the segments, and the edges of adjacent segments are connected continuously by merging the coincident nodes [Figure 1.2(a)]. A specific mirror model is generated using a set of geometric parameters that includes the mirror diameter D, the size of the gap between the segments, the number of rings n_r, the mirror curvature, and the aspect ratio. For a segmented mirror, the number of mechanisms n_e along each edge, the mechanism placement, and the mechanism properties are additional parameters.

For simplicity, the mount model consists of two options: the mirror as a whole is either entirely unsupported or kinematically mounted at three edge nodes spaced by 120°. While

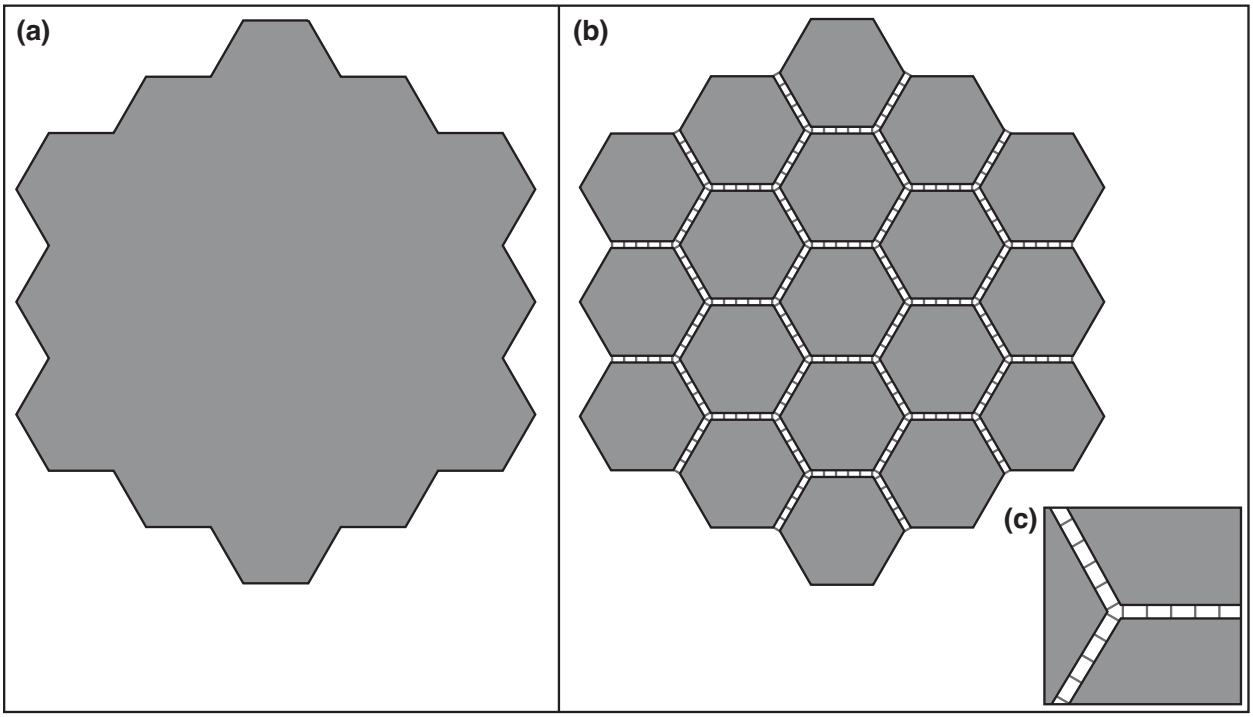

Figure 1.2: Mirror modeling. In the finite-element model, a mirror is composed of rings of hexagonal segments, with the connectivity determining whether the mirror is monolithic or segmented. For a monolithic mirror (a), the segments are connected continuously along the edges, while for a segmented mirror (b), the segments are connected at discrete locations by collections of damped springs that represent the mechanisms (c).

each segment could be mounted on a backplane in addition to being connected edgewise, the problem of segmented mirror mount design is beyond the scope of this paper.

The mechanism model represents each mechanism as a collection of damped springs. As an example, we consider a case in which all of the important dynamics can be captured using four collocated single-degree-of-freedom damped springs. Three of these damped springs correspond to translations parallel and perpendicular to the mirror edge, with the fourth corresponding to bending. It is assumed that while the damping is isotropic, the stiffness is not: the stiffness for perpendicular translation, $k_\perp$, is twice that for parallel translation, $k_\parallel$, and directly proportional to the bending stiffness, k_b. This particular mechanism model can

be used to describe flux-pinning mechanisms,[13] an actual collection of damped springs, or any other mechanism with the same behavior. The model also applies to the case of virtual mechanisms, in which sensors detect the relative motion between segments, actuators resist or correct this motion, and a control algorithm determines the appropriate actuator response.

In the simulations that follow, we consider a baseline 15 m mirror with two rings of segments, six mechanisms per edge, and an aspect ratio of 100, and we vary individual design parameters to determine their effects on the mirror performance. Since the natural frequency is directly proportional to the mirror thickness, we consider aspect ratios from 80 to 120; this range is expected to cover the spectrum of conservatively thick to aggressively thin designs.[14] To examine the importance of the mechanism stiffness, we consider $k_\perp$ values ranging from 10 to 10^9 N/m. At the upper end of this range, k_b is comparable to the approximate plate constant, the bending stiffness of a circular plate with the same diameter and material properties as the monolithic mirror. The limiting case of infinitely stiff mechanisms is also considered by using the CERIG command in ANSYS.[15] Similarly, to examine the importance of the mechanism damping, we consider values ranging from 0 to 10^6 kg/s.

Since the total stiffness and damping contributions from the mechanisms depend on the total number of mechanisms N_{mech} in addition to the individual mechanism properties, we also consider parameters that affect this number. In the edgewise-connected mirror, the total number of mechanisms depends upon the number of mechanisms n_e along each edge as well as the number of edge connections. There are two types of edge connections: connections between segments in the same ring and connections between segments in neighboring rings. As illustrated in Figure 1.3, for the ith ring, there are $6i$ sets of edge connections within the ring and $6(2i-1)$ sets of connections to ring $i-1$. As a result, there are $9n_r^2 + 3n_r$ sets of

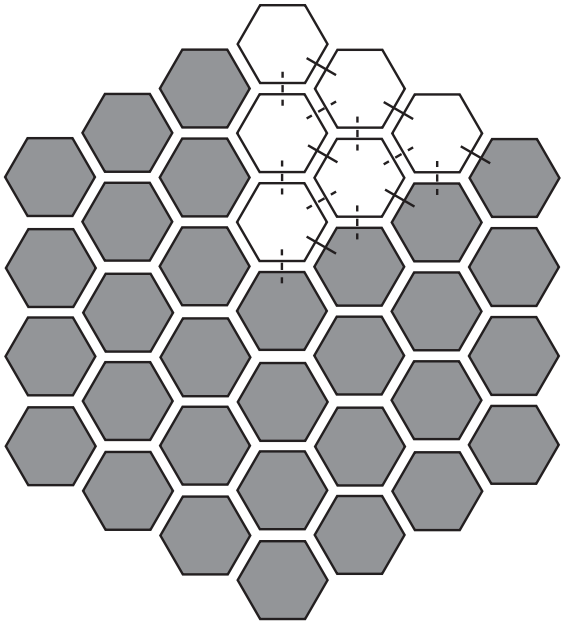

Ring Number	1	2	3	*i*
—— Sets of Edge Connections Within a Ring	6(1)	6(2)	6(3)	6(*i*)
- - - Sets of Edge Connections to the Previous Ring	6(1)	6(3)	6(5)	6(2*i*-1)

Figure 1.3: Mechanism totals by ring number. The total number of mechanisms depends upon the number of mechanisms used to connect a pair of adjacent edges, n_e, as well as the number of edge pairs. For ease of counting, the edge pairs are divided into two categories: in-ring pairs, for segments in the same ring, and cross-ring pairs, for segments in rings i and $i-1$. For a mirror with n_r rings, there are $9n_r^2 + 3n_r$ pairs, for a total of $n_e(9n_r^2 + 3n_r)$ mechanisms.

edge connections within the entire mirror, and the total number of mechanisms is given by

$$N_{mech} = n_e(9n_r^2 + 3n_r). \tag{1.1}$$

Since the total number of mechanisms depends on n_e, we consider 3 to 8 mechanisms per edge. Similarly, since the total number depends on n_r, we consider 1 to 4 rings; these ring numbers correspond to segments that are between 1 and 5 meters flat-to-flat, a range that includes sizes within current manufacturing capabilities as well as sizes that require technology development.[5]

1.3 Relating Mirror Motions to Mechanism Applications

When mirror segments are connected edgewise by springlike mechanisms, the overall stiffness along the segment edges affects the mirror behavior both globally and at the segment level. The edge stiffness is determined by the mechanism stiffness and the number of mechanisms along each edge, and it influences the first natural frequency as well as the motion of the segments, which can move as a unit or as individual rigid bodies. These different segment motions correspond to different mechanism applications: for sufficiently high edge stiffnesses, the mechanisms serve as structural attachments between the segments, with the segments moving as a cohesive unit. For lower edge stiffnesses, the mechanisms provide supplemental stiffness and damping even if the segments move as individual rigid bodies. To understand the conditions under which the mechanisms are suited for each purpose, we have conducted a series of parameter studies that investigate the relationship between the segmented mirror design and the resulting behavior.

The edge stiffness is affected by two main factors: the number of connections between adjacent mirror segments and the equivalent stiffness of all the mechanisms along the edge. These factors are controlled by two of the design parameters, the number of mechanisms along an edge and the mechanism stiffness, but they are not always adjusted independently. While the number of connections is directly related to the number of mechanisms, adding a mechanism also increases the equivalent stiffness. However, the effect that increasing the connectivity has on the mirror behavior can be isolated by considering the case of infinitely stiff mechanisms since in this limit adding mechanisms increases the number of connections without affecting the equivalent stiffness. Similarly, the effect of increasing the equivalent stiffness can be isolated by fixing the number of mechanisms and varying the mechanism

stiffness.

As Figure 1.4 shows, the equivalent stiffness is the dominant factor in determining the global mirror behavior. Although replacing the continuously connected edges of the monolith with discretely connected edges lowers the natural frequency, the effect is minimal. Even with as few as three mechanisms per edge, the frequency in the infinite-stiffness case is within 4% of the monolithic value, and it asymptotes to the monolithic value as the number of mechanisms increases. This asymptotic behavior is to be expected since the discrete connectivity approaches continuity in the limit of infinitely many mechanisms per edge. By comparison, decreasing the mechanism stiffness can decrease the frequency by orders of magnitude, and as expected, increasing the number of mechanisms increases the frequency. The same trends are observed whether the mirror is conservatively thick or aggressively thin.

One particularly significant result is that the frequency curves cluster as k_b approaches the approximate plate constant. As shown in Figure 1.5, a plot of the frequency as a function of mechanism stiffness divides into three regions. In the low- and intermediate-stiffness regions, the frequency increases as approximately the square root of the stiffness, but in the high-stiffness region, the increase is much slower. This result suggests that while aggressively increasing the bending stiffness may be beneficial in the low- and intermediate-stiffness regimes, it may not be worthwhile in the high-stiffness regime, especially if significant cost is involved.

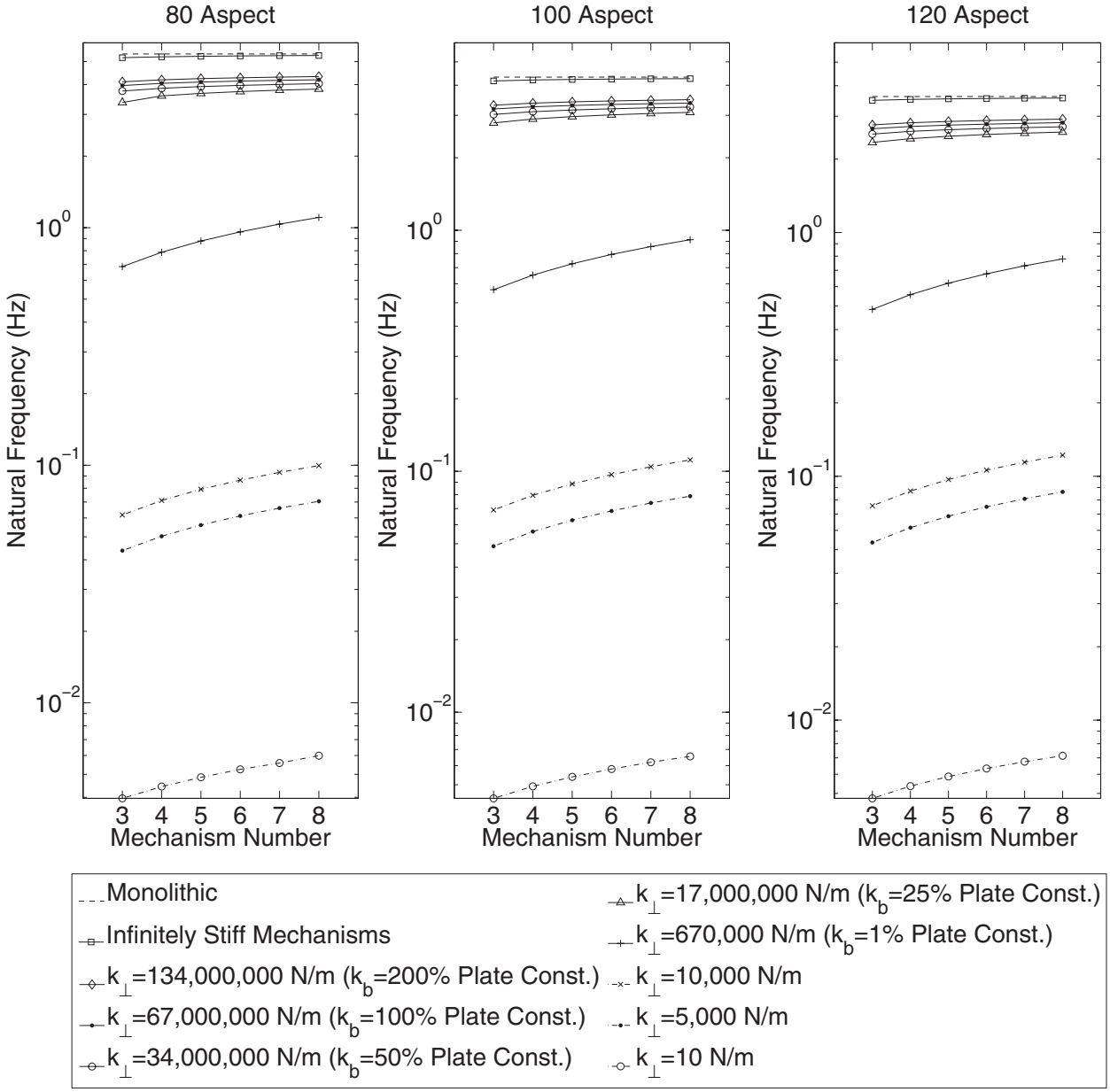

Figure 1.4: The first natural frequency as a function of aspect ratio, mechanism number, and mechanism stiffness.

Figure 1.5: Mechanism stiffness regimes and the corresponding segment motion. The mechanism stiffness affects the mirror behavior globally and at the segment level. For low-stiffness mechanisms (A), the segments conform to the mode shape by tilting as individual rigid bodies. For intermediate-stiffness mechanisms (B), the segments start to move as a unit while still tilting as individual rigid bodies. In these cases, the mechanisms are a source of supplemental stiffness and damping, and the natural frequency is approximately proportional to the square root of the mechanism stiffness. For high-stiffness mechanisms (C), the segments bend as a cohesive unit, indicating that the mechanisms serve as structural attachments between the segments. In this regime, increasing the mechanism stiffness has a minimal effect on the natural frequency. The limiting case of infinitely stiff mechanisms (D) is shown for reference.

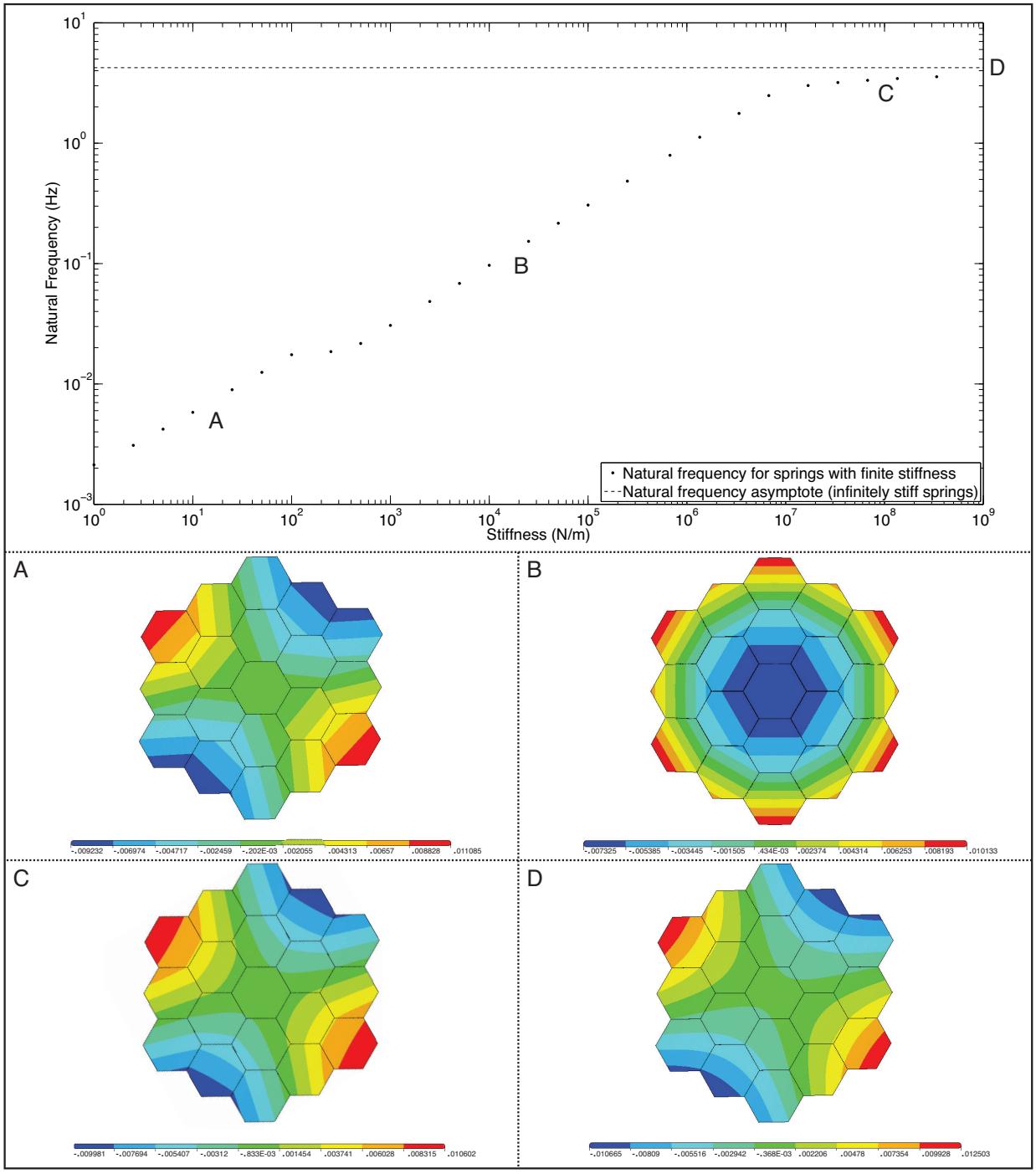
Natural Frequency (Hz)
Stiffness (N/m)
A
B
C
D
Natural frequency for springs with finite stiffness
Natural frequency asymptote (infinitely stiff springs)
-.009232 -.006974 -.004717 -.002459 -.202E-03 .002055 .004313 .00657 .008828 .011085
-.007325 -.005385 -.003445 -.001505 .434E-03 .002374 .004314 .006253 .008193 .010133
-.009981 -.007694 -.005407 -.00312 -.833E-03 .001454 .003741 .006028 .008315 .010602
-.010665 -.00809 -.005516 -.002942 -.368E-03 .002206 .00478 .007354 .009928 .012503

The transitions from one stiffness regime to the next correspond to changes in the segment motion, as evidenced by changes in the mode shapes. In the low-stiffness regime, the mode shape contours are straight across the segments and discontinuous across the segment boundaries, which indicates that the segments conform to the mode shape by tilting as individual rigid bodies. In the high-stiffness regime, the contours curve within a segment and are continuous across the boundaries, indicating that the segments bend as a single, cohesive unit. In between these cases, in the intermediate-stiffness regime, the contours are straight across the segments and the mode shape has shifted so that the contours are continuous across the segment boundaries. In this case, the segments move as a unit while still tilting as individual rigid bodies. These results suggest that the mechanisms function as structural attachments in the high-stiffness regime and as supplemental sources of stiffness and damping in the low- and intermediate-stiffness regimes.

1.4 Mirror Performance Studies

One important performance metric for a primary mirror is the settling time required after disturbances induce vibration. Since the mirror surface error must remain below a specified limit during science observations, time spent excessively vibrating reduces the observatory efficiency. To evaluate the performance of an edgewise-connected mirror relative to its equivalent monolith, we consider the time history of the root-mean-square surface error after an impulse disturbance is applied to one of the supports. This type of disturbance could arise from thermal snap, as seen on Hubble,[8,9] or other sources, including motions of internal spacecraft mechanisms such as tape recorders or filter wheels.[9,10]

For the edgewise-connected mirror, the disturbance response depends upon the total stiffness and damping contributions from the mechanisms. These contributions are affected by both the individual mechanism properties and the total number of mechanisms. While the total number of mechanisms can be adjusted by changing either the number of mechanisms n_e along each edge or the number of rings n_r, only the number of rings will be considered since the mechanism number increases quadratically with n_r but only linearly with n_e, as shown in Equation (1.1).

The mechanism stiffness primarily affects the response by determining the strength of the connections between the segments. For high-stiffness mechanisms, which serve as structural attachments, the connections are strong enough for the segments to move as a unit, while for lower-stiffness mechanisms, the connections can be much weaker. The difference in connection strength translates into a difference in the ease with which disturbances propagate across the mirror surface, with stronger connections corresponding to increased propagation. As a result, higher stiffnesses lead to larger disturbance responses, as shown in Figure 1.6.

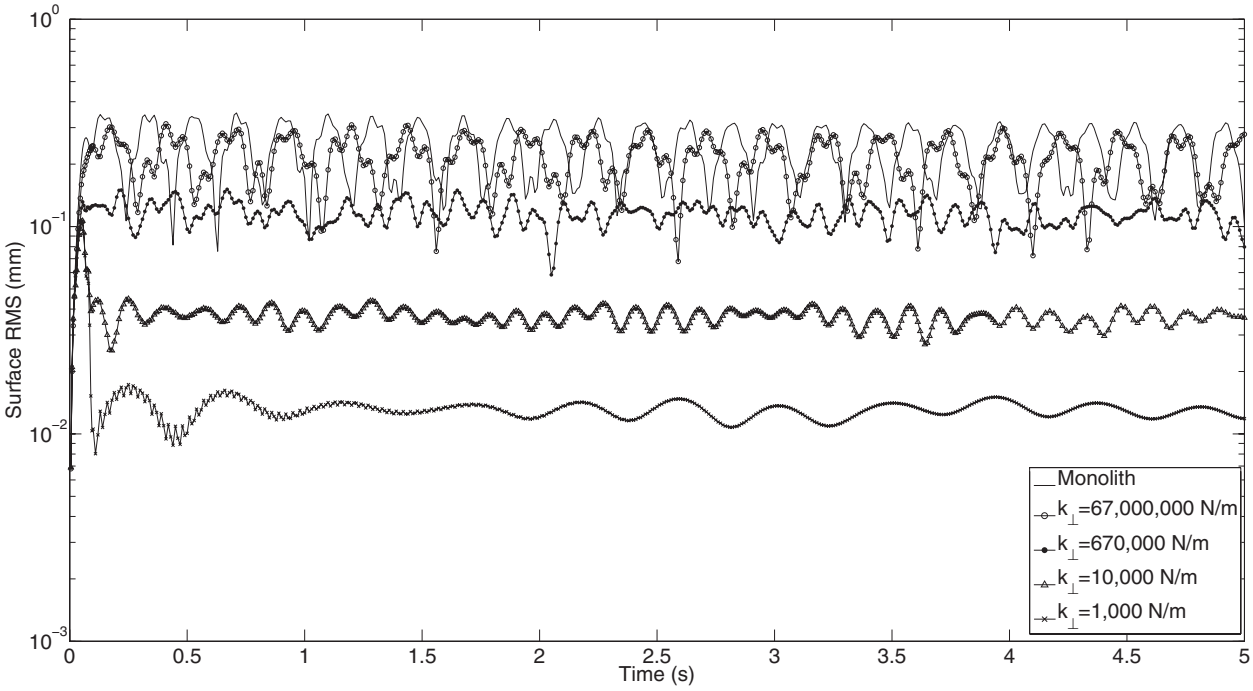

Figure 1.6: The effects of mechanism stiffness on the impulse response.

Since the stiffness affects the disturbance propagation, mechanisms that serve as structural attachments have different response characteristics than mechanisms that serve as supplemental sources of stiffness and damping. To examine these differences, we consider mechanisms for each application, with high-stiffness mechanisms representing the structural application and intermediate-stiffness mechanisms representing the supplemental application. As shown in Figure 1.7, four basic responses are possible. With high-stiffness mechanisms, the edgewise-connected mirror has a disturbance response comparable to or better than that of the monolith. In the low-damping case, the response oscillates with approximately the same magnitude and minimal decay, and in the high-damping case, the response improves noticeably, oscillating at a single frequency and decaying by nearly an order of magnitude in only five seconds. With intermediate-stiffness mechanisms, the edgewise-connected mirror has a response at least an order of magnitude lower than that of the monolith due to the decreased disturbance propagation. In the low-damping case, the response varies little

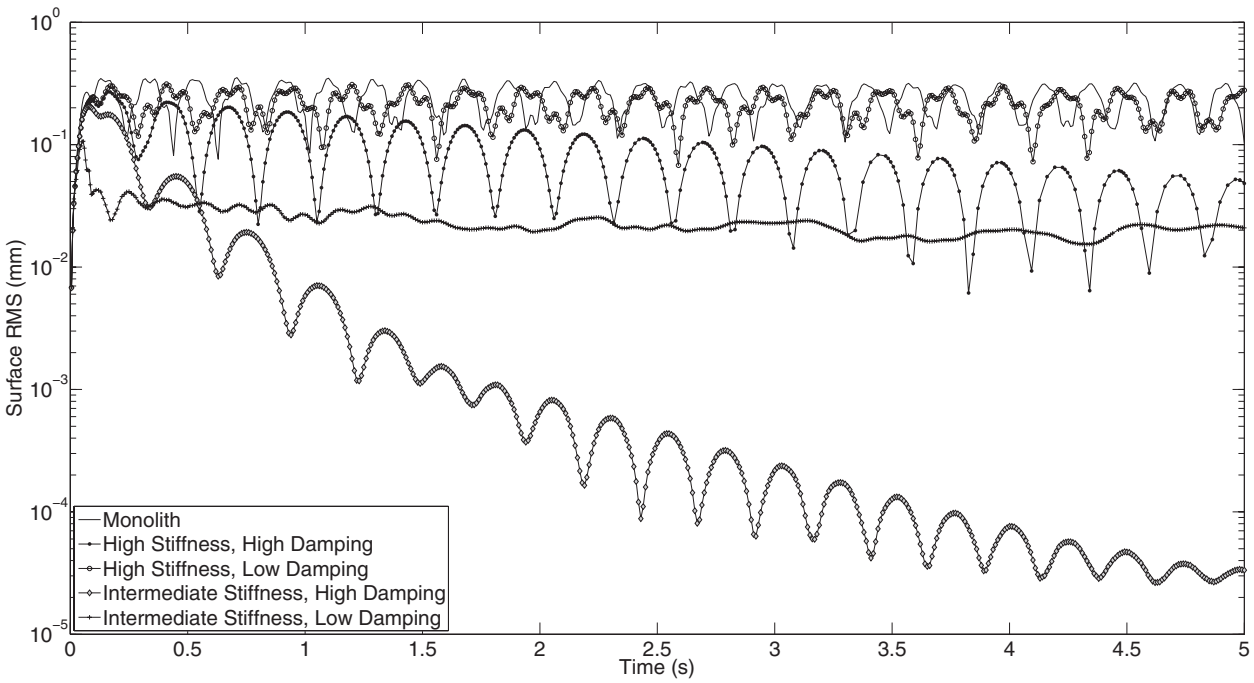

Figure 1.7: Limiting cases for the impulse response.

over five seconds, while in the high-damping case, the response decays rapidly, decreasing by several orders of magnitude.

While increasing the mechanism damping generally increases the decay rate, the amount of change depends upon the mechanism stiffness. Since disturbances propagate less effectively in the intermediate-stiffness cases, increasing the damping has a more pronounced effect [Figure 1.8(a)]. With very high damping, the dampers also begin to connect the segments. In Figure 1.8, the optimal damping for the intermediate-stiffness mechanisms is on the order of $100,000$ kg/s since the resulting response has the quickest decay without any oscillation. With additional damping, the response has a larger initial transient and oscillates with an amplitude comparable to that of the monolith response, indicating that the dampers are connecting the segments. In the high-stiffness cases, the increased connection strength is less apparent since the segments are already connected strongly [Figure 1.8(b)].

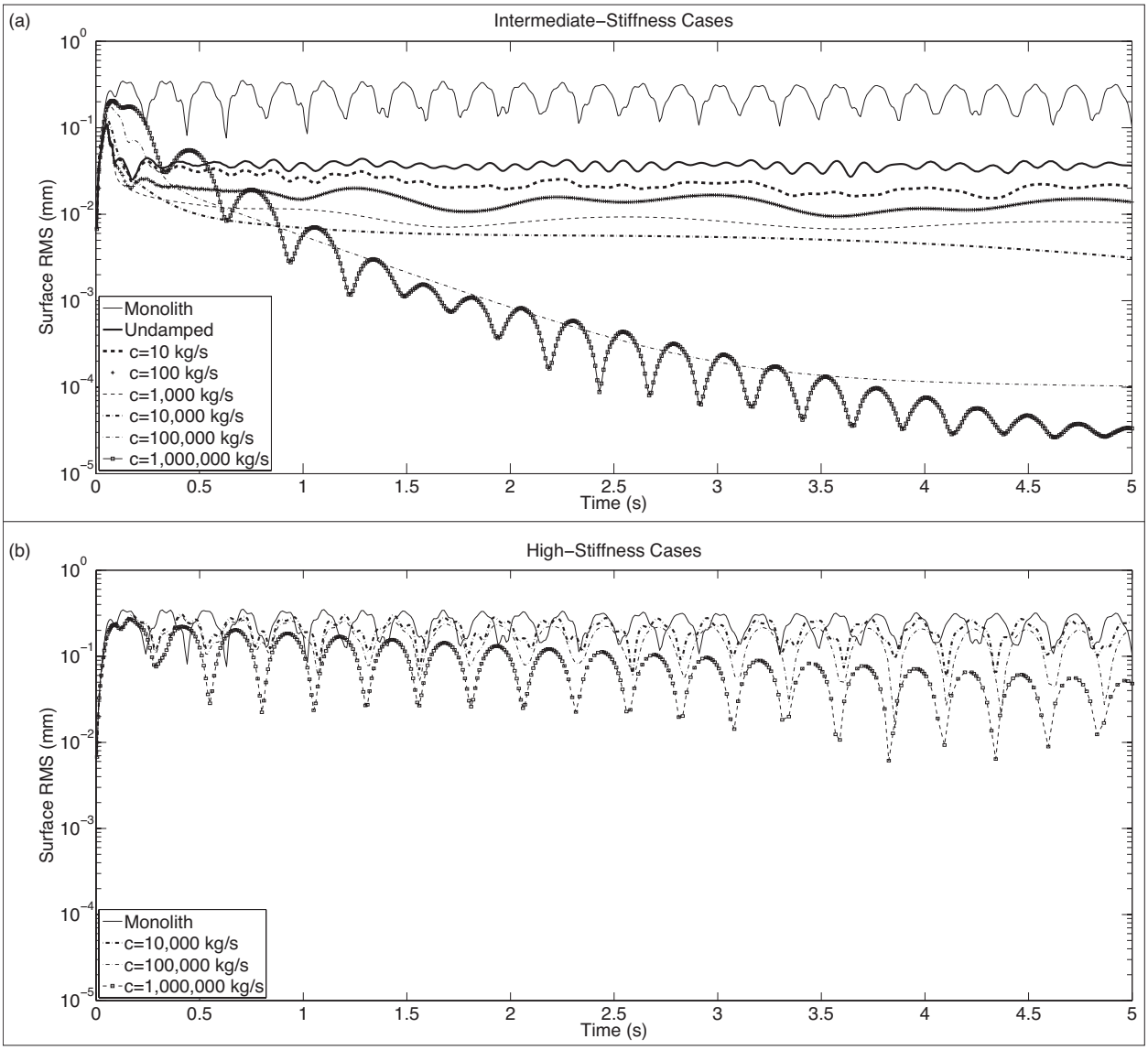

Figure 1.8: The effects of damping on the impulse response for intermediate- and high-stiffness mechanisms.

The effects of varying the ring number also depend upon the mechanism stiffness. In the high-stiffness cases, the ring number primarily affects the decay rate. With low damping, the responses are all comparable to that of the monolith [Figure 1.9(a)], and with high damping, the responses generally decay faster for higher ring numbers [Figure 1.9(c)]. In the intermediate-stiffness cases, the ring number affects both the decay rate and the disturbance propagation. As the ring number increases, the mirror is divided into a larger number of weakly-connected segments, decreasing the ease with which disturbances propagate across the mirror. As a result, the magnitude of the response decreases as the ring number increases [Figure 1.9(b)]. With high damping, the responses also decay more rapidly for higher ring numbers as the decreased disturbance propagation and increased damping combine to eliminate vibration quickly [Figure 1.9(d)].

While the mechanism properties and ring number all affect the final response, the selection of which parameters to increase will depend upon the cost and mechanism application. Increasing the number of rings from two to three, for example, more than doubles the number of mechanisms, but the number of segments and the number of segment types double as well, adding complexity to the design. For performance comparable to a monolith, high-stiffness mechanisms must be used, and increasing the mechanism damping or ring number improves the disturbance response. For mechanisms serving as supplemental sources of stiffness and damping, increasing the ring number or mechanism damping improves the disturbance response, but excessively high damping can lead to increased disturbance propagation.

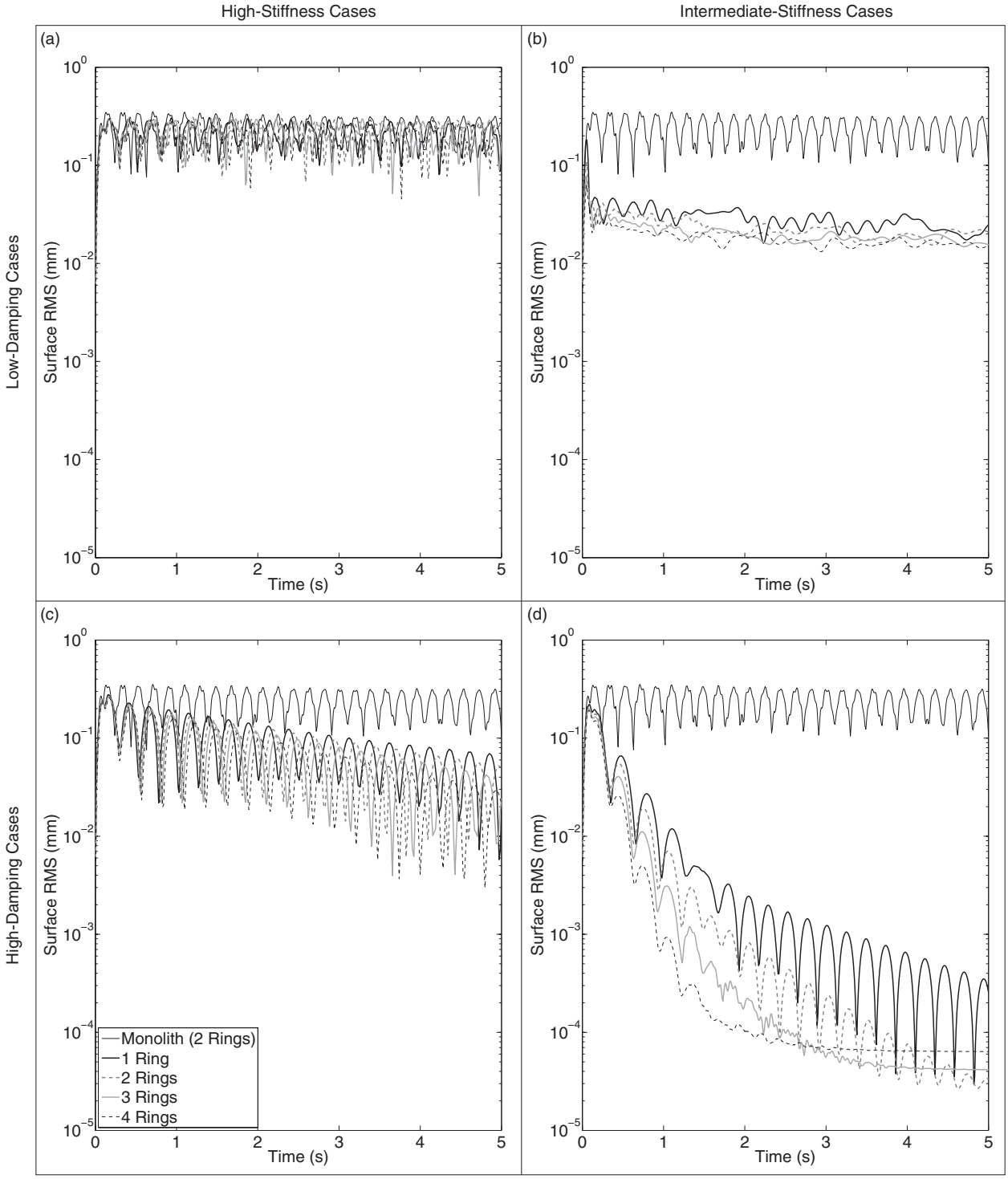

Figure 1.9: The effects of ring number on the impulse response for various mechanism cases.

1.5 Summary

While increasing the primary mirror diameter presents challenges related to packaging and deployment and mirror stability, these challenges can be addressed by using a segmented mirror architecture in which the segments are connected edgewise by mechanisms analogous to damped springs. Depending on the stiffness, these mechanisms function as either structural attachments between the segments or supplemental sources of stiffness and damping. For sufficiently high stiffnesses, the mechanisms cause the segments to move as a cohesive unit without requiring any other means of connecting the segments, such as via a backplane. In this case, the segmented mirror is dynamically comparable to a monolith, with the advantage that it can be assembled on orbit. With the additional damping provided by the mechanisms, the segmented mirror can also outperform the monolith, requiring less time to settle after vibrations are excited. For lower stiffnesses, the mechanisms may not be sufficiently strong to serve as the only connections between the segments, but the stiffness and damping contributions still improve the natural frequency and impulse response. The effects of adding a backplane are beyond the scope of this paper and may be explored in future simulations.

In general, the segmented mirror performance depends upon the total stiffness and damping contributions from the mechanisms, which are affected by the individual mechanism properties as well as the total number of mechanisms. While the mechanism stiffness is primarily useful for determining the mechanism application, increasing the stiffness also increases the natural frequency and the magnitude of the impulse response. Increasing the damping generally reduces the settling time, although excessively aggressive dampers can structurally connect the segments as well. While adjusting the ring number affects the total

stiffness and damping contributions, it also affects the ease with which disturbances propagate through the mirror. This effect is most noticeable if low- or intermediate-stiffness mechanisms are used since increasing the ring number divides the mirror into a larger number of weakly connected segments, decreasing the disturbance propagation. The choice of which parameters to vary to obtain the desired mirror characteristics will depend upon the mechanism application and overall cost, which will be the subject of future investigation.

CHAPTER 2

FLUX-PINNING MECHANISMS FOR IMPROVING CRYOGENIC SEGMENTED MIRROR PERFORMANCE

2.1 Introduction

Large cryogenic space telescopes may provide a means of answering several compelling astrophysics questions, but the required increase in the primary mirror diameter presents numerous technical challenges. Proposed investigations of early star formation, planetary system evolution, and the presence of large organic molecules in interstellar disks, for example, require a 10 to 16 m class far-IR to submillimeter space telescope; in this wavelength range, atmospheric extinction precludes ground-based measurements except within the several submillimeter windows, and existing space telescopes suffer from source confusion.[16–19] It is also expected that high-resolution far-IR observations will lead to new discoveries, possibly concerning the emergence of cosmic structure.[19,20] However, for an observatory to obtain an angular resolution in the far-IR that is comparable to Hubble's resolution in the visible, its diameter must be on the order of 1 km.[20] By comparison, Herschel, the largest space telescope to operate in the far-IR to submillimeter range, has a primary diameter of 3.5 m.[21] As the primary mirror diameter of future cryogenic observatories increases, maintaining a stable wavefront becomes increasingly challenging since the first natural frequency decreases as the diameter squared, the material damping is negligible, and other common damping

The material in this chapter has been submitted to a peer-reviewed journal as J. Gersh-Range, W. R. Arnold, Sr., D. Lehner, and H. P. Stahl, "Flux-pinning mechanisms for improving cryogenic segmented mirror performance" (2014).

methods break down at low temperatures.[9,11,22–24]

Although large stiff precision structures are considered an enabling technology for large cryogenic mirrors,[25] an alternative approach to increasing mirror stability is to use an edgewise-connected architecture. In this approach, mechanisms analogous to damped springs are placed along the edges of the primary mirror segments. The stiffness and damping contributions from the mechanisms reduce the requirements for the supporting structure, and if the mechanisms are sufficiently stiff, the segmented mirror performs comparably to a monolith even if the mechanisms are the only structural connections to the segments.[26] While the mechanisms can be a collection of damped springs or any other device with similar behavior, flux-pinning mechanisms are uniquely suited for cryogenic mirrors.

Unlike mechanical devices, which can have problems with lubrication, CTE matching, and thermal snap, flux-pinning mechanisms operate best at cryogenic temperatures. These passively stable, non-contacting mechanisms consist of a collection of magnets and type II superconductors, and require only low temperatures; no power is needed other than the minimal amount, if any, necessary for cooling. Like a flexure, a flux-pinning mechanism preferentially allows motion in specific degrees of freedom, which depend upon the mechanism design, as described in Section 2.2. Motion in the non-preferred degrees of freedom is resisted by a force analogous to a damped spring force, and the stiffness and damping can be adjusted independently. These mechanism properties depend upon the choice of magnets, the separation between the magnets and superconductors, and the presence of nonmagnetic conductive materials, such as aluminum.

As an example, we consider simple mechanisms consisting of an inexpensive magnet and a single superconductor separated by distances on the order of 1 mm (Sections 2.3-2.4). These

mechanisms can be trained to follow a particular deflection pattern when loaded, and they provide increasing resistance the closer the magnet and superconductor – or mirror segments attached to each – come to colliding. Typical stiffness and damping values are on the order of 5,000 N/m and 5 kg/s, respectively (Section 2.3). As shown in Section 2.4, mechanisms with these values provide modest improvements to the performance of an edgewise-connected mirror. Greater gains can be achieved by using stronger magnets or smaller separations, or by placing nonmagnetic conductive materials near the mechanism.

2.2 Flux-Pinning Mechanisms

Flux pinning, a physical interaction between a magnet and a type II superconductor, is analogous to a noncontacting damped spring force. This force is due to the presence of impurities that allow the magnetic field to penetrate into the superconductor material. As the superconductor cools below its critical temperature (approximately 90 K for YBCO, yttrium barium copper oxide[27]), the magnetic field lines are "frozen" in place; motions that change the magnetic field distribution inside the superconductor induce supercurrents that oppose the change. As a result, the relative orientation and position of the magnet and superconductor are passively stabilized in every direction that has a magnetic field gradient.

A useful conceptual model is the frozen-image model, which explains the forces between a magnet and a type II superconductor by replacing the superconductor with two image magnets.[28] The first image magnet, called the mobile image, is a reflection of the permanent magnet across the superconductor surface (Figure 2.1). This image moves as the permanent magnet moves, and since the two magnets have opposite moments, the interaction between

them is repulsive. The second image magnet, called the frozen image, is stationary. This image is almost a perfect reflection of the permanent magnet at the time the superconductor cooled below its critical temperature; the orientation and position of the frozen image are reflections of the orientation and position of the permanent magnet at this time, but the magnetic moment is in the same direction as that of the permanent magnet. The force on the permanent magnet is the sum of the forces due to each image magnet. As a result, the permanent magnet is in equilibrium when it is in its initial orientation and position since the forces from the images cancel. As the magnet moves closer to the superconductor, the force from the mobile image dominates, and the magnet is repelled. Similarly, as the magnet moves further from the superconductor, the force from the frozen image dominates, and the magnet is attracted.

For small motions, the force between the magnet and superconductor is analogous to a damped spring force, with the stiffness and damping determined by a variety of factors including the choice of magnet and superconductor, the separation during cooling, and the presence of conductive materials.[29–31] For a cylindrical magnet levitated over a cylindrical superconductor, the stiffness for motions perpendicular to the magnet-superconductor interface has been determined empirically to be approximately twice the stiffness for motions parallel to the interface,[32,33] and the stiffness increases nearly exponentially as the cooling separation decreases.[29] Stiffer interfaces result from using stronger magnets, stronger superconductors, and smaller separations. Additionally, the amount of damping can be increased independently by placing nonmagnetic conductive materials, such as aluminum, near the interface. Previous experiments have demonstrated that placing aluminum near the mechanism can increase the damping substantially, altering the response from imperceptibly damped to strongly overdamped.[29]

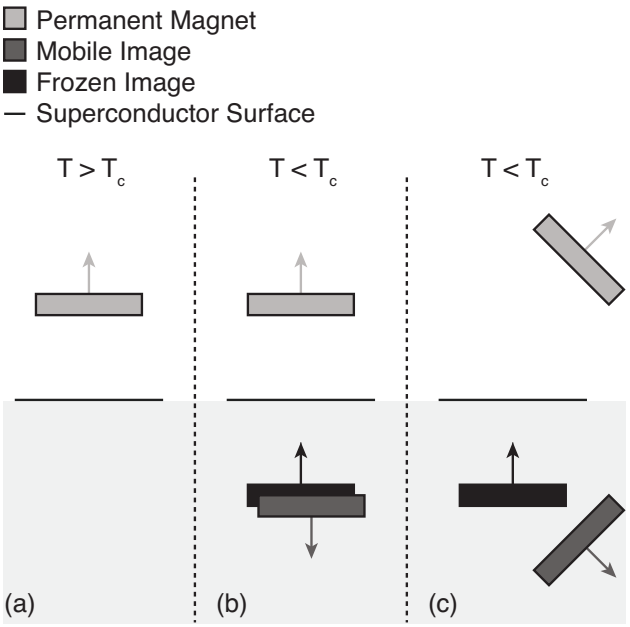

Figure 2.1: Image model for flux pinning. In this model, flux pinning is described as the interaction between the permanent magnet and two image magnets that form as the superconductor cools below its critical temperature (a, b). [Note that in (b) the image magnets have been offset from one another for clarity.] The mobile image is a mirror image of the permanent magnet, and it moves as the permanent magnet moves (c). The frozen image is almost a mirror image of the permanent magnet at the moment the superconductor cools below its critical temperature; the orientation and position are mirror images, but the dipole vector is the same. The frozen image does not move. The force on the permanent magnet is the sum of the forces due to the image magnets.

A flux-pinning mechanism is a configuration of magnets and superconductors that, like a flexure, preferentially allows motion in specific degrees of freedom. Since the mechanism stiffness depends upon the magnet-superconductor cooling separation, these mechanisms fall into two broad categories: low-stiffness mechanisms that prioritize larger separations, and low-separation mechanisms that prioritize higher stiffness. Prior research into flux-pinning mechanisms has concentrated on designing mechanisms that serve as joints between spacecraft modules.[29,34,35] While these mechanisms belong in the first category since large separations are desired, similar techniques can be applied to designing optomechanical interfaces, which typically require high stiffnesses in order to control motion to a fraction of a

wavelength.[36–39]

Since flux pinning resists changes to the magnetic field distribution inside the superconductor, one design approach is to shape the magnetic field so that it is constant in directions where motion is desirable. For example, to allow only translation along a line, like a parallel-blade flexure, one mechanism design consists of a cubical superconductor pinned between two long cylindrical magnets [Figure 2.2(a)].* Since a line between and parallel to the magnets is the only direction without a magnetic field gradient, it is the only direction in which the superconductor can move freely; the geometry of the superconductor restricts rotation about this line. Similarly, to allow only rotation about an axis, like cross-blade flexure, the flux-pinning mechanism consists of a small cylindrical magnet pinned above a superconducting disk, as shown in Figure 2.2(b). Since the line connecting the magnet and superconductor is an axis of symmetry for the magnetic field, rotations about this axis are unconstrained. Motions in any other direction, however, are opposed by a restoring force since there is a magnetic field gradient.

An alternative approach to flux-pinning mechanism design is to combine field shaping with mechanical constraints. As an example, a flux-pinning mechanism analogous to a wire flexure consists of a cylindrical superconductor pinned to a spherical magnet mounted inside an inverted cone [Figure 2.2(c)]. This mechanism allows motion in five degrees of freedom. As before, the line connecting the magnet and superconductor is an axis of symmetry for the magnetic field, so the superconductor is free to rotate about this axis without disturbing the magnet. However, a spring-like restoring force opposes any motions that change the relative orientation and position of the magnet, such as motion along the line connecting

*This configuration corresponds to the prismatic joint described in (Shoer and Peck, 2009a; Shoer and Peck, 2009b).

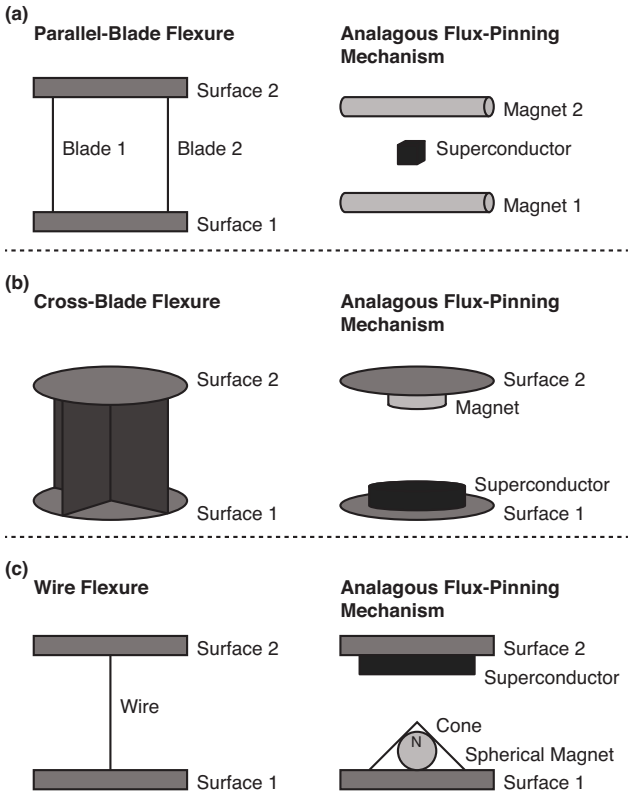

Figure 2.2: Flux-pinning mechanisms and the corresponding flexures. Like a flexure, a flux-pinning mechanism preferentially allows motion in specific degrees of freedom. These degrees of freedom depend upon the mechanism design, and there are two basic design approaches: shaping the magnetic field so that there is no change in the degrees of freedom in which motion is desired (a, b), and combining field shaping with mechanical constraints (c).

the two. As a result, rotating the superconductor about the cone will cause the magnet to rotate correspondingly since it is free to move within the cone; radial translation is the only motion the mechanism resists.

For the edgewise-connected mirror analysis that follows, we have selected the mechanism described in Figure 2.2(b). This mechanism consists of a 56 mm single-domain melt-textured YBCO disk[27] paired with a neodymium disk magnet, and the cooling separation varies from 0.5 to 2 mm. To represent this mechanism as a collection of collocated damped springs, it is assumed that all of the important dynamics can be captured by considering only the

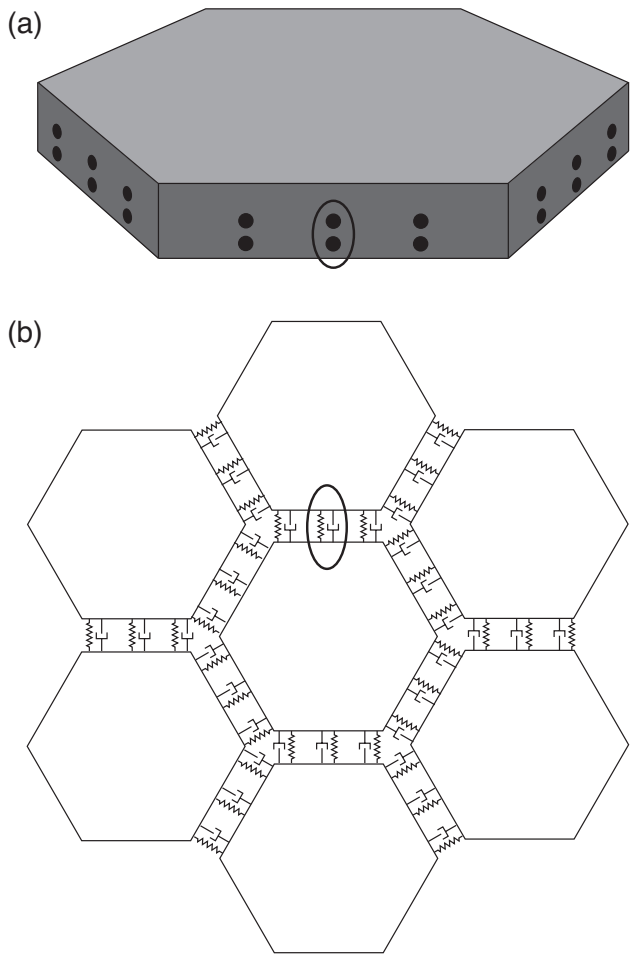

Figure 2.3: The mechanism model. As an example, we consider the case of an edgewise-connected mirror using the flux-pinning mechanisms shown in Figure 2.2(b). While these mechanisms resist bending to some extent, it is assumed that the resistance from a single mechanism is negligible; bending stiffness is added by using pairs of mechanisms, as circled on the segment in (a). In the model, each pair of mechanisms is represented by a set of four collocated single-degree-of-freedom damped springs (b), capturing the resistance to bending and translation.

relative translations between the magnet and superconductor. While this mechanism does resist bending to some extent, it is assumed that the resistance from a single mechanism is negligible. Instead, bending stiffness is added by using pairs of mechanisms separated by a distance d_r, as shown in Figure 2.3.

In this model, there are two rows of mechanisms along each segment edge, and each pair of mechanisms is represented by a set of four collocated single-degree-of-freedom damped springs. One of these damped springs corresponds to translation perpendicular to the superconductor surface, with stiffness $k_\perp$, and two of the springs correspond to translation parallel to the superconductor surface, with stiffness $k_\parallel$. The remaining spring corresponds to bending, with stiffness $k_b = \frac{1}{2}k_\perp d_r$. Since flux pinning is approximately twice as stiff for motion perpendicular to the magnet-superconductor interface as it is for motion parallel, we assume that $k_\perp$ is twice $k_\parallel$, and to account for the two rows of mechanisms, $k_\perp$ and $k_\parallel$ are also twice the values for a single mechanism. Finally, for simplicity, the damping is assumed to be isotropic.

2.3 Mechanism Characterization

The performance of an edgewise-connected mirror depends upon the mechanism stiffness and damping.[26] For a flux-pinning mechanism, these properties are affected by design choices including the cooling separation, the magnet strength, and the presence of conductive materials. To investigate the achievable stiffness and damping for mechanisms with cooling separations on the order of millimeters, rather than centimeters, we conducted a series of static and dynamic measurements for various mechanisms of the type shown in Figure 2.2(b). The static measurements provide insight into the basic mechanism behavior (Section 2.3.2), while the dynamic measurements illustrate how the stiffness and damping depend upon the mechanism parameters (Section 2.3.3). These static and dynamic measurements required constructing a specialized apparatus to address challenges posed by the need for cryogenic temperatures and the requirement for materials that would not interact with the mechanism,

as described in Section 2.3.1.

2.3.1 Measurement Apparatus

The stiffness and damping measurements present a number of practical challenges since flux-pinning mechanisms require cryogenic temperatures and interact with magnetic or conductive materials. For high-temperature superconductors such as YBCO,[27] the critical temperature is high enough that the mechanisms can be cooled in liquid nitrogen rather than using a cryogenic chamber. If this technique is used, the measurement apparatus must be able to withstand the repeated thermal shocks and large temperature gradients associated with rapidly cooling the mechanism. Low thermal conductivity and a low coefficient of thermal expansion are also desirable to minimize the frequency of replenishing the liquid nitrogen and the effects of temperature fluctuations. The apparatus must also be sufficiently stiff that the experiments measure the stiffness of the mechanism, not the apparatus. Finally, the apparatus cannot be constructed from magnetic or conductive materials, which would interact with the mechanism and interfere with the measurements. To address these challenges, we fabricated a specialized measurement apparatus using Zerodur, a low-expansion ceramic.[40]

This apparatus has two configurations: a static configuration for measuring the perpendicular stiffness and a dynamic configuration for measuring the parallel stiffness and damping. In the static configuration, a lever arm measures displacements perpendicular to the magnet-superconductor interface as the mechanism is loaded and unloaded incrementally with known weights [Figure 2.4(a)]. In the dynamic configuration, a cantilever suspends the magnet over the superconductor, with a parallel-blade flexure restricting the motion to a

line parallel to the superconductor surface (Figure 2.8). In both configurations, the superconductor rests on a Zerodur platform insulated by a Styrofoam box that contains the liquid nitrogen. For stability, the platform is supported by three Zerodur legs that pass through the Styrofoam to rest on a granite table.

2.3.2 Static Measurements (Perpendicular Stiffness)

To determine the perpendicular stiffness and investigate the mechanism behavior, we measured changes in the magnet-superconductor separation as the flux-pinning mechanism was loaded with a sequence of known weights and incrementally unloaded. In these static experiments, the superconductor was constrained so that changes in the magnet-superconductor separation corresponded to deflections of the magnet. These deflections, Δh, were measured by reflecting a laser off a mirror mounted to a lever arm that rotated as the separation changed, and tracking the location of the reflected beam spot on a target a distance D away [Figure 2.4(a)].

The relationship between the measured changes in the reflected beam spot location and Δh can be determined by considering the experiment geometry and the changes that occur as the mechanism and apparatus transition from room temperature to cryogenic temperatures and as the spacer that constrains the magnet-superconductor separation during cooling is removed. At room temperature, the location of the reflected beam spot is determined by the deviation of the mirror normal from 45°, α_n, the laser misalignment, α_l, and the initial tilt of the lever arm, α_p [Figure 2.4(b)]. Since the pivot mirror rotates with the lever arm, the total tilt changes the height of the spot where the laser intersects the mirror, shifting the

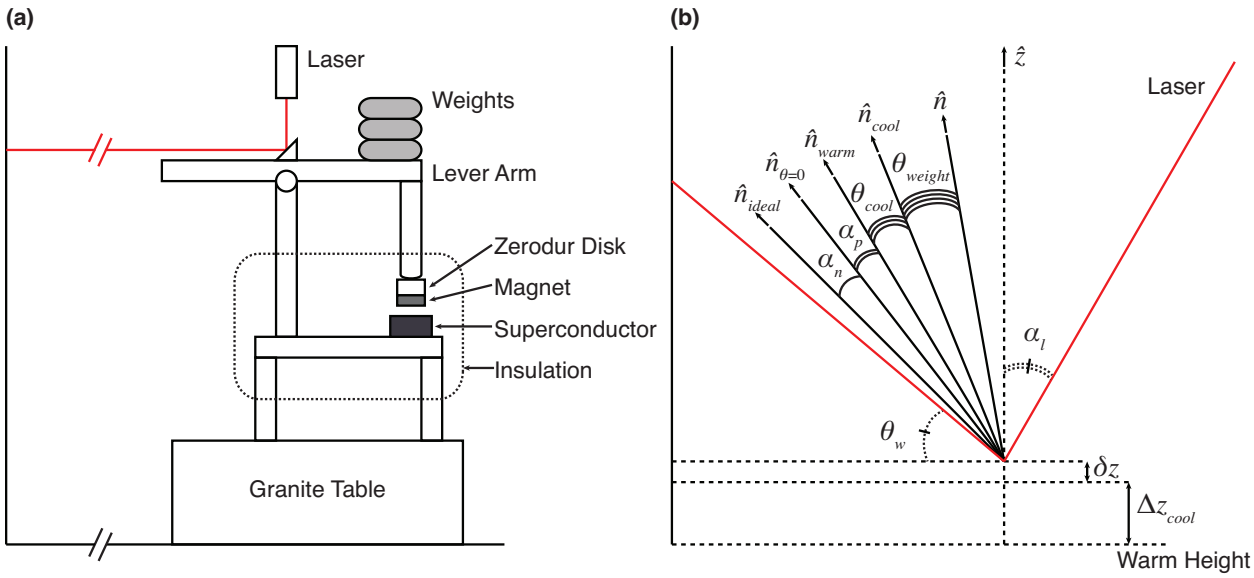

Figure 2.4: The static measurements. To determine the perpendicular stiffness, changes in the magnet-superconductor separation are measured as the mechanism is loaded with a sequence of known weights. These weights are placed on a lever arm that rotates as the magnet-superconductor separation changes, and the changes are measured by reflecting a laser off a mirror attached to the lever arm and tracking the location of the reflected beam spot (a). The deflection due to the applied weight corresponds to a rotation angle of θ_{weight}, and the relationship between θ_{weight} and the beam spot motion depends upon thermal effects and various misalignments in addition to the applied weight (b). (Angles in the figure have been exaggerated for clarity.)

height of the reflected beam by δz. As liquid nitrogen is added, the apparatus expands due to its negative coefficient of thermal expansion,[41,42] increasing the height of the point where the laser intersects the mirror by Δz_{cool}. In addition, the mechanism contracts, causing the pivot arm to rotate by an additional amount θ_{cool}. These two effects are distinguished by comparing changes in the location of the reflected pivot beam spot to changes in the location of a reflected spot from a laser aimed at a reference mirror attached to a stationary part of the apparatus. After the experiment reaches thermal equilibrium, the spacer between the magnet and the superconductor is removed, and the mechanism is loaded with a known weight. As the magnet-superconductor separation decreases in response to the weight, the lever arm rotates by an additional amount θ_{weight}.

At each stage of the experiment, the translation of the reflected pivot beam spot is related to the total lever arm rotation, θ, by

$$D\tan(2\theta + 2\alpha_n - \alpha_l) = H_{target} - \Delta z_{cool} - \delta z, \tag{2.1}$$

where H_{target} is the height of the reflected pivot beam spot relative to the height of the point where the beam intersects the mirror when the experiment is at room temperature. Since δz is given by

$$\delta z = \left[\frac{\sin\theta(x_2 - x_1) + \cos\theta(z_2 - z_1)}{\cos\theta(x_2 - x_1) - \sin\theta(z_2 - z_1)}\right](x_\alpha - x_1\cos\theta + z_1\sin\theta) + x_1\sin\theta + z_1\cos\theta - z_\alpha,$$

where $(x_1,\, z_1)$ and $(x_2,\, z_2)$ are points on the mirror surface and $(x_\alpha,\, z_\alpha)$ is the point where the beam hits the mirror, (2.1) can be rewritten as

$$\begin{aligned} D\tan(2\theta + 2\alpha_n - \alpha_l) = {} & H_{target} - \Delta z_{cool} - x_1\sin\theta - z_1\cos\theta + z_\alpha \\ & - \left[\frac{\sin\theta(x_2 - x_1) + \cos\theta(z_2 - z_1)}{\cos\theta(x_2 - x_1) - \sin\theta(z_2 - z_1)}\right](x_\alpha - x_1\cos\theta + z_1\sin\theta). \end{aligned} \tag{2.2}$$

The various rotation angles are determined by iteratively solving (2.2) for θ and noting that

$$\theta = \begin{cases} \alpha_p & \text{when the experiment is warm,} \\ \alpha_p + \theta_{cool} & \text{when the experiment reaches thermal equilibrium,} \\ \alpha_p + \theta_{cool} + \theta_{weight} & \text{when weights are applied.} \end{cases}$$

To relate θ_{weight} to the deflection caused by adding the weight, Δh_{weight}, we begin by noting that once the experiment reaches thermal equilibrium, the height of the lever arm pivot point relative to the bottom of the superconductor, H_{cold}, is a constant. Before the spacer is removed, H_{cold} is given by

$$d\sin(\alpha_p + \theta_{cool}) + l\cos(\alpha_p + \theta_{cool}) + h_{disk} - \Delta h_{disk} + h - \Delta h_{cool},$$

where d is the distance from the pivot point to the end of the lever arm, l is the length of the indenter, h_{disk} is the thickness of the Zerodur disk at room temperature, Δh_{disk} is the change in h_{disk} due to cooling, h is the distance from the bottom of the superconductor to the top of the magnet at room temperature, and Δh_{cool} is the change in h due to cooling (Figure 2.5). After the spacer is removed and weights are applied, H_{cold} is given by

$$d\sin(\alpha_p + \theta_{cool} + \theta_{weight}) + l\cos(\alpha_p + \theta_{cool} + \theta_{weight}) + h_{disk} - \Delta h_{disk} + h - \Delta h_{cool} - \Delta h_{weight}.$$

Equating these two expressions and solving for Δh_{weight}, we find that

$$\Delta h_{weight} = d\sin(\alpha_p+\theta_{cool}+\theta_{weight}) - d\sin(\alpha_p+\theta_{cool}) + l\cos(\alpha_p+\theta_{cool}+\theta_{weight}) - l\cos(\alpha_p+\theta_{cool}),$$

which for small angles reduces to

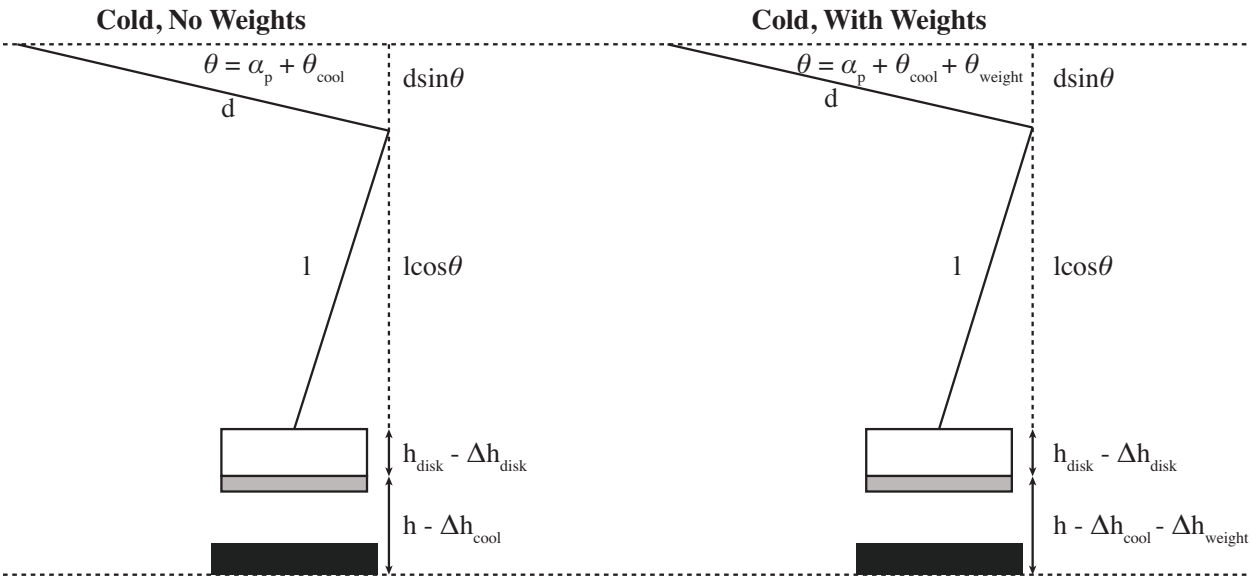

Figure 2.5: Relating θ_{weight} to the magnet deflection. Since the height of the lever arm pivot point relative to the bottom of the superconductor is a constant, the amount of rotation caused by adding weight, θ_{weight}, and the corresponding magnet deflection, Δh_{weight}, are related by $\Delta h_{weight} = d\theta_{weight}$ for small angles.

$$\Delta h_{weight} = d\theta_{weight}. \tag{2.3}$$

To investigate the mechanism behavior, the mechanism was loaded with a sequence of weights, gradually increasing to a maximum of W_{seq}, then unloaded in reverse order. After several repetitions, W_{seq} was incremented to a new value. As Figure 2.6 shows, the resulting deflection pattern is affected by the heaviest weight that has ever been applied, W_{max}. As W_{max} increases, the pattern shifts toward larger deflections. (If W_{seq} is less than W_{max}, the pattern does not shift back toward smaller deflections.) This effect appears to be an offset only, with no effect on the stiffness; when the offset between the average initial deflections for two sequences is subtracted, the data points for both sequences fall on the same curve. This hysteretic behavior suggests that as W_{max} increases, the mechanism sags. For practical purposes, there are two implications: the mechanisms can be trained to have a particular

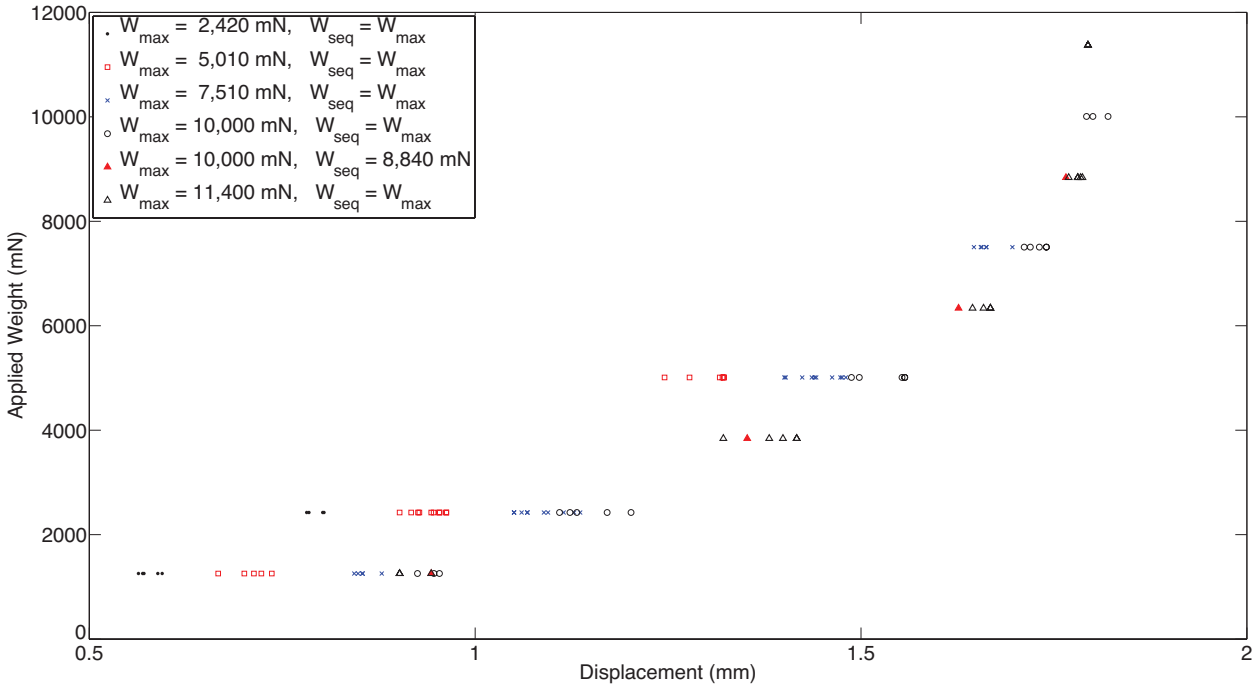

Figure 2.6: The importance of W_{max}. As the mechanism is sequentially loaded or unloaded, the deflection pattern depends upon the maximum weight that has ever been applied, W_{max}, rather than the heaviest weight in the sequence, W_{seq}. Increasing W_{max} shifts the pattern toward larger deflections without affecting the stiffness, and the pattern does not shift back toward smaller deflections if $W_{seq} < W_{max}$.

deflection pattern if the maximum load remains below some threshold, and the deflections will increase if this threshold is exceeded. Since the mechanisms are situated along the segment edges, the ability to specify the deflection pattern corresponds to an ability to specify the size of the gap between adjacent segments, which may prove beneficial in situations where the gap must remain above a minimum value.

The stiffness values can be estimated from the deflection pattern by approximating the derivative between adjacent data points. For two points $(\Delta h_{weight,1}, W_1)$ and $(\Delta h_{weight,2}, W_2)$, the stiffness corresponding to the mean deflection is approximately

$$k = \frac{W_2 - W_1}{\Delta h_{weight,2} - \Delta h_{weight,1}}.$$

As Figure 2.7 shows, the stiffness is nonlinear, and the shape of the curve depends on both the cooling separation and the magnet deflection. Decreasing the cooling separation increases the stiffness, as expected, and also leads to smaller shifts as W_{max} increases. For a fixed cooling separation, the stiffness varies by an order of magnitude as the magnet-superconductor separation diminishes, increasingly sharply as the separation approaches zero. This increase is to be expected; previous work suggests that the stiffness increases nearly exponentially as the magnet approaches the superconductor.[43,44] This behavior may prove beneficial in an edgewise-connected mirror: the mechanisms provide increasing resistance the closer the two segments come to colliding.

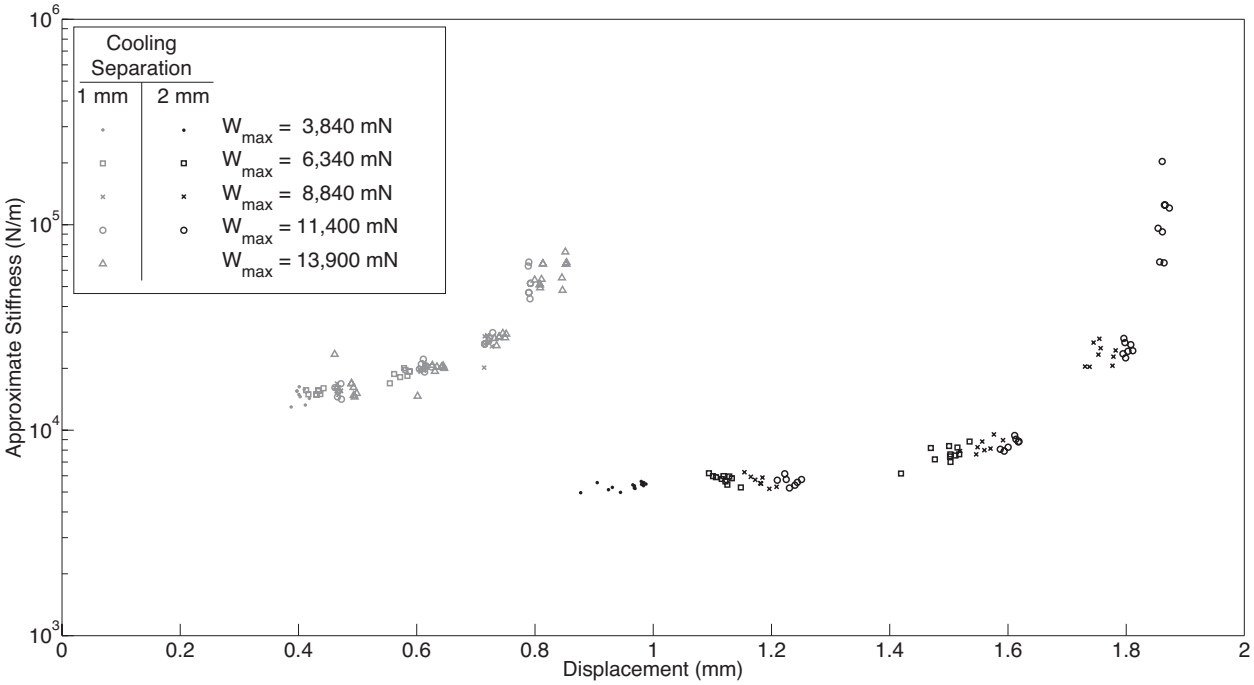

Figure 2.7: The perpendicular stiffness. As the magnet approaches the superconductor, the stiffness varies by an order of magnitude, increasing sharply as the magnet-superconductor separation vanishes. As a result, the flux-pinning mechanism provides increasing resistance the closer two segments in an edgewise-connected mirror come to colliding. Decreasing the cooling separation leads to stiffer mechanisms.

2.3.3 Dynamic Measurements (Parallel Stiffness and Damping)

To determine the parallel stiffness and damping and study their dependence on the mechanism implementation, we measured the impulse response for mechanisms with various magnets and cooling separations of $0.5 - 2$ mm. Since flux pinning is affected by the shape and strength of the magnetic field present during cooling, magnets of different diameter and thickness were tested. In addition to conventional magnets, we also tested a Swirl magnet, a neodymium magnet imprinted with a magnetic field pattern that preferentially allows rotational motion.[45–47] This pattern was selected in order to investigate whether the rapidly changing magnetic field and its resistance to translation correspond to an increase in $k_{\|}$. For

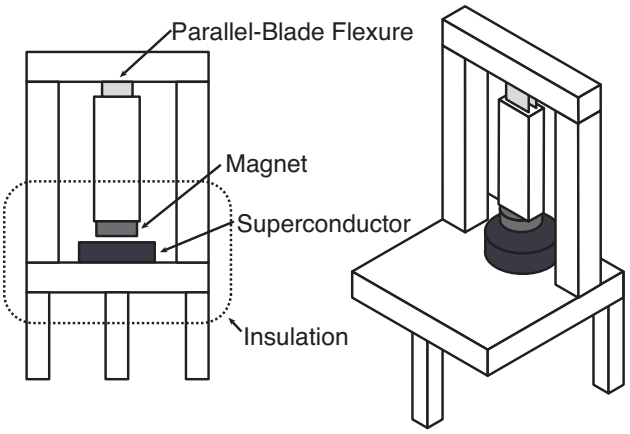

Figure 2.8: The dynamic measurements. The parallel stiffness and damping are determined by measuring the impulse response. For these measurements, a cantilever suspends the magnet over the superconductor, with a parallel-blade flexure restricting the motion to a line parallel to the superconductor surface.

each mechanism, the stiffness and damping were extracted from the impulse response using eigensystem realization analysis,[48] and the results of multiple trials were averaged.

As shown in Figures 2.9 and 2.10, $k_{\parallel}$ and c generally increase as the cooling separation decreases or the magnet strength increases. These trends are to be expected since both stronger magnets and smaller cooling separations increase the magnetic flux penetrating into the superconductor during cooling; previous measurements have suggested that the stiffness increases nearly exponentially as the cooling separation decreases.[29,49] For the mechanisms tested, the effects of varying the cooling separation are particularly noteworthy. As the cooling separation decreased from 2 mm to 0.5 mm, the stiffness increased by a factor of 2-10, with typical values on the order of $1,000$ N/m, and the damping increased by up to an order of magnitude, with typical values on the order of $1-10$ kg/s. By comparison, previous measurements using comparable mechanisms with a cooling separation of 5 cm reported stiffnesses on the order of 7 N/m and no discernible damping.[29]

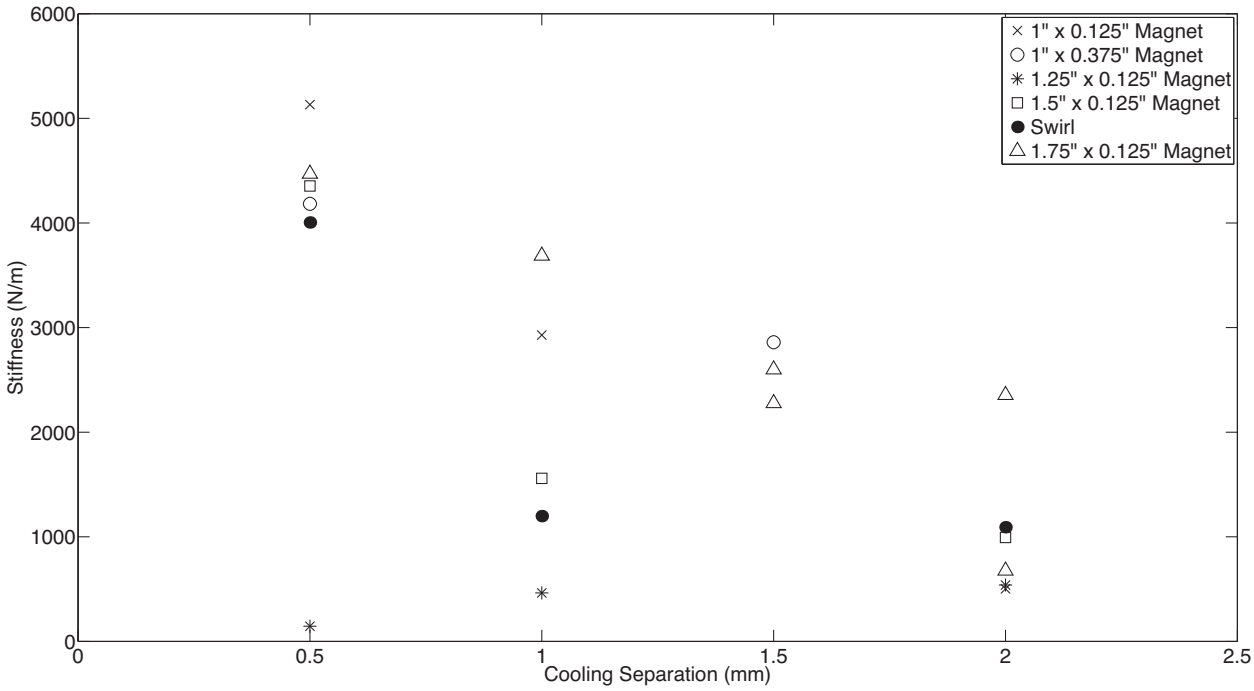

Figure 2.9: The parallel stiffness for various mechanisms. In general, stronger magnets and smaller cooling separations lead to stiffer mechanisms. With cooling separations on the order of 1 mm, the mechanisms tested typically have stiffnesses on the order of $1,000$ N/m. By comparison, previous measurements for similar mechanisms with cooling separations on the order of 5 cm reported stiffnesses on the order of 7 N/m.[29]

While additional testing is needed to investigate the merits of using patterned rather than conventional magnets, the Swirl magnet considered in these experiments seems less useful than a conventional magnet of the same size. Although the Swirl pattern is designed to resist translation, the mechanism using the Swirl magnet typically had a lower stiffness than a mechanism using a conventional neodymium magnet with the same dimensions. Since the Swirl pattern concentrates the magnetic field in the near field,[47,50] it is possible that less flux penetrates into the superconductor, leading to a lower stiffness. This effect could also influence the amount of damping. Although the mechanism using the Swirl magnet had higher damping than the mechanism using the conventional magnet, the reverse may be true if the mechanisms are modified to include nonmagnetic conductive materials: since the increased damping is due to eddy current damping, the lower flux penetration of the Swirl

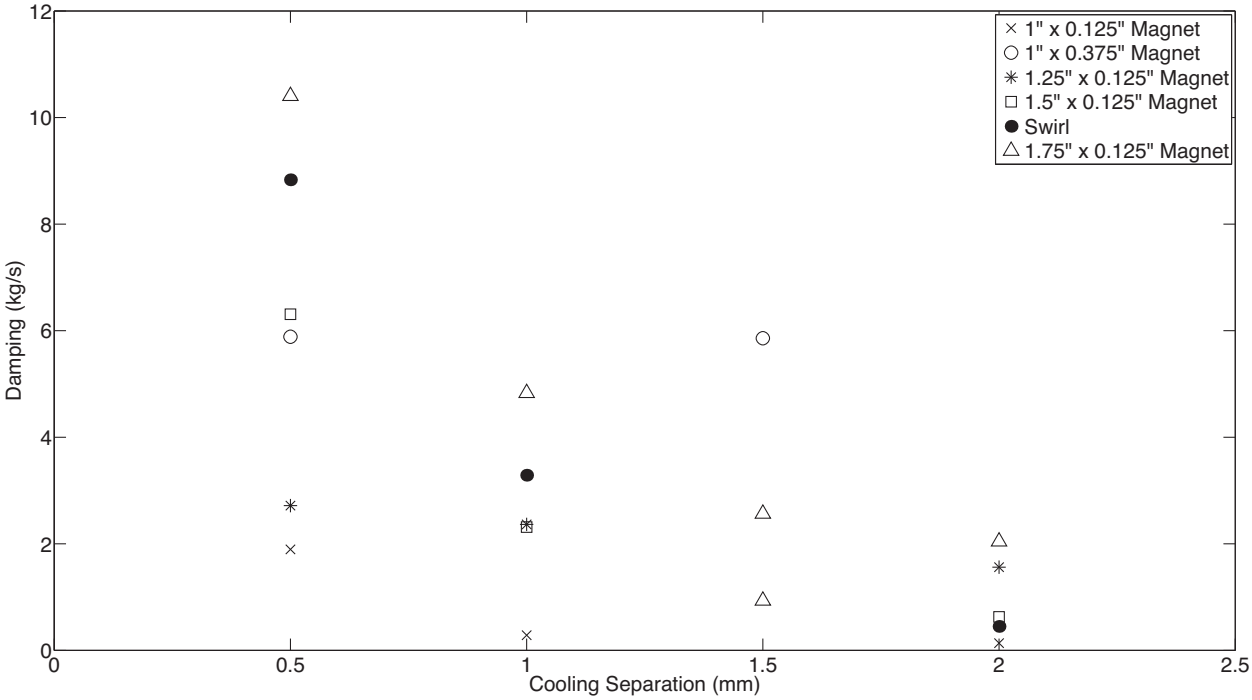

Figure 2.10: The damping for various mechanisms. With cooling separations on the order of 1 mm, the mechanisms tested typically have damping values on the order of $1 - 10$ kg/s. Smaller cooling separations and stronger magnets generally correspond to higher damping. By comparison, previous measurements with similar mechanisms and cooling separations on the order of 5 cm reported no discernible damping.[29]

magnet could correspond to smaller gains.

2.4 Simulated Mirror Performance

To investigate the performance improvements provided by placing flux-pinning mechanisms along the segment edges, we consider the impulse response of a 15 m edgewise-connected mirror that has mechanisms with stiffness and damping values representative of the measurements presented in Section 2.3. For simplicity, the mirror is kinematically mounted at three points with the mechanisms serving as the only connections between the

segments; although it is likely that the segments would be mounted individually to a backplane in practice, the problem of segmented mount design is beyond the scope of this paper.

Previous modeling work[26] has shown that the magnitude of the impulse response is affected primarily by the mechanism stiffness. Since disturbances propagate more effectively across a mirror with strongly connected segments, higher mechanism stiffnesses correspond to larger responses. For high-stiffness mechanisms, the segmented mirror response is comparable to that of a monolith, while for the stiffnesses measured in Section 2.3, the response is an order of magnitude lower. If performance comparable to that of a monolith is desired, the flux-pinning mechanism stiffness must be increased by approximately three orders of magnitude, which may be achievable by using smaller cooling separations or stronger magnets.

As shown in Figure 2.11, the damping contributions from the mechanisms improve the impulse response, reducing the number of oscillating frequencies and increasing the decay rate. Though the improvements are modest, more substantial gains are possible with higher damping values.[26] These values may be attainable by placing nonmagnetic conductive materials near the mechanisms. Approaches include placing bulk material adjacent to the mechanisms and fabricating the mirror segments from a nonmagnetic conductive material. The amount of additional damping will likely depend on a variety of factors including the magnet strength, the distance between the material and the moving magnet, the material conductivity, and the amount of material. Quantifying how the amount of material and its placement affect the damping is a subject for future investigations.

2.5 Summary

As future astrophysics missions require larger far-IR to submillimeter space telescopes, maintaining the stability of the cryogenic primary becomes increasingly challenging. One approach to increasing the mirror stiffness and damping is to use an edgewise-connected architecture, with flux-pinning mechanisms placed along the segment edges. Consisting of a configuration of magnets and superconductors, flux-pinning mechanisms are uniquely suited for cryogenic mirrors since they require low temperatures to operate, unlike mechanical devices, which can have problems with lubrication, CTE matching, and thermal snap. Like flexures, flux-pinning mechanisms preferentially allow motion in specific degrees of freedom, which depend upon the mechanism design. These non-contacting mechanisms are passively stable and require no power other than the amount needed for cooling.

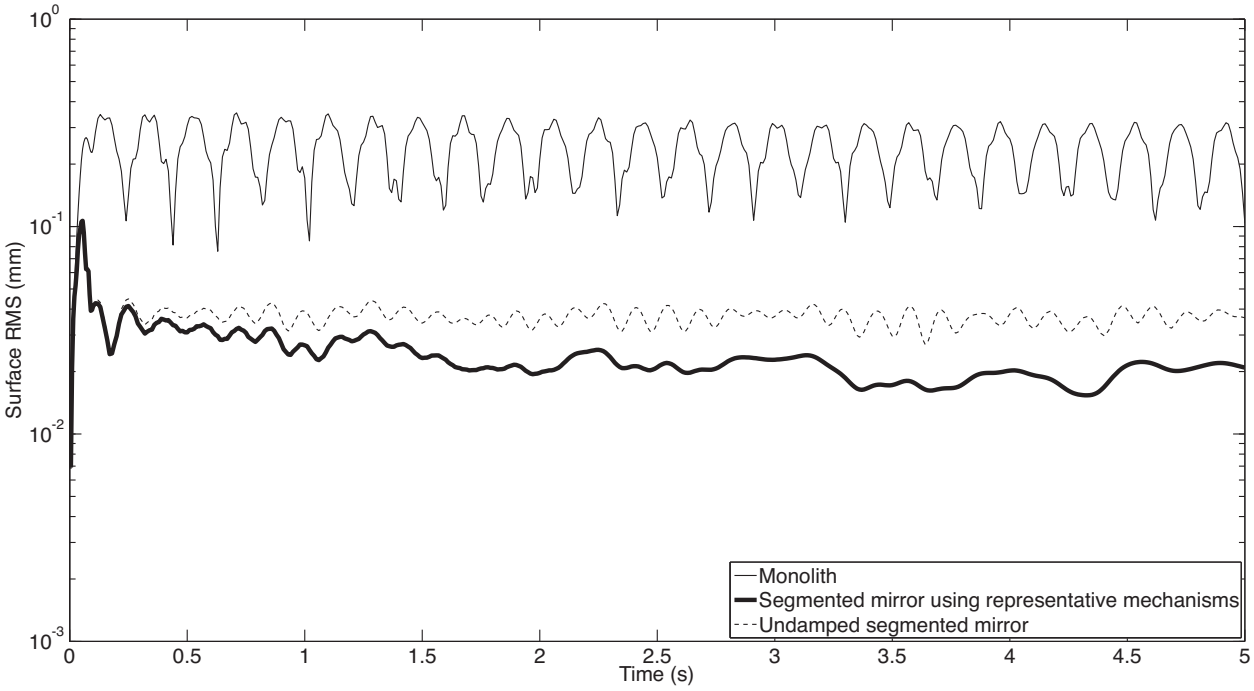

Figure 2.11: The impulse response for an edgewise-connected mirror with flux-pinning mechanisms. The damping provided by the flux-pinning mechanisms improves the disturbance response, reducing the number of vibrating frequencies and increasing the decay rate. For reference, the responses of the undamped segmented mirror and a monolith of the same size and shape are also shown; the segmented mirrors are identical except for the mechanism damping. The responses of the segmented mirrors are approximately an order of magnitude lower than the response of the monolith since disturbances do not propagate as effectively across a primary consisting of weakly-connected segments; the effects of a backplane are not considered in this model.

The stiffness and damping contributions from the flux-pinning mechanisms improve the mirror stability and lessen the requirements for the mirror support structure. As an example, a flux-pinning mechanism consisting of a single magnet and superconductor has been considered. With an inexpensive magnet and a cooling separation on the order of 1 mm, this type of mechanism has typical stiffness and damping values on the order of 5,000 N/m and 5 kg/s, respectively. With these values, the mechanisms provide modest improvements to the mirror performance, increasing the stiffness and decreasing the settling time. Greater stiffnesses can be achieved by using stronger magnets or smaller cooling separations, and

the damping can be adjusted independently by placing nonmagnetic conductive materials near the mechanism. Quantifying the increases in damping due to the material amount and placement remains a subject for future investigation.

CHAPTER 3

IMPROVING ACTIVE SPACE TELESCOPE WAVEFRONT CONTROL USING PREDICTIVE THERMAL MODELING

3.1 Introduction

Active control enables large telescopes by maintaining optical performance in the presence of perturbations. Active control algorithms have been optimized for large ground telescopes and are commonly used to compensate for manufacturing errors, gravitational and thermal distortions, and low-frequency errors induced by wind.[9,51–54] By comparison, active control algorithms for space telescopes are less mature. The baseline control scheme for the first large active optical/infrared space telescope, the James Webb Space Telescope (JWST), is conceptually simple, consisting of measuring the wavefront error (WFE) every two days and using these measurements to apply corrections every two weeks as needed.[55] This scheme satisfies the observatory's requirements; however, alternative control algorithms may further improve the performance, providing lower and/or more stable wavefront errors and enhancing science capabilities.

The difference in maturity between the control algorithms for active space telescopes such as JWST and active ground telescopes is due in part to differences in the wavefront control problems, which stem from differences in the observatory design constraints and

The material in this chapter will be submitted to a peer-reviewed journal as J. Gersh-Range and M. D. Perrin, "Improving active space telescope wavefront control using predictive thermal modeling" (2014).

environment. For an active space telescope, the control problem involves a trade between minimizing the wavefront error deviations and minimizing the number of corrections. Limited by the mass and volume constraints of a launch vehicle, active space telescopes generally use the science instruments to monitor the wavefront periodically.[56] As a result, there is a significant cost associated with each wavefront measurement; since science observations and wavefront measurements cannot be performed simultaneously, each wavefront measurement reduces the observatory efficiency. This cost is amplified for control schemes that require a post-correction wavefront measurement to verify the actuator motions, and it provides one incentive to limit the number of corrections. Additional incentives to avoid unnecessary control include the inability to repair or replace actuators that have exceeded their design lifetimes and, for cryogenic mirrors, the possibility of introducing heat with each actuator move.

In addition, high-speed continuous control is less necessary for an active space telescope at L2 since the dominant wavefront perturbations are driven by changes in the thermal environment, with timescales on the order of hours to days. These changes are caused by variations in the solar heating as the telescope attitude changes from one observation to the next. Minimizing degradations from such medium-timescale perturbations is the key challenge for active wavefront maintenance in space. Slower perturbations, such as those due to gradual degradation of a sunshield or insulation or to annual orbital variations in the distance to the sun, are readily corrected by a control scheme that operates on a timescale of days to weeks, and faster dynamical perturbations leading to pointing jitter can be partially controlled by an active fine steering mirror[9] up to some control-bandwidth-limited frequency.

The control problem for an active space telescope thus consists of weighing control costs against the benefits of correcting wavefront error perturbations that are a predictable byprod-

uct of the observing schedule, which we determine and know in advance. This is a very different situation than the one faced by active ground telescopes, where the rapid weather-dominated disturbances require continual control, wavefront measurements and science observations are performed concurrently using separate dedicated hardware, and worn-out actuators can be replaced.

In this paper, we investigate several methods for improving the control algorithms for active space telescopes at L2. We do not discuss the details of how the wavefront measurements are to be obtained nor how the desired controls are applied via spacecraft actuators; these topics have been discussed at length in other papers.[55–57] Our focus here is on the question of how often sensing and control should take place and how multiple sensing measurements may be combined in order to optimize performance. Although our analysis is based on JWST specifically, the general approach taken is also applicable to other missions, such as AFTA and ATLAST.[58,59]

Note that the overall optical performance of JWST depends on contributions from many other factors besides the thermal perturbations we model here, including the telescope's static WFE, the science instruments' internal WFE, and uncontrolled high-temporal-frequency jitter. Integrated modeling predicts a total telescope WFE in the range of 90-110 nm rms,[60] so the time-variable component (expected to be of order 60 nm) corresponds to a significant part of JWST's overall optical error budget. Several of JWST's driving science cases are exquisitely sensitive to variations in point spread function properties, for instance weak lensing studies of the early universe or coronagraphic observations of nearby exoplanets, and would benefit greatly from as stable a telescope as possible. Intrinsic wavefront sensor noise and calibration systematics likely set a fundamental limit of a few nm rms. How closely can we approach that limit?

Since the dominant WFE perturbations are due to thermal fluctuations, we have developed a combined thermal and wavefront model that tracks the temperature evolution over a sample mission and calculates the corresponding WFE (Section 3.2). A similar approach has been used successfully to track focus variations in the Hubble Space Telescope.[61] Using this model, we first show that the WFE can be controlled passively by introducing scheduling constraints that limit the allowable sun angles for an upcoming observation based on the mean telescope temperature (Section 3.3). We then turn to strategies for active control: we describe the design and implementation of a predictive hybrid controller (Section 3.4.2) and assess its performance relative to simpler control strategies under a variety of assumed conditions (Section 3.4.3). This algorithm is designed to prevent the WFE from ever exceeding a desired limit instead of simply reacting after the limit has been exceeded; it uses an internal thermal model to predict when the WFE will exceed the threshold and schedules corrections in advance. As a result, the corrections are placed at more effective times, and the algorithm achieves a lower WFE without requiring significantly more corrections. We close (Section 3.5) with a summary of results and a look ahead to future work and the feasibility of implementation for JWST.

3.2 Thermal and Wavefront Model

During the course of a mission, an active space telescope such as JWST is rarely, if ever, in thermal equilibrium. The equilibrium thermal state is affected by the amount of solar heating, which depends upon the attitude of the telescope relative to the sun. As a result, the equilibrium state is different for each observation, changing as the telescope slews from one science target to the next. Since a typical observation lasts a few hours, there is insufficient

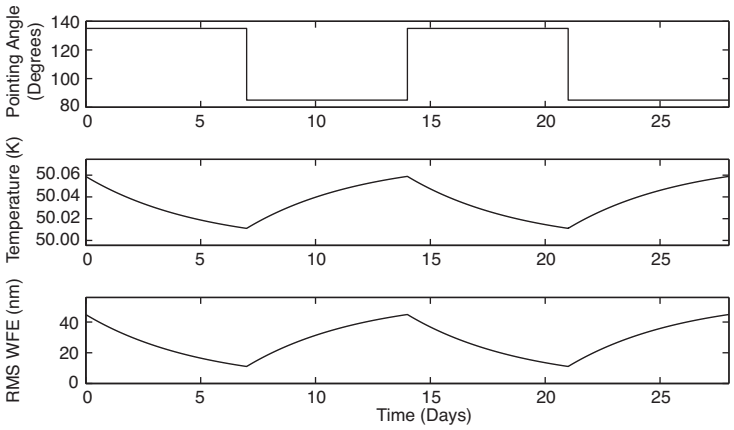

Figure 3.1: Sample temperature and wavefront evolution for a repeated slew between two attitudes. Since an active space telescope is rarely in thermal equilibrium, the mean telescope temperature is not a simple function of attitude. During an observation, the temperature follows an exponential determined by the temperature at the start of the observation, the observation duration, and the equilibrium temperature associated with the sun angle. These parameters change with each observation, altering the temperature trajectory. The change in the wavefront error with respect to some nominal state is determined from the temperature using a linear model. As an example, the temperature and RMS wavefront error evolution are shown for a square-wave pointing schedule.

time for a cryogenic shielded telescope to equilibrate before the next slew; the thermal time constant for typical designs is on the order of days.[1,62,63] As a result, the thermal state of the telescope is not a simple function of attitude, but rather a complex function of attitude history. As the thermal state changes during a mission, the thermally induced deformations in the observatory structures also vary, causing perturbations in the WFE (Figure 3.1).

To investigate how the WFE evolves in response to changes in the thermal state, we have developed a combined temperature and wavefront model. This model assumes that all of the important dynamics can be determined to first order by tracking a single temperature that corresponds to the dominant deformation. As an example, distortions of the primary mirror backplane support structure are expected to dominate the WFE evolution for JWST, and these distortions correspond to changes in the average backplane temperature.[1,64] The

model also assumes that the thermal changes are caused only by variations in the spacecraft orientation with respect to the sun (hereafter "sun angle"). Although changes due to roll or other sources could be included in a more sophisticated model, these perturbations are small by comparison. As an example, JWST has an allowed pointing range of 85° to 135° between the telescope optical axis and the sun, set by the geometry needed to keep the telescope in the shade at all times (Figure 3.2). Rotations azimuthally around the optical axis are relatively minor since they are restricted to a range of approximately +4° to −4°, and rotations around the JWST-to-sun axis, though unconstrained, do not affect the amount of solar heating.[65]

Since the equilibrium thermal state can change with each observation, the combined temperature and wavefront model follows three basic steps for each observation: determining the equilibrium temperature, calculating the temperature evolution, and relating the temperature to a wavefront error. In the equilibrium temperature model, each sun angle ϕ is associated with the equilibrium temperature T_e the telescope would attain if left at that attitude for infinitely long. This temperature can depend, for example, upon the projected area of the sunshield normal to the sun, which varies cosinusoidally with the sun angle. More generally, this relationship can be parameterized to second order as

$$T_e = a\phi^2 + b\phi + c, \tag{3.1}$$

where the constants a, b, and c are determined by fits to available thermal models or on-orbit measurements. In the case of JWST, detailed finite element modeling[64] has concentrated on the hottest and coldest attitudes, so we fit a, b, and c by considering these extreme cases. These attitudes determine the temperature range, and they are affected by the sunshield geometry and the pointing restrictions.

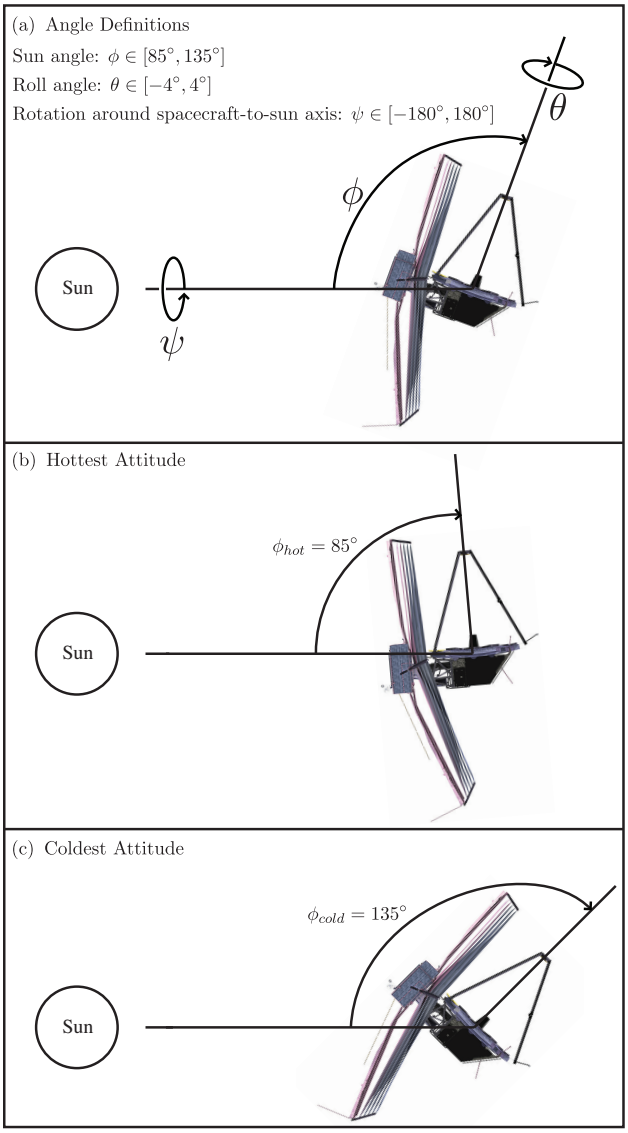

Figure 3.2: Attitude range. For the simulations, we assume that the spacecraft attitude range is identical to that of JWST[65] (a). The hottest attitude corresponds to a sun angle of 85° (b), and the coldest attitude corresponds to a sun angle of 135° (c). Since thermal changes are predominately due to changes in the sun angle ϕ, we concentrate here on the effects of ϕ alone.

During an observation, the mean telescope temperature is assumed to follow an exponential of the form

$$T = (T_0 - T_e)e^{-k(t-t_0)} + T_e, \tag{3.2}$$

where T_0 is the temperature at the beginning of the observation, t_0 is the time the observation begins, and k is the thermal decay constant. In general, the temperature at the start of observation j, $T_0(j)$, will depend upon the temperature at the end of observation $j-1$, $T_f(j-1)$, and the slew duration. For the initial investigations in Section 3.4, we consider the worst-case thermal changes by neglecting slews and assuming that $T_0(j) = T_f(j-1)$.

After the temperature has been determined, the corresponding wavefront error is calculated using a linear model. For these calculations, it is convenient to consider the change in the wavefront error with respect to some nominal state, such as the long term average optical state or the observatory's best-achieved starting alignment. We denote this by $\mathbf{W}$:

$$\mathbf{W} = \mathbf{W}_{total} - \mathbf{W}_{nominal}. \tag{3.3}$$

Since the temperature is bounded by T_{hot} and T_{cold}, it is particularly convenient to calculate changes in the wavefront error relative to the wavefront error at one of these limiting temperatures; we use T_{cold}. For simplicity, the wavefront model assumes that each coefficient in the expansion of the wavefront scales linearly with temperature; in the absence of control, the relative WFE is

$$\mathbf{W} = \left(\frac{T - T_{cold}}{T_{hot} - T_{cold}}\right) \begin{bmatrix} w_1 \\ w_2 \\ w_3 \\ \vdots \\ w_n \end{bmatrix} = \left(\frac{T - T_{cold}}{T_{hot} - T_{cold}}\right) \mathbf{w}, \tag{3.4}$$

where the w_i are the first n Zernike coefficients specifying the change in WFE at the hottest temperature. As an example, the temperature and wavefront error trajectories for a hypothetical back-and-forth slew pattern between two attitudes are shown in Figure 3.1.

For the simulations that follow, we consider an active space telescope at L2 with thermal properties based on the requirements for JWST. The allowable sun angles are identical to those for JWST,[65] ranging from 85° to 135°. The hottest attitude is 85° and the coldest is 135°, as shown in Figure 3.2. The thermal decay constant is assumed to be 0.2 days^{-1}, based on the JWST requirement that the WFE is sufficiently stable to achieve < 60 nm rms over a two-week period in the absence of wavefront control,[1] and the Zernike coefficients w_i are similarly chosen such that the RMS WFE changes by approximately 56 nm for the worst-case slew. These coefficients, along with the remaining thermal model parameters such as the temperature range, are loosely derived from the results of detailed finite-element thermal modeling of the temperature evolution following a worst-case cold-to-hot slew.[64,66]

3.3 Limiting the WFE Using Schedule Restrictions

Since the WFE perturbations are driven by changes in the sun angle, they are a byproduct of the observing schedule, which we know and determine in advance. As a result, we can control the WFE evolution passively by introducing scheduling constraints as part of the schedule generation process. This type of approach has been studied for managing the spacecraft momentum,[67] which also depends on the sun angle, and the same or similar constraint mechanisms in the scheduling software could be extended to consider the WFE. These constraints can in principle either limit the WFE change during an observation or

ensure that the total WFE change never exceeds a specified limit. For the thermal model we consider, both approaches are suitable for typical observations, allowing most if not all of the sky. However, in practice limiting the total WFE change may be too restrictive since the constraints limit the field of regard for long observations.

Since changes in the WFE are directly related to changes in the telescope temperature, the scheduling constraints are derived from temperature restrictions; the basic principle is to generate schedules that do not cause the telescope temperature to experience extreme swings or deviate from a specified range. Limiting the WFE change during an observation, for example, corresponds to defining a range of allowable final temperatures based on the initial temperature and the observation duration. Similarly, ensuring that the total WFE change remains below a specified threshold corresponds to requiring that the temperature remain at all times within a range determined by the reference temperature (for which there is no WFE). In each case, the temperature limits determine the maximum and minimum equilibrium temperatures, which correspond to the minimum and maximum allowable sun angles, respectively, for the next spacecraft attitude in the schedule. As a result, the scheduling constraints are derived by relating the desired WFE condition to restrictions on the final temperature, determining the limiting equilibrium temperatures, and calculating the corresponding sun angles.

As an example, to ensure that the WFE change during an observation does not exceed a desired threshold τ, we require that

$$|\Delta RMS| = \left| \sqrt{\mathbf{W}(t_f) \cdot \mathbf{W}(t_f)} - \sqrt{\mathbf{W}(t_0) \cdot \mathbf{W}(t_0)} \right| \leq \tau, \tag{3.5}$$

where t_0 and t_f are the times at which the observation begins and ends, respectively. Using

Equation (3.4), we can rewrite this condition as

$$-\tau \leq \frac{T_f - T_0}{T_{hot} - T_{cold}} \sqrt{\mathbf{w} \cdot \mathbf{w}} \leq \tau, \tag{3.6}$$

where T_f is the temperature at the end of the observation. Solving for T_f, we find that Equation (3.5) is satisfied if

$$T_f \in [T_{min}, T_{max}], \tag{3.7}$$

where

$$T_{max} = \frac{\tau(T_{hot} - T_{cold})}{\sqrt{\mathbf{w} \cdot \mathbf{w}}} + T_0 \tag{3.8}$$

and

$$T_{min} = \frac{-\tau(T_{hot} - T_{cold})}{\sqrt{\mathbf{w} \cdot \mathbf{w}}} + T_0. \tag{3.9}$$

For an observation of duration $t_f - t_0$, these limiting values for T_f correspond to equilibrium temperatures of

$$T_{e,max} = \min \left\{ \frac{\tau(T_{hot} - T_{cold})}{(1 - e^{-k(t_f - t_0)})\sqrt{\mathbf{w} \cdot \mathbf{w}}} + T_0,\, T_{hot} \right\} \tag{3.10}$$

and

$$T_{e,min} = \max \left\{ \frac{-\tau(T_{hot} - T_{cold})}{(1 - e^{-k(t_f - t_0)})\sqrt{\mathbf{w} \cdot \mathbf{w}}} + T_0,\, T_{cold} \right\}, \tag{3.11}$$

respectively, where the additional restrictions ensure that the temperature remains within the range $[T_{cold}, T_{hot}]$. Substituting these equilibrium temperatures into Equation (3.1), we find that the maximum and minimum sun angles are

$$\phi_{max} = \frac{-b - \sqrt{b^2 - 4a(c - T_{e,min})}}{2a} \tag{3.12}$$

$$\phi_{min} = \frac{-b - \sqrt{b^2 - 4a(c - T_{e,max})}}{2a}. \tag{3.13}$$

As a result, Equation (3.5) is satisfied if $\phi \in [\phi_{min}, \phi_{max}]$. For instance, suppose we wish to keep the WFE change below 10 nm for observations up to 2 days in length. Then, for $T_0 = 50.05$ K, observations are allowed at sun angles between 85° and 131°, using our thermal

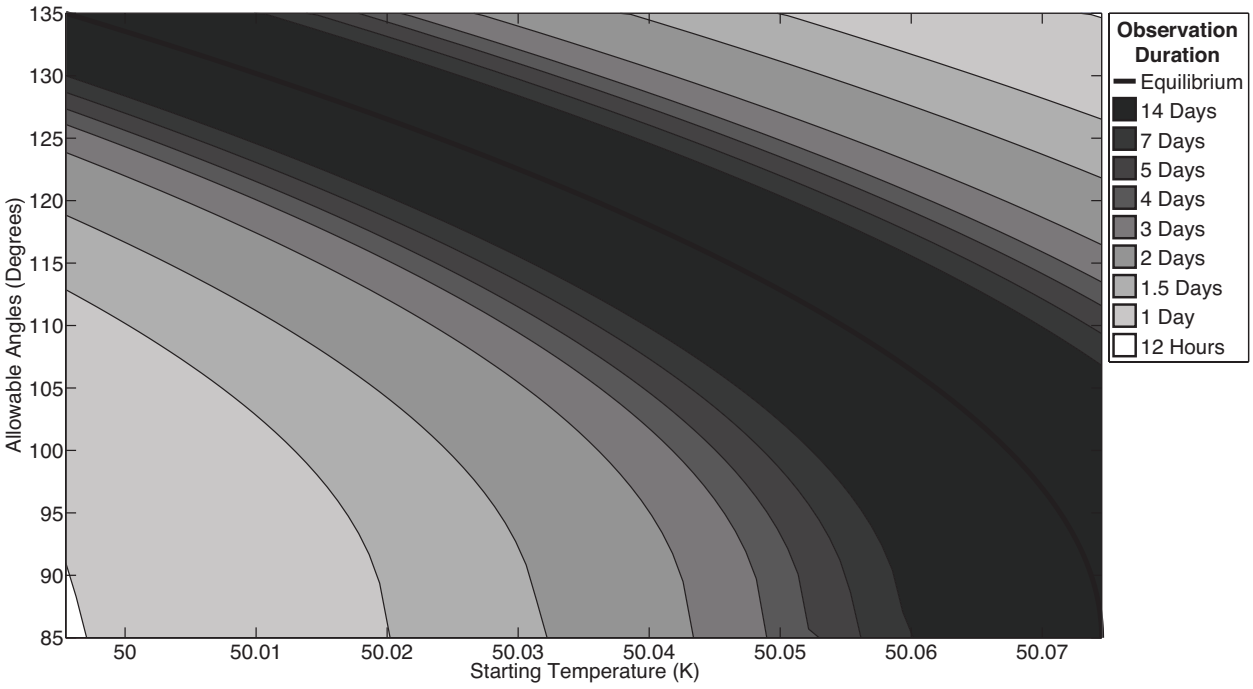

Figure 3.3: Restricting the WFE change during an observation. Since the WFE perturbations are driven by changes in the sun angle ϕ, we can control the WFE passively by introducing scheduling constraints. To limit the WFE change during an observation, we require that $\phi \in [\phi_{min}, \phi_{max}]$, where ϕ_{min} and ϕ_{max} depend on the equilibrium angle ϕ_{eq} associated with the temperature at the start of the observation, T_0. These restrictions limit the size of slews from ϕ_{eq}, with the excluded sun angles requiring larger slews. Since the angle boundaries approach ϕ_{eq} as the observation duration increases, the entire field of regard remains accessible regardless of the observation duration, provided that T_0 is consistent with the restrictions. Conversely, for an arbitrary starting temperature T_0, the entire field of regard can be observed if the observation duration is sufficiently brief. As an example, the plotted constraints ensure that the WFE changes by no more than 10 nm during an observation.

model. In general, the allowed sun angles vary depending on the initial temperature and observation duration, as shown in Figure 3.3.

Similarly, to keep the RMS WFE below τ at all times, we require that the temperature remain within the bounds that correspond to the maximum allowable WFE. Since we have selected T_{cold} as the reference temperature, we know that $T_{min} = T_{cold}$, so $\phi_{max} = 135°$.

In this case, we only need to find ϕ_{min}. Using Equation (3.4), we can write the WFE requirement as

$$\frac{T_f - T_{cold}}{T_{hot} - T_{cold}} \sqrt{\mathbf{w} \cdot \mathbf{w}} \leq \tau. \tag{3.14}$$

Solving for T_f, we find that the temperature requirement is

$$T_f \in [T_{min}, T_{max}], \tag{3.15}$$

where

$$T_{max} = \frac{\tau(T_{hot} - T_{cold})}{\sqrt{\mathbf{w} \cdot \mathbf{w}}} + T_{cold}. \tag{3.16}$$

For an observation of duration $t_f - t_0$, T_{max} corresponds to an equilibrium temperature of

$$T_e = \min \left\{ \frac{T_{max} - T_0 e^{-k(t_f - t_0)}}{1 - e^{-k(t_f - t_0)}}, T_{hot} \right\} \tag{3.17}$$

and a minimum sun angle of

$$\phi_{min} = \frac{-b - \sqrt{b^2 - 4a(c - T_e)}}{2a}. \tag{3.18}$$

Although short-duration observations are allowed under either set of angle restrictions using our thermal model and $\tau = 10$ nm, the different approaches exclude different regions of the sky as the observation duration increases. For the first approach, restricting the WFE change during an observation, the range of allowable sun angles depends upon the equilibrium sun angle ϕ_{eq} associated with the initial temperature, with excluded sun angles corresponding to large slews from ϕ_{eq} as shown in Figure 3.3. (The actual slew size required to reach one of the allowable sun angles may vary: the sun angle during the previous observation is not necessarily near ϕ_{eq} since the telescope is rarely in thermal equilibrium.) As the observation duration increases, the difference between the initial and limiting temperatures must decrease

in order to satisfy the temperature requirement, so the angle boundaries approach ϕ_{eq}. As a result, any part of the sky remains accessible regardless of the observation duration, provided that the initial temperature is consistent with the restrictions. These angle restrictions also allow more of the sky at hotter attitudes due to the quadratic model for T_e [Equation (3.1)]; since T_e changes less rapidly near the hottest attitude, larger slews from ϕ_{eq} can be tolerated. By comparison, the second restriction approach preferentially excludes attitudes that are further from the reference attitude. Although the entire sky is accessible for typical short observations in our example, the scheduling constraints restrict the field of regard as the observation duration increases, which can decrease the scheduling efficiency and potentially preclude some observations. As a result, it may be more practical to use the restrictions derived from limiting the WFE change during an observation.

Although incorporating sun angle restrictions in the observing schedule is a promising technique for passively controlling the WFE, in practice this method would be complicated to implement given the many other constraints that must be considered as part of scheduling.[68] Detailed simulations of mission scheduling are beyond the scope of this paper, but any potential implementation of this method would need to carefully assess the efficiency impacts from the additional constraints.

3.4 Limiting the WFE Using Optical Control

Although the active control algorithms for ground telescopes are typically variations on classical control laws,[53,69–72] the control problem for an active space telescope is more naturally expressed as a hybrid control problem. Hybrid systems consist of both continuous and

discrete subsystems that interact, and they come in many forms.[73–78] As an example, the interaction between the temperature in a room and a thermostat constitutes a hybrid system: the continuous temperature dynamics are affected by the discrete dynamics of the thermostat, which turns on and off depending on the temperature.[73] Other hybrid control applications include manufacturing processes,[79] aircraft collision avoidance,[80] automated highway systems,[81] automotive engine control,[82] life support systems for manned space exploration,[83] and allocating water based on seasonal snowmelt cycles.[84]

In the case of an active space telescope, the continuous WFE evolution is affected by both discrete and continuous dynamics even in the absence of optical control. In the uncontrolled case, the WFE is directly proportional to the temperature [Equation (3.4)], and the continuous temperature dynamics are affected by the start of a new observation; changes in the sun angle alter the exponential. When optical control is added, the WFE is the sum of the temperature-induced error $\mathbf{W}(T)$ and the control vector $\mathbf{u}$:

$$\mathbf{W} = \mathbf{W}(T) + \mathbf{u}. \tag{3.19}$$

This control vector is updated at discrete times rather than continuously, with the corrections $\mathbf{u_c}$ determined by the specific control algorithm:

$$\mathbf{u}(j) = \mathbf{u}(j-1) + \mathbf{u_c}. \tag{3.20}$$

Although the wavefront control process could be fully automated in theory, we will consider the case where ground intervention is required because this adds the complication of time delays and is the case for JWST.[85] In this scenario, wavefront measurements are sent from the spacecraft to a ground station for analysis, after which a new set of commands, including any wavefront corrections, is sent to the spacecraft. Two time delays account for

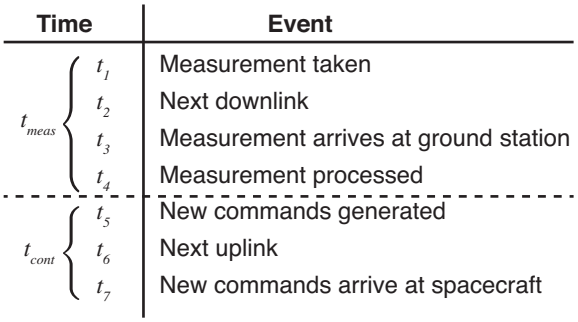

Figure 3.4: Time delay definitions. In the wavefront control process, new measurements are sent to the ground for analysis, after which updated commands, including revised wavefront corrections, are sent to the spacecraft. Two time delays account for the total amount of time that elapses during this process: t_{meas} accounts for the time required for wavefront measurements to be sent to the ground and processed, and t_{cont} accounts for the time required for a set of commands to be sent to the spacecraft.

the total amount of time that elapses during this process (Figure 3.4). The first delay, t_{meas}, accounts for the time required for wavefront measurements to be sent from the spacecraft and processed on the ground. The second delay, t_{cont}, accounts for the time required for a set of commands to be sent to the spacecraft. It is assumed that no new measurements are taken until after both delays have passed.

In addition to time delays, the wavefront control process can also be complicated by the presence of noise. Due to the hybrid nature of the control problem and the relative infrequency of the wavefront measurements, this noise is not readily handled by applying classical approaches such as a Kalman filter; this is a case where the model itself changes faster than the measurements are taken. At the start of each observation, the change in sun angle alters the equilibrium temperature, which in turn alters the temperature and wavefront trajectories. Since wavefront measurements are taken every few days, while typical observations last a few hours, the wavefront trajectory can switch many times between measurements. As a result, it is not trivial to estimate the true wavefront evolution using a sequence of noisy measurements.

To investigate the optical performance that can be achieved with infrequent wavefront control, we have evaluated three control algorithms according to two competing metrics: the number of actuator moves and the amount of time spent over the correction threshold. Two of these algorithms are variations on the baseline control scheme for JWST, and the third is our predictive controller that uses an internal temperature and wavefront model to determine in advance when corrections will be needed (Section 3.4.2). Using multiple observing schedules (Section 3.4.1), we compare these algorithms under a variety of assumed conditions, including cases with noise and model error (Section 3.4.3). These comparisons show that while all three algorithms successfully maintain the wavefront even with substantial measurement noise, the predictive controller generally provides the best performance.

3.4.1 Mission Schedules

To assess the strengths and weaknesses of wavefront control algorithms, it is useful to consider two types of schedules: simple schedules that are easily understood and more realistic schedules that approximate the types of observations expected on orbit. In the simulations that follow, we will use square wave schedules as well as schedules based on the Science Operations Design Reference Mission (SODRM) 2013 schedules for JWST.[68] The square wave schedules represent repeated worst-case slews, with the observatory oscillating between the hottest and coldest attitudes with a period of 1 to 56 days [Figure 3.5(a)]. Since we assume that the attitude changes occur instantaneously, these schedules consider the worst-case thermal changes for each period. In contrast, the SODRM-based schedules simulate more realistic hypothetical mission scenarios based on a detailed population of candidate observations. We consider fifteen realizations of the sample mission schedules, which repre-

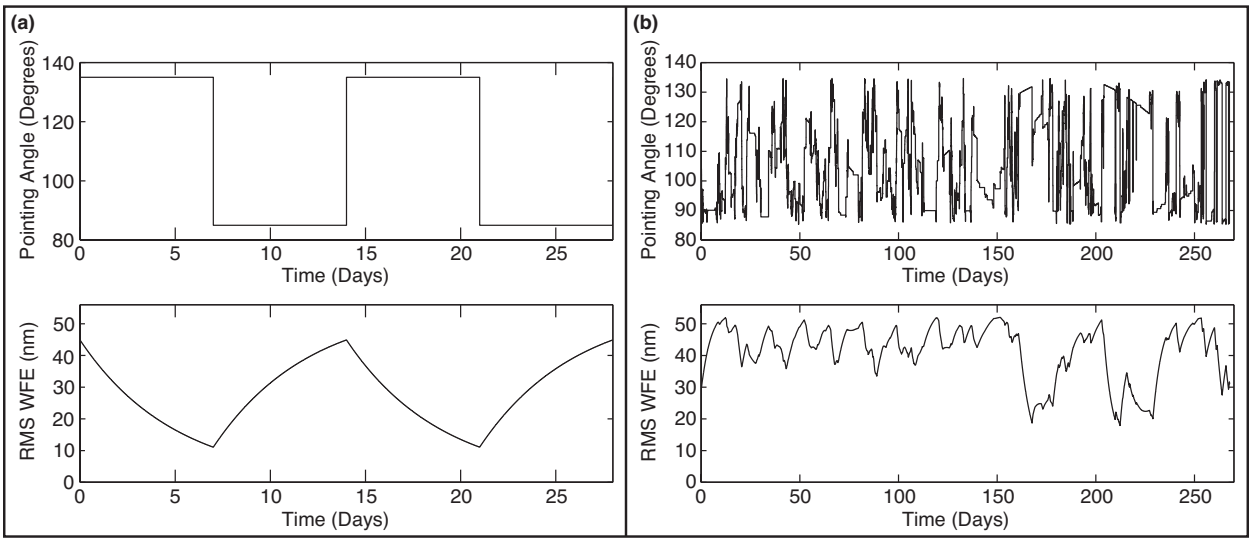

Figure 3.5: Mission schedules. To evaluate the performance of the wavefront control algorithms, we consider two types of schedules: square wave schedules that represent repeated worst-case slews between the hottest and coldest attitudes (a), and hypothetical mission schedules based on the SODRM schedules for JWST[68] (b). Fifteen such SODRM schedules were provided to us by the JWST planning and scheduling system developers.

sent different orderings of the same underlying pool of observations; an example is shown in Figure 3.5(b).

3.4.2 Control Schemes

For an active space telescope, the WFE evolution depends upon the control scheme in addition to schedule parameters such as the sun angle changes and the observation durations. Control schemes that use a sequence of wavefront measurements to correct excursions at regular intervals, for example, perform differently than schemes that preemptively correct the wavefront before the error exceeds a desired limit. To investigate the effectiveness of each approach, we have developed three control algorithms: baseline and averaging algorithms

that correct every two weeks as needed, and a predictive algorithm that uses an internal model to determine in advance when corrections will be needed.

Baseline and Averaging Algorithms

For the baseline and averaging algorithms, we use a control scheme that is similar to the baseline scheme for JWST.[55] The wavefront error is measured every two days, and the measurements taken during the last two-week period are used to determine if a correction is needed. For the baseline algorithm, only the most recent measurement $\mathbf{W_{m7}}$ is used. At the end of each control period, the RMS WFE from $\mathbf{W_{m7}}$ is compared against the correction threshold τ, and if the error exceeds τ, a correction is sent to the spacecraft [Figure 3.6(a)]. This correction consists of the additive inverse of $\mathbf{W_{m7}}$:

$$\mathbf{u_c} = \begin{cases} -\mathbf{W_{m7}} & \text{if } \sqrt{\mathbf{W_{m7}} \cdot \mathbf{W_{m7}}} \geq \tau, \\ \mathbf{0} & \text{otherwise.} \end{cases} \tag{3.21}$$

This algorithm is analogous to the classical feedback control laws that are typically used to actively control large ground telescopes;[69–72] it is similar to a proportional controller with a logic-driven gain operating on a two-week timescale rather than continuously. It may seem inefficient or overly simplistic to simply discard six out of seven measurements. However, given the time-variable wavefront evolution as noted above, it is not straightforward to combine measurements from different times, and how to do so for JWST has not yet been specified. This scenario intentionally represents a simplest possible algorithm against which we can compare more sophisticated approaches.

The averaging algorithm, on the other hand, uses all of the wavefront measurements

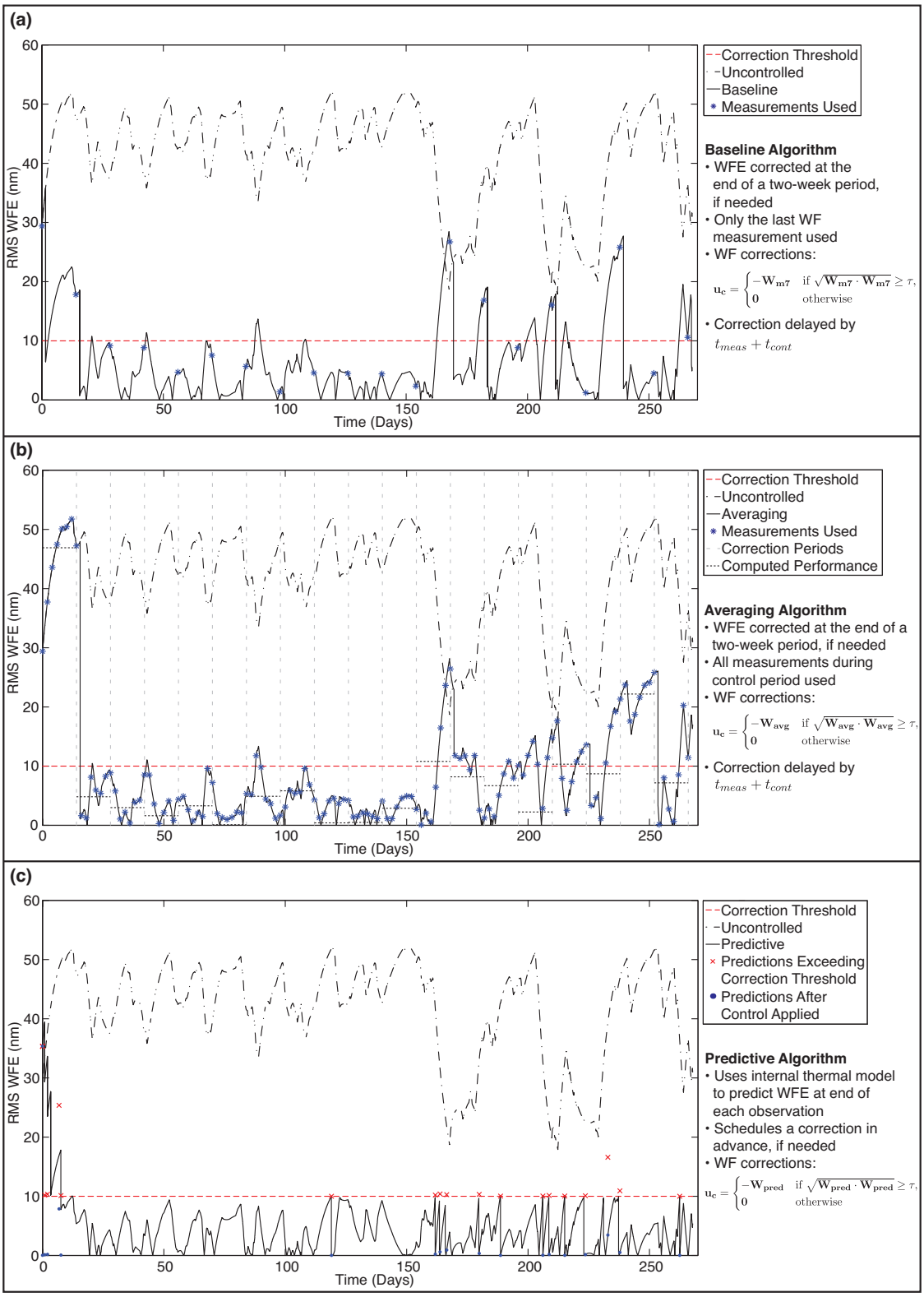

Figure 3.6: The wavefront control algorithms

taken during the last control period. These measurements are used to construct a vector of the average wavefront coefficients during the last two weeks, $\mathbf{W_{avg}}$, and a correction is issued if the corresponding RMS WFE exceeds τ [Figure 3.6(b)]. This correction consists of the additive inverse of $\mathbf{W_{avg}}$:

$$\mathbf{W_{avg}} = \begin{bmatrix} mean(W_{m1_1}, W_{m2_1}, W_{m3_1}, \ldots, W_{m7_1}) \\ mean(W_{m1_2}, W_{m2_2}, W_{m3_2}, \ldots, W_{m7_2}) \\ \vdots \\ mean(W_{m1_8}, W_{m2_8}, W_{m3_8}, \ldots, W_{m7_8}) \end{bmatrix} \tag{3.22}$$

$$\mathbf{u_c} = \begin{cases} -\mathbf{W_{avg}} & \text{if } \sqrt{\mathbf{W_{avg}} \cdot \mathbf{W_{avg}}} \geq \tau, \\ \mathbf{0} & \text{otherwise.} \end{cases} \tag{3.23}$$

Since the baseline and averaging algorithms use a sequence of measurements to determine if a correction is required, there is an implicit assumption that the wavefront error during the previous correction period is representative of the wavefront error during the upcoming period. As a result, these algorithms are expected to perform best in situations where the wavefront error variation is low relative to τ. It is also worth noting that these algorithms issue corrections only *after* the RMS WFE has exceeded τ, and these corrections are delayed by $t_{meas} + t_{cont}$.

Predictive Algorithm

Since the wavefront perturbations are a byproduct of the observing schedule, it is possible to predict when the WFE will exceed the correction threshold and to schedule an appropriate correction in advance. Due to the hybrid nature of the system model, we have developed

a hybrid predictive controller rather than using a classical predictive control algorithm.[86] Our algorithm uses knowledge of the observing schedule and an internal thermal model to predict the WFE at the end of each observation, and it schedules a correction whenever the prediction exceeds the threshold. The algorithm also has the option of updating its internal model as wavefront and/or temperature measurements are taken in order to improve the accuracy of its predictions.

In practice, the predictive control algorithm would likely reside at a ground station, where it would be used to generate a set of predictions up through a preset time rather than in real time. For instance, predictions could be generated for the next two weeks as part of the preparation of short-term schedules. As new measurements became available, the algorithm would update its internal model and generate a set of revised predictions. Since any new instructions arrive at the spacecraft after a total delay of $t_{meas} + t_{cont}$, it would be particularly convenient to generate a set of predictions from $t = t_{m1} + t_{meas} + t_{cont}$ to $t = t_{m2} + t_{meas} + t_{cont}$, where t_{m1} and t_{m2} are the times at which the most recent measurement and the next scheduled measurement are taken, respectively [Figure 3.6(c)].

For simulations, the repeated calculations associated with model updates are unnecessarily inefficient, and it is advantageous to structure the predictive control algorithm differently. Due to the time delays, a measurement can be available for use on the ground, on the spacecraft, or neither. As a result, there are three possible information availability states s if only one measurement type is used for model updates,

$$s \in S = \Big\{\text{unavailable}, \quad \text{available on ground}, \quad \text{available on ground and spacecraft}\Big\},$$

and nine possible states if both temperature and wavefront measurements are used,

$$s \in S_{temp} \times S_{WFE}.$$

For control purposes, only the information available to the spacecraft matters–while new predictions can be generated on the ground as soon as a measurement is received, this updated model cannot be used to alter the wavefront for observations occurring between times t_m+t_{meas} and $t_m+t_{meas}+t_{cont}$. To track the flow of information throughout the system, our implementation of the predictive controller contains nine submodels, each containing the information available to the ground station and the spacecraft for one of the information states. A logic framework tracks the information state of the system and identifies the appropriate submodel to use; this framework also updates the submodels appropriately as the various delays pass. We emphasize that this approach is a computational convenience to speed simulations by considering all cases in parallel, not a required architecture.

At the beginning of an observation, the predictive controller uses the information available to the spacecraft to predict the temperature and wavefront error at the end of the observation. The prediction model has the same basic structure as the physical model presented in Section 3.2, although it is more convenient to write the prediction for the thermally induced wavefront coeffients, $\mathbf{W_{pred}}(T_{pred})$, in slope-intercept form to allow for model updates:

$$T_{pred} = (T_{0,pred} - T_e)e^{-k_{pred}(t_f - t_0)} + T_e \tag{3.24}$$

$$\mathbf{W_{pred}} = \mathbf{W_{pred}}(T_{pred}) + \mathbf{u} = T_{pred}\mathbf{m_{pred}} + \mathbf{o_{pred}} + \mathbf{u} \tag{3.25}$$

where $\mathbf{m_{pred}}$ and $\mathbf{o_{pred}}$ are the slopes and offsets, respectively, for the lines relating the temperature to the wavefront coefficients. It is important to note that the model parameters, such as the equilibrium temperatures and the thermal time constant, that are used in the predictive controller's model will not in general be exactly equal to the true values representing the behavior of the spacecraft. We investigate in Section 3.4.3 cases of substantial error in the model parameters.

If the wavefront error prediction exceeds the correction threshold τ, a correction is determined and applied. (In our simulation framework there is no need to wait for a delay to pass since all delays have been incorporated in the model structure.) The wavefront correction can take several forms, including the additive inverse of the predicted wavefront coefficients at the start, end, or midpoint of the observation. We use the predicted wavefront coefficients $\mathbf{W_{pred}}$ at the time half of the WFE change during the observation has occurred, t_{midW}:

$$\mathbf{u_c} = \begin{cases} -\mathbf{W_{pred}}(t_{midW}) & \text{if } \sqrt{\mathbf{W_{pred}}(t_f) \cdot \mathbf{W_{pred}}(t_f)} \geq \tau, \\ \mathbf{0} & \text{otherwise.} \end{cases} \tag{3.26}$$

To allow for independent temperature and wavefront model updates, our implementation of the predictive controller is structured such that the temperature model updates as temperature measurements become available, and $\mathbf{m_{pred}}$ and $\mathbf{o_{pred}}$ update as wavefront measurements become available. For a temperature update, T_{pred} is reset to match either the last measurement or the output of a state estimator. For a wavefront update, the last N wavefront measurements and the corresponding temperature predictions are used to calculate the best-fit line for each wavefront coefficient; $\mathbf{m_{pred}}$ and $\mathbf{o_{pred}}$ are then reset to match the slopes and offsets for these lines. In this paper, we concentrate on using wavefront measurements only since that is the case relevant to JWST,[85] although in general, temperature measurements could also be incorporated if the temperature sensors on the spacecraft and telescope were sufficiently precise.

3.4.3 Comparisons of Algorithm Performance

The performance of a wavefront control algorithm depends on the input schedule; control parameters, such as the sensing frequency and the correction threshold; and sources of error, including wavefront sensing noise and model error. To investigate the impact of each of these factors and assess the relative strengths of the control algorithms, we compare the performance of each algorithm under a variety of conditions, using a baseline correction threshold of 20 nm, which corresponds to approximately one third of the allowed wavefront variability in the absence of control for JWST.[87] As we will show, each algorithm can control the wavefront successfully, with the predictive controller generally providing the best optical performance, even in the presence of substantial noise and model error.

Performance Metrics

To evaluate the optical performance, we consider two main metrics: the amount of time the RMS WFE exceeds the correction threshold and the total number of corrections commanded. When considered together, these metrics describe how successfully an algorithm achieves the competing goals of minimizing the RMS WFE and minimizing the number of actuator moves. To neglect any transient effects associated with the simulation's initial conditions and the first corrections, these metrics are calculated for the steady-state response, which is defined as starting on Day 35 for the SODRM-based schedules; by this time, the temperature dynamics are no longer affected by the initial conditions, and the algorithms have had at least two opportunities to issue corrections.

For each simulation, we construct a time history of the RMS WFE. [We remind readers that $\mathbf{W}$ is the *differential* WFE measured with respect to the nominal alignment state as shown in Equation (3.3), not the total WFE.] To gain additional insight into the wavefront response without plotting each time history, we calculate two quantities: the mean of all the RMS WFE data points in steady-state, and the corresponding standard deviation. Taken together, these quantities describe the overall magnitude of the RMS WFE and the amount of variation during the simulation.

Effects of Observation Duration and Correction Threshold

In the absence of noise, the observation duration and the correction threshold τ determine how aggressively an algorithm must correct in order to keep the RMS WFE below τ. Longer observations create larger wavefront changes, increasing the likelihood that the RMS WFE will exceed τ by the end of the observation, and lower thresholds allow less leeway for wavefront variations before a correction is needed. As a result, the number of corrections and the amount of time spent over the correction threshold both depend on the observation frequency and τ.

To investigate how the performance is affected by the observation frequency, we consider square wave schedules with periods ranging from 1 to 56 days. In the absence of optical control, the RMS WFE for this type of schedule oscillates around the RMS WFE associated with the mean temperature [Figures 3.5(a) and 3.7(a)]:

$$mean(\sqrt{\mathbf{W}\cdot\mathbf{W}}) = \sqrt{\mathbf{W}(T_{mean})\cdot\mathbf{W}(T_{mean})} \tag{3.27}$$

where

$$T_{mean} = \frac{T_{hot} + T_{cold}}{2}. \tag{3.28}$$

As the observation duration increases, there is more time for the wavefront to evolve, leading to larger changes; this behavior is reflected in the standard deviation, which increases with wave period [Figure 3.7(b)]. For periods less than 14 days, the standard deviation is less than 10 nm, which is half the correction threshold. As a result, the RMS WFE passively remains below τ 100% of the time, and none of the control algorithms issue corrections in steady state [Figure 3.7(c, d)].

Since the baseline and averaging algorithms determine if a correction is needed at regular intervals, the optical performance for these algorithms depends on the relationship between the wave and control periods. The baseline algorithm is particularly sensitive to the timing since it uses only one measurement. When the wave and control periods are the same and in phase, for example, the baseline algorithm may issue no corrections even though the RMS WFE exceeds τ 41.6% of the time [Figure 3.7(c,d)]. It is also possible to find cases where the optical performance is worse with these algorithms than without any control, although these pathological scenarios are not expected on orbit. As an example, for a square wave schedule with a 28-day period (twice the control period) and the same phase as the control cycle, the algorithms more than double the amount of time that the RMS WFE exceeds τ despite issuing corrections at every opportunity: the RMS WFE exceeds τ 79% of the time for the averaging algorithm and 94% of the time for the baseline algorithm, compared to 36% of the time if uncontrolled. Even when the baseline and averaging algorithms improve the optical performance relative to the uncontrolled case, the time spent over the correction threshold is limited to approximately 37% at best for the periods considered.

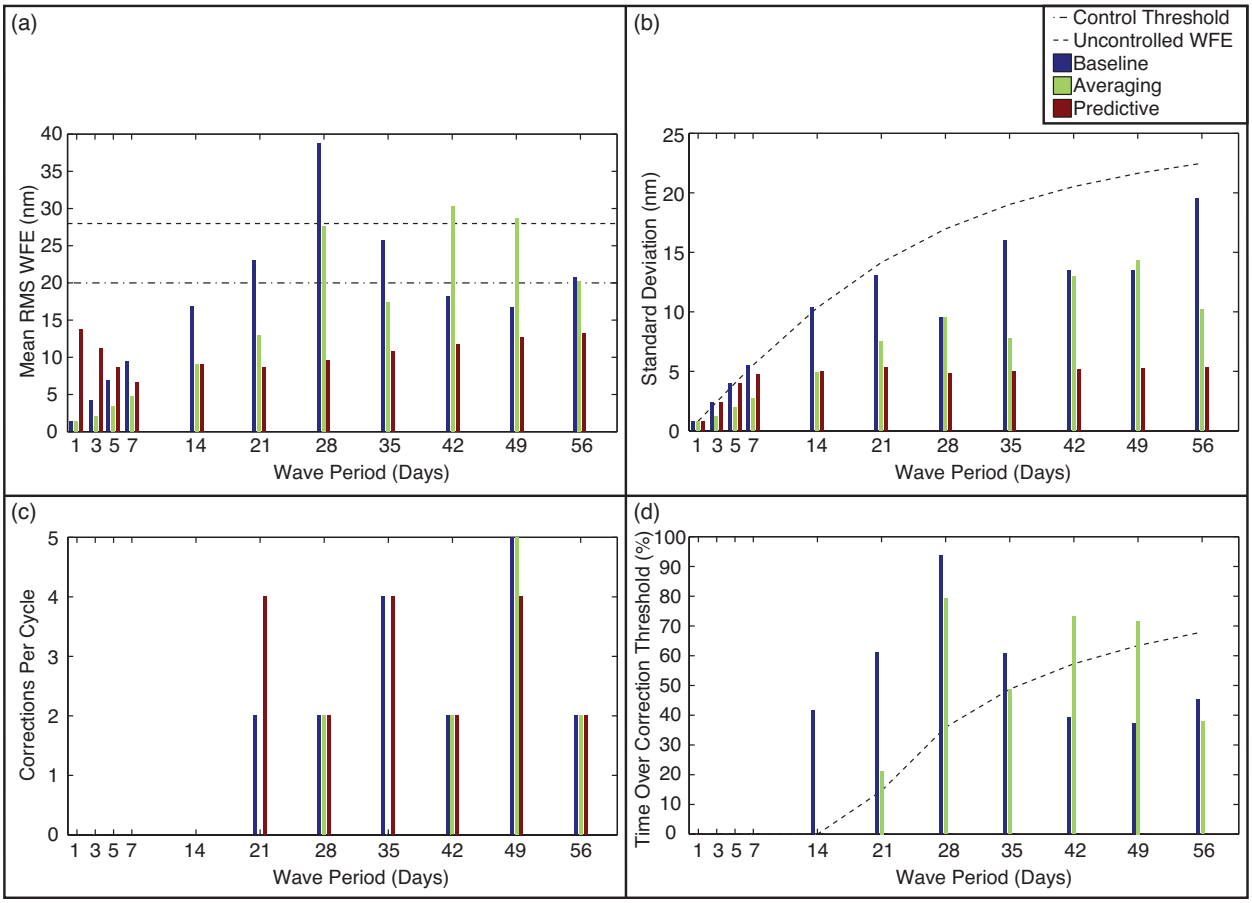

Figure 3.7: The effects of observation duration. In the absence of optical control, the RMS WFE for a square wave schedule oscillates around the RMS WFE associated with the mean temperature (a), with longer observation durations corresponding to larger WFE changes (b). For durations less than two weeks, the WFE variation is small enough that the RMS WFE remains below a correction threshold of 20 nm 100% of the time without optical control (d). As a result, none of the control algorithms issue corrections for these periods (c). [Note that the mean RMS WFE has been subtracted for the uncontrolled case in (d) since it is well known.] For periods longer than two weeks, the effectiveness of the baseline and averaging algorithms depends upon the wave period, and it is possible to find cases where the algorithms lead to worse performance than the uncontrolled case. Of the three algorithms, the predictive controller performs the best, holding the RMS WFE below τ 100% of the time for each period without requiring significantly more corrections than the other algorithms.

By comparison, the predictive algorithm consistently improves the optical performance, holding the RMS WFE below τ 100% of the time without requiring significantly more corrections than the other algorithms. The predictive algorithm achieves this performance by placing the corrections at more effective times, scheduling them for points in the observing cycle where the RMS WFE changes rapidly and is about to exceed τ. For wave periods longer than two weeks, this scheduling actually leads to a lower mean RMS WFE than the averaging algorithm (Figure 3.7).

Similarly, during the course of a sample mission, the predictive algorithm provides the best optical performance, holding the RMS WFE below τ at least 99.8% of the time on average. If we reduce τ below approximately 15 nm, the number of corrections required to maintain this performance increases significantly, from an average of 6.7 corrections at 15 nm to 53 corrections at 5 nm [Figure 3.8]. As a result, the performance of the noiseless, error-free predictive algorithm is limited only by the number of corrections that are permissible. By comparison, the performance of the averaging and baseline algorithms is limited by the two-week correction period; for thresholds less than 10 nm, these algorithms cannot correct aggressively enough to keep the RMS WFE below τ during periods where the wavefront changes rapidly, such as during long observations following large slews. Consequently, the time over the correction threshold increases as τ decreases, while the number of corrections does not change significantly for the baseline and averaging algorithms.

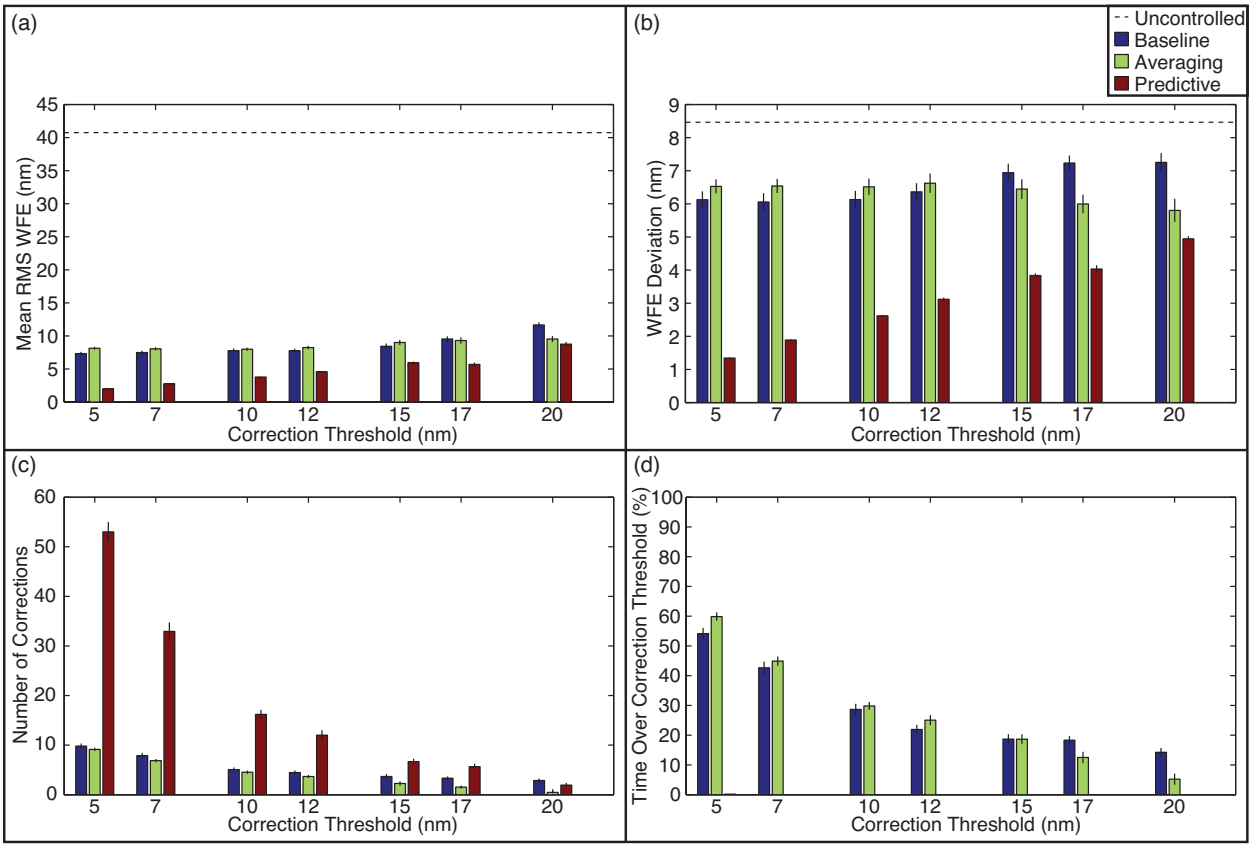

Figure 3.8: Selecting a correction threshold. For the predictive controller, the choice of correction threshold for a sample mission is limited only by the number of corrections; this algorithm holds the RMS WFE below τ at least 99.8% of the time for thresholds as low as 5 nm but requires an increasing number of corrections for $\tau < 15$ nm. For the baseline and averaging algorithms, the choice of correction threshold is limited by the correction period, which is fixed at two weeks; for $\tau < 10$ nm, these algorithms cannot correct aggressively enough to keep the RMS WFE below τ at times when the wavefront changes rapidly.

Effects of Mission Schedule

To investigate how the optical performance varies with different mission schedules, we compare the results for the fifteen SODRM-based sample mission scenarios. As shown in Table 3.1, for $\tau = 20$ nm the predictive algorithm consistently holds the RMS WFE below τ 100% of the time, requiring 0-5 corrections depending on the schedule. This consistency is to be expected since the predictive algorithm is designed to correct the wavefront before the RMS WFE exceeds τ; it may, however, require a different number of corrections to achieve this performance depending on the specific schedule.

The performance of the baseline and averaging algorithms, by comparison, can vary considerably with schedule since these algorithms rely on a sequence of measurements to determine when a correction is required. The wavefront measurements taken during a two-week period are not always representative of the wavefront during the next two-week period, and the wavefront error can at times temporarily exceed τ in between measurements without affecting the correction schedule. The baseline algorithm is particularly sensitive to the measurement timing since it uses only a single measurement, and it generally provides the worst performance. For the fifteen schedules considered, the baseline and averaging algorithms hold the RMS WFE below τ 75.4-93.0% and 78.1-100% of the time, respectively (Table 3.1).

Table 3.1: Baseline, averaging, and predictive algorithm performance for the sample mission scenarios

	Number of Corrections			Time Over τ (%)		
	Baseline	Averaging	Predictive	Baseline	Averaging	Predictive
	2	0	5	12.4	4.9	0
	3	0	4	16.4	0.7	0
	5	0	0	24.6	0	0
	3	1	0	13.2	21.9	0
	5	0	0	21.9	0	0
	4	0	3	9.4	2.1	0
	1	0	0	12.0	0	0
	3	0	2	11.8	3.1	0
	0	0	0	7.0	0.1	0
	1	0	2	7.2	3.1	0
	2	2	4	7.6	15.8	0
	3	0	1	15.1	0	0
	3	0	2	21.7	0.5	0
	3	2	4	14.2	9.3	0
	5	2	2	19.3	16.7	0
Average	2.9	0.5	1.9	14.3	5.2	0

Although the baseline and averaging algorithms are sensitive to the choice of mission schedule, it is not straightforward to predict whether a given schedule will prove challenging. As an example, for the schedules considered, the averaging algorithm in the best case holds the RMS WFE below τ 100% of the time without issuing any corrections in steady-state. However, at least one of these "best" schedules contains larger wavefront changes than the schedule with the worst performance [Figure 3.9(a)]. Similarly, the best schedule for the baseline algorithm contains larger wavefront changes than the worst schedule [Figure 3.9(b)]. In general, it appears that the measurement timing is particularly important for the baseline and averaging algorithms. Adjusting this timing based on knowledge of the observing schedule may improve the performance, but the resulting algorithm would begin to resemble the predictive algorithm. To some extent these behaviors just reflect the relatively simple definitions of the baseline and averaging algorithms, and point toward the need for a

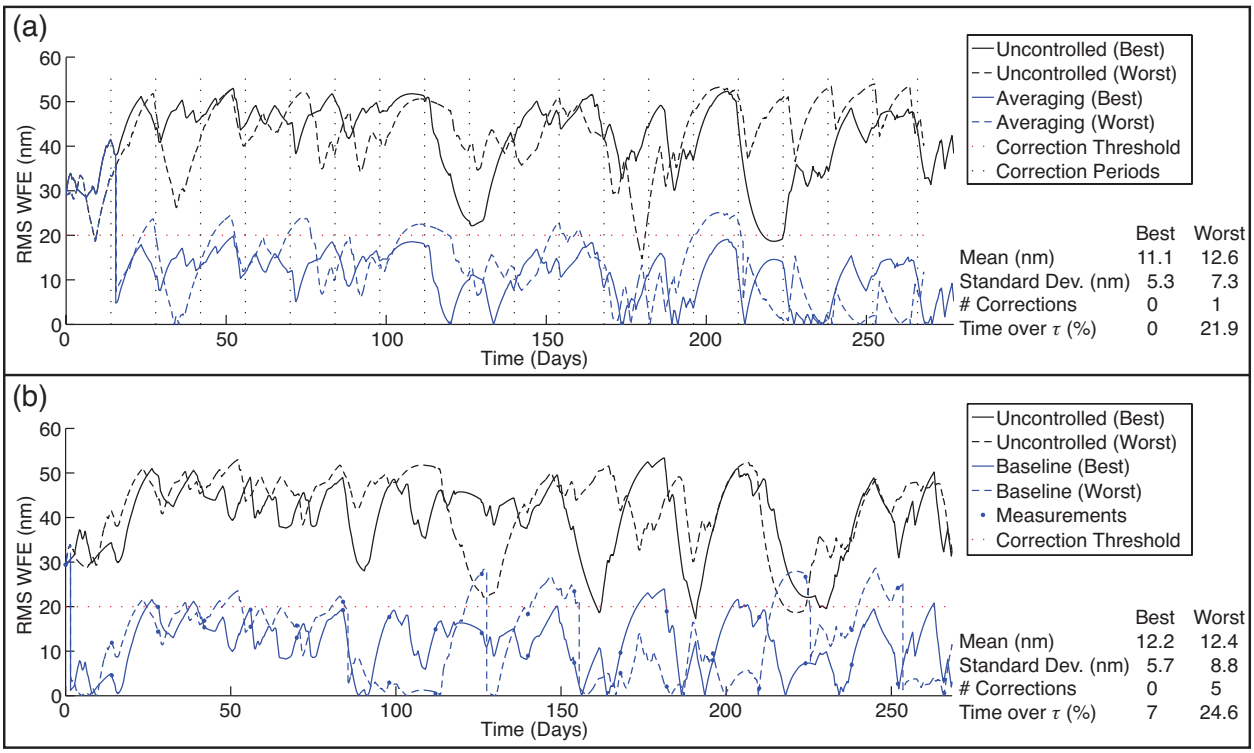

Figure 3.9: Sensitivity to the mission schedule. Since the baseline and averaging algorithms use a sequence of wavefront measurements to determine when a correction is required, they are sensitive to the measurement timing, and their performance can vary considerably for different mission schedules. For the fifteen schedules considered, the averaging and baseline algorithms hold the RMS WFE below τ 78.1-100% and 75.4-93.0% of the time, respectively. It is not straightforward to predict whether a given schedule will prove challenging. One of the best schedules for the averaging algorithm contains larger changes than the worst schedule (a), and the same is true for the baseline algorithm (b).

more nuanced approach like the predictive algorithm.

Effects of Wavefront Sensing Noise

Although wavefront sensing noise can introduce errors in the correction process, the three control algorithms are not explicitly designed for noise rejection. To investigate whether these algorithms are sensitive to noise as a result, we add zero-mean Gaussian noise to each measurement taken during the sample mission scenarios. This noise is randomly distributed across all of the Zernike coefficients and has a standard deviation of 1, 5, or 10 nm. Twenty-five trials are conducted for each noise case and averaged together to obtain the final result.

When the performance is averaged over all of the sample schedules, all of the algorithms successfully hold the RMS WFE below $\tau = 20$ nm at least 80% of the time, even when the noise level is equal to half the correction threshold (Figure 3.10). Of the three algorithms, the baseline algorithm typically provides the worst performance, holding the RMS WFE below τ 87% of the time at best, compared to 95% of the time for the averaging algorithm and 92-100% for the predictive algorithm. The averaging algorithm is least affected by the noise, spending approximately the same amount of time over the correction threshold and issuing the same number of corrections in each case. This behavior is to be expected since the mean RMS WFE during a correction period is relatively unaffected by zero-mean noise. The predictive algorithm, by comparison, generally provides the best optical performance, holding the RMS WFE below τ over 98% of the time even with measurement noise levels as high as 5 nm.

If the noise level is increased to 10 nm, the relative performance of the predictive and averaging algorithms depends on the specific mission scenario. The predictive algorithm achieves a lower time over the correction threshold for 33% of the scenarios we considered.

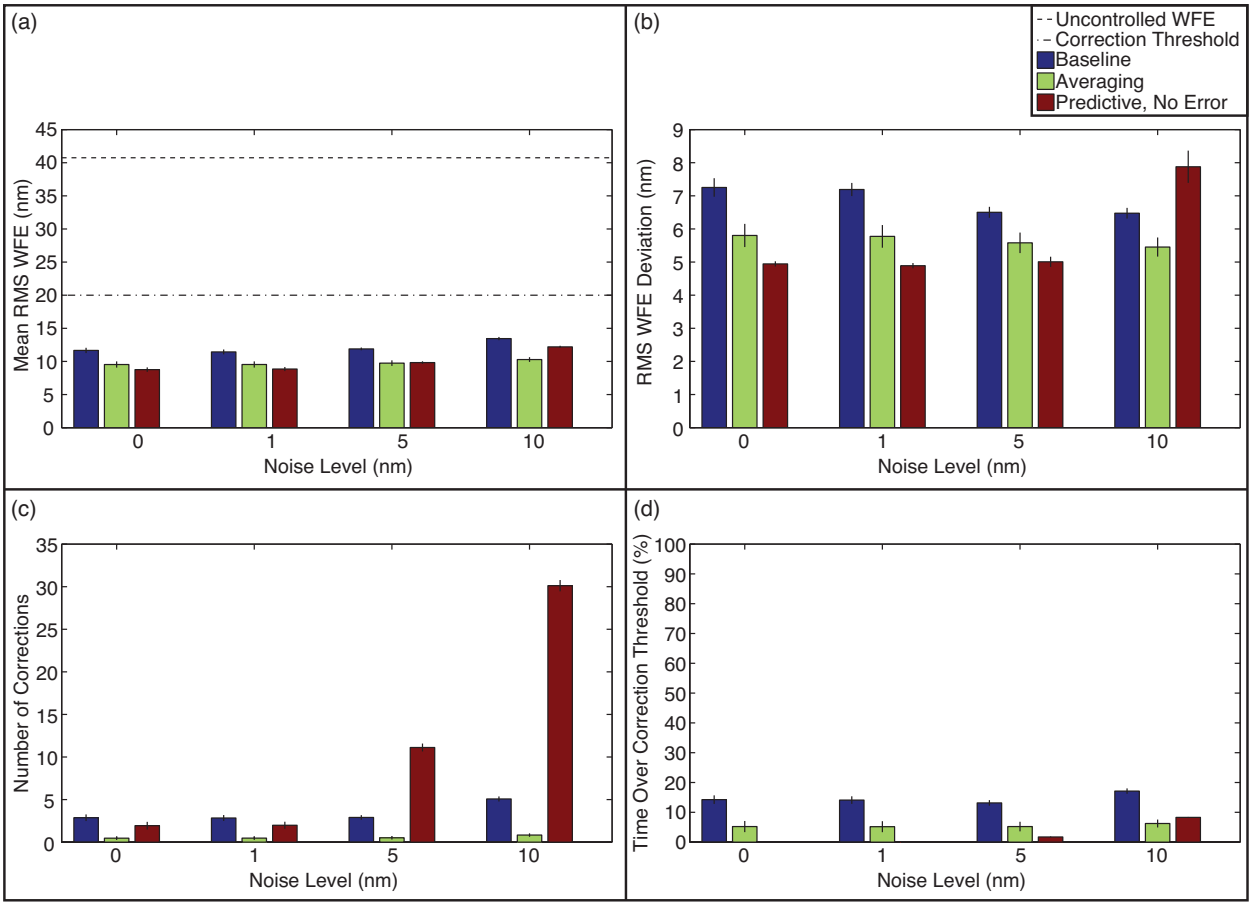

Figure 3.10: Sensitivity to noise (averaged over all schedules). Although the three control algorithms are not explicitly designed for noise rejection, they all successfully hold the RMS WFE below τ at least 80% of the time on average, even when the noise level equals half the correction threshold. The averaging algorithm is the least sensitive to noise, performing comparably in each scenario, while the predictive algorithm generally provides the best optical performance. However, the predictive algorithm is sensitive to noise, requiring significantly more corrections as the noise level increases. For 10 nm noise, the relative performance of the predictive and averaging algorithms depends on the specific schedule.

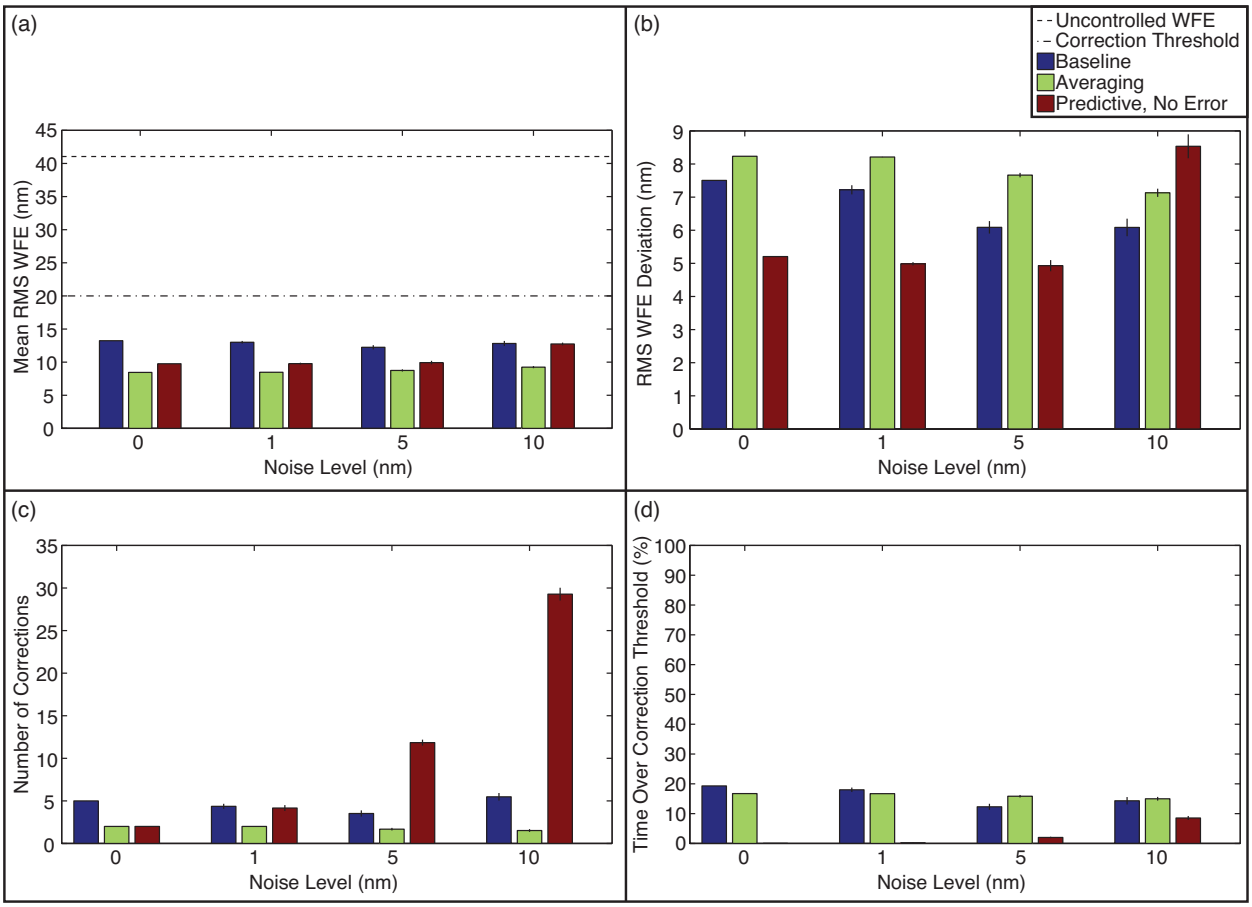

Figure 3.11: Sensitivity to noise (sample schedule). Although the predictive algorithm is sensitive to noise, it can outperform the averaging algorithm even with substantial measurement noise. For the schedule shown in Figure 3.5(b), the predictive algorithm with 10 nm noise holds the RMS WFE below τ 91% of the time, while the averaging algorithm achieves only about 85% at best.

As an example, for the schedule shown in Figure 3.5(b), the predictive algorithm holds the RMS WFE below τ 100% of the time in the absence of noise, but drops to 91% as 10 nm noise is added (Figure 3.11). In this case, the predictive controller even with noise performs much better than the averaging controller with zero noise, which achieves only 83% of the time under the threshold.

While the averaging algorithm is sensitive to schedule and insensitive to noise, the re-

verse is true for the predictive algorithm. As the noise level increases, the predictive controller works harder to maintain the wavefront, issuing significantly more corrections [Figures 3.10(c) and 3.11(c)]. The aggressive correction schedule also leads to higher variation in the RMS WFE [Figures 3.10(b) and 3.11(b)]. Our implementation of the predictive controller is sensitive to noise since it uses all of the last N wavefront measurements to update its internal temperature-to-wavefront model; one particularly noisy measurement can affect the accuracy of subsequent wavefront error predictions (Section 3.4.2). More sophisticated model update schemes, which discard outlying measurements or incorporate an estimate of the noise statistics, for example, or adding a gain to Equation (3.26) may lessen the predictive algorithm's sensitivity to noise, but that is beyond the scope of this paper.

Effects of Predictive Model Error

Since the predictive controller relies on an internal model to determine when corrections will be needed, the corrections issued and their timing can be affected by errors in model parameters such as the thermal decay constant k. The physical effect of an error in the model's k depends upon its sign: for positive errors, the model predicts more rapid temperature changes than actually take place, while for negative errors, the model predicts more gradual changes. This difference can affect the optical performance, depending on the implementation of the predictive controller.

For a purely predictive controller that has the correct temperature-to-wavefront model [Equation (3.25)] and does not use any measurements to update its internal thermal and wavefront model, the different signs affect the optical performance asymmetrically. For positive errors, the more rapid changes in the predicted temperature correspond directly to

more rapid changes in the predicted wavefront error, so the controller issues corrections more aggressively than strictly necessary. In this case, the controller issues corrections somewhat before τ is exceeded and overcorrects. For negative errors, the slower changes in the predicted temperature mean that the predicted wavefront changes too slowly, so the RMS WFE may exceed the correction threshold. As a result, the optical performance is less sensitive to positive errors; the penalty for positive errors is a more aggressive correction schedule, while the penalty for negative errors is more time spent over the correction threshold. Therefore in the situation where the observatory's true thermal decay constant is not measured precisely, but the relationship between the temperature and the WFE is relatively well known, it may provide better performance to assume a decay constant near the upper end of the uncertainty range.

For a predictive controller that uses wavefront measurements to update its internal temperature-to-wavefront model, the effects of positive and negative k errors can be more symmetric. In our implementation of the predictive controller, the wavefront measurements are used to adjust the slopes and offsets for the lines relating the predicted temperature to the wavefront coefficients, as described in Section 3.4.2. As a result, the controller attempts to compensate for the k error by adjusting its linear temperature-to-wavefront model. Typically, these adjustments lead to higher-magnitude slopes and lower-magnitude offsets for negative errors, and the reverse for positive errors. Consequently, for each error type, there are temperatures for which the predictive controller overestimates the wavefront change as well as temperatures for which the predictive controller underestimates the wavefront change, and these temperatures change with each model update. As a result, there is no clear preference for positive or negative errors when the optical performance is averaged over multiple mission schedules, as shown in Figure 3.12. It is expected that the predictive controller would similarly attempt to compensate for other model errors, such as incorrect equilibrium

temperatures, although these cases have not been investigated in detail yet.

It is clearly advantageous for a predictive controller to have an internal model of the observatory that is as accurate as possible, yet the results in Figure 3.12 also show that the predictive controller can tolerate significant discrepancies between the model and the as-built performance while still delivering superior wavefront control. For the sample mission scenarios, the predictive controller successfully functions with k errors as high as 25%, which corresponds to a modeled time constant one day shorter than the actual time constant, and as low as -25%. The k error mostly affects the amount of time that the RMS WFE exceeds the correction threshold, and the effects are more pronounced at lower thresholds since there is less room for the RMS WFE to vary before exceeding τ. For $\tau = 20$ nm, the error has little effect on the optical performance: the 25% error, -25% error, and error-free controllers issue approximately the same number of corrections and spend approximately the same amount of time over τ. If we decrease τ to 5 nm, the controllers still issue approximately the same number of corrections, but the amount of time over τ increases with the magnitude of the k error. However, even in this case, the predictive controllers all spend less than 7% of the time over τ, compared to more than 50% for the baseline and averaging algorithms (Figure 3.8).

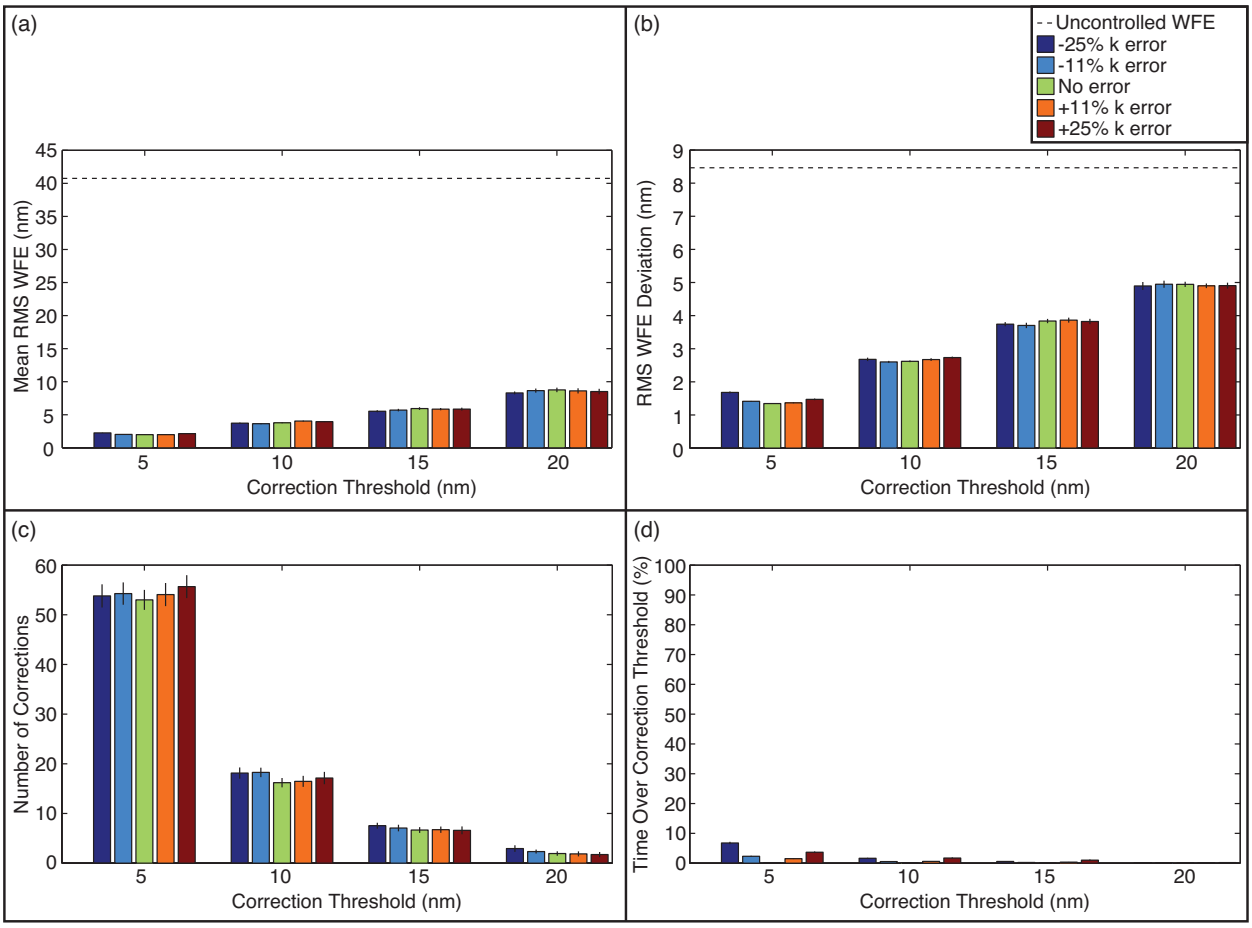

Figure 3.12: Sensitivity to model error. Our implementation of the predictive controller can tolerate significant errors in the modeled thermal decay constant k while still providing superior wavefront control. The k error mostly affects the amount of time that the RMS WFE exceeds the correction threshold τ, and the effects are more pronounced at lower τ since there is less room for the RMS WFE to vary before exceeding τ. For the hypothetical mission scenarios, the predictive controller successfully maintains the wavefront despite k errors as high as 25% (corresponding to a modeled time constant one day shorter than the actual time constant) and as low as -25%, spending less than 7% of the time over τ for τ as low as 5 nm.

3.5 Conclusion

The wavefront control problem for an active space telescope at L2 requires a trade between minimizing the wavefront error and minimizing the number of corrections (actuator moves).

Mirror state updates thus happen occasionally rather than continuously, a key difference from typical ground-based active optics systems. Furthermore, since the dominant wavefront perturbations are due to thermal changes caused by variations in the spacecraft attitude with respect to the sun, they are byproducts of the observing schedule, which is known and determined in advance. We have investigated two approaches for improving the effectiveness of wavefront control under these conditions.

First, these wavefront perturbations can be controlled passively by introducing scheduling constraints that prevent large temperature swings by limiting the allowable sun angles for each observation in the schedule based on the observation duration and the predicted mean telescope temperature at the start of the observation. Such constraints would need to be weighed against the many other criteria used in scheduling, such as the observatory efficiency and momentum management. Given the need to balance the sun angle restrictions with these other factors, it seems implausible that schedule constraints alone could entirely eliminate the need for periodic active corrections; however, there may be some cases worth pursuing as part of a broader strategy. In particular, since the longest observation blocks most readily lead to large swings in the telescope temperature, attention paid to scheduling those observations could result in more benign schedules without imposing any strict restriction in general. In the case of deep fields or large mosaics, it would be advantageous from a wavefront maintenance perspective to split those observations into multiple noncontiguous blocks provided that doing so is consistent with achieving the science goals of those programs.

Alternatively, given any observing schedule it is possible to predict when the wavefront error will exceed some correction threshold and to schedule wavefront corrections in advance. In this case, the control problem is naturally expressed as a hybrid control problem since

the wavefront evolution is affected by discrete events, such as the start of a new observation or the implementation of a new wavefront correction, as well as continuous dynamics, such as the telescope's temperature evolution. Using this approach, we have developed a hybrid predictive controller designed to prevent the time-variable component of the RMS WFE from exceeding a desired correction threshold τ, and compared it to two variants of the baseline control strategy for JWST.

During hypothetical mission scenarios, all three algorithms successfully hold the RMS WFE below τ at least 80% of the time on average, even with wavefront sensor noise levels up to half the correction threshold. The predictive controller generally performs slightly better, holding the RMS WFE below τ at least 91% of the time on average and approaching 100% for sufficiently low sensing noise. It also has superior performance on our metrics for the mean and temporal deviation of the RMS WFE for most test cases. In addition, the predictive controller can be used with more aggressive τ than the other algorithms; limited by their fixed correction period, the baseline and averaging algorithms cannot correct aggressively enough to hold the RMS WFE below τ during times when the wavefront changes rapidly, and the performance flattens out for $\tau < 10$ nm.

The performance of the predictive controller is limited primarily by the allowable number of corrections; the algorithm issues substantially more corrections for lower τ or higher noise levels. Our implementation of the predictive controller can tolerate significant errors in the modeled thermal decay constant k. These errors mostly affect the amount of time that the RMS WFE exceeds the correction threshold, and the effects are more pronounced at lower τ since there is less room for the RMS WFE to vary before exceeding τ. For the sample mission scenarios, the predictive controller successfully maintains the wavefront despite k errors as high as 25% and as low as -25%, with the RMS WFE exceeding a correction threshold of 5

nm less than 7% of the time on average.

Since we used thermal model parameters derived from the requirements for JWST, these quantitative results depend on JWST meeting its design requirements for thermal stability, but more generally they confirm the potential to improve the optical performance of an active space telescope by using more sophisticated control laws. Although the assumed model parameters will differ from the exact numbers in flight, the general behavior and benefits of the predictive controller should hold over a wide range of parameter space for active space telescopes that are perturbed based on predictable external stimuli.

The predictive controller is promising in its current form, but additional enhancements are worth considering in future modeling efforts. For example, using temperature measurements to update the temperature model may allow for less frequent wavefront measurements, increasing the observatory efficiency in addition to improving the overall predictions. Combining predictive control with scheduling restrictions for long observations may reduce the number of corrections needed during a mission. Modifications to the predictive controller, such as adding a control gain or incorporating an estimate of the noise statistics in the model update process, may decrease its sensitivity to noise and help to reduce the number of corrections required to maintain the optical performance. Incorporating additional perturbation sources, such as roll around the telescope optical axis, also remains future work, although it is expected that the current algorithms will naturally compensate for slow perturbations such as gradual sunshield degradation or variations in the orbital distance to the sun.

The practical details of a hypothetical implementation for JWST are beyond the scope of this paper. However, the presence of the wavefront control software system and its associated trending system on the ground at the Science and Operations center rather than on the

spacecraft computer provides more flexibility for future enhancements. Validating thermal and optical models against the as-built performance of the telescope is already planned as part of the ongoing integration and test program. Looking beyond JWST, active optical control is expected to be an essential technology for other future large space telescopes such as the proposed AFTA and ATLAST mission concepts. Active and adaptive control of terrestrial telescopes has matured into a sophisticated field with many specialized algorithms adapted to different conditions. Similarly, we should expect that active telescopes in space will benefit from a variety of control algorithms developed by taking into account the unique circumstances and environment of each mission.

CHAPTER 4

MINIMIZING THE WAVEFRONT ERROR DEGRADATION FOR PRIMARY MIRROR SEGMENTS WITH FAILED HEXAPOD ACTUATORS

4.1 Introduction

One of the defining challenges for engineering space systems is that even simple hardware failures are almost always far beyond our reach for repair, and we must be prepared to work around any failures that do occur. For instance, faced with the failure of one of the wheels on the Mars rover *Spirit*, engineers devised methods for driving backward while dragging the damaged wheel.[88] The *Hayabusa* spacecraft, after suffering serious damage to its propulsion system during its 2005 landing on asteroid Itokawa, nonetheless successfully returned to Earth in 2010 following a complex recovery process and an entirely redesigned return orbital plan.[89] Even the Hubble Space Telescope, one of the few spacecraft designed for on-orbit servicing, benefited from workarounds in between servicing missions, such as the development of a two-gyro pointing mode with attitude control performance comparable to that of the nominal three-gyro mode.[90]

NASA's next flagship observatory, the James Webb Space Telescope (JWST), features a 6.6-meter primary mirror composed of 18 hexagonal segments.[85] JWST will be used to study a variety of topics including galaxy formation, early stellar evolution, and the potential

The material in this chapter was originally published as J. Gersh-Range, E. Elliott, M. Perrin, and R. van der Marel, "Minimizing the Wavefront Error Degradation for Primary Mirror Segments with Failed Hexapod Actuators," *Optical Engineering* **51**(1), 011005 (2012).

for life in other planetary systems. The success of this mission depends upon the ability to maintain the alignment and phasing of the 18 primary mirror segments. Like a segmented ground telescope, JWST relies on actuators to control the position and orientation of each segment, but these actuators cannot be replaced or manually adjusted if failures occur. (Manned servicing is not planned for JWST, unlike Hubble.) As a result, any failures represent a potential threat to the science mission. However, as we show in this paper, the impact of actuator failures can be mitigated by using the remaining segment actuators to optimize the pose of each affected segment. We develop a control scheme that achieves zero performance degradation in the case of one failed actuator per segment, and low wavefront error (WFE) in most cases where multiple actuators fail on a segment.

This paper considers a segmented space telescope with a primary mirror architecture similar to that of JWST.[91] The primary mirror has a circumscribed diameter of 6.6 m, and it is assumed that the mirror is rotationally symmetric about its optical axis, with each segment an off-axis section of the parent conic. The 18 mirror segments are divided into three geometric types,[92] A, B, and C, as shown in Figure 4.1. Each segment is controlled by a hexapod, and it is assumed that an actuator failure results in one of the hexapod legs becoming fixed in length and uncontrollable. Such failures could arise from mechanical issues, such as debris sticking in a gear train, or from a drive electronics malfunction.

We have developed a combined hexapod and optical model and optimization method to minimize the WFE in the event of one or more actuator failures. A hexapod model, described in Section 4.2, relates a set of leg lengths to the segment pose, and a linear optical model converts the pose to a segment WFE. As demonstrated in Section 4.3, the loss of a segment actuator corresponds to the inability to control all six of the segment rigid-body degrees of freedom simultaneously rather than an inability to control a specific degree of freedom. We

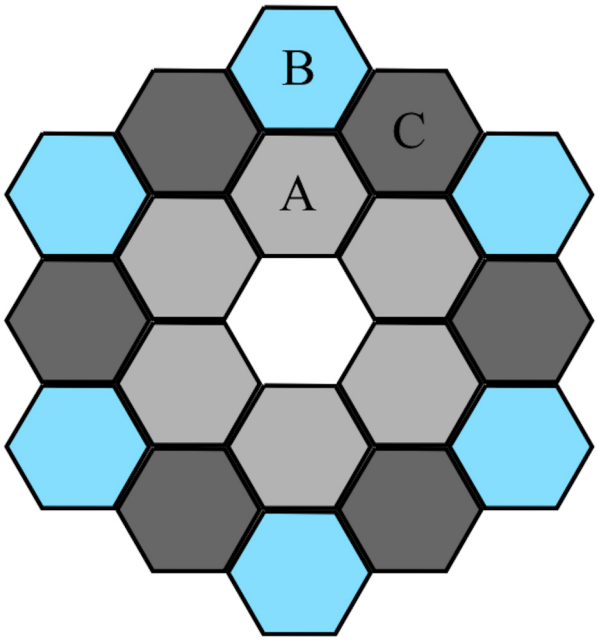

Figure 4.1: The primary mirror segment types.

also show that the uncontrolled degree of freedom can be chosen arbitrarily. Methods for optimizing the pose of a segment with failed actuators and the effects of these failures on the WFE are presented in Sections 4.3 through 4.5. The optimal pose in the event of a single actuator failure is presented in Section 4.3, and general trends in the event of two failures on the same segment are presented in Section 4.4. Finally, in Section 4.5, the risk that actuator failures pose for the successful completion of a mission is assessed. Since the final WFE depends on both the number of failed actuators and the total accumulated length errors for the failed legs, an order-of-magnitude estimate is made for plausible accumulated length errors at the end of a multiyear mission, and Monte Carlo simulations of many actuator failures randomly distributed across the primary are presented. The results show that even with 10% of all the actuators nonfunctional, an acceptable WFE can be achieved in over 98% of cases.

4.2 Telescope and Hexapod Model

Unlike segmented ground telescopes, which use three actuators per segment to control only the tip, tilt, and piston,[9,53,72,93–97] the first segmented space telescope, JWST, uses six actuators to control all of the segment rigid-body degrees of freedom.[85] Rather than controlling these degrees of freedom directly, the actuators are arranged into a hexapod as shown in Figure 4.2, with one actuator adjusting the length of each leg. Since the desired pose (orientation and position) uniquely determines the required length of each leg, all six actuators must work in combination to attain this pose. Actuator failures introduce leg length errors, which prevent the hexapod from achieving this pose exactly, and it is assumed that any failures are hard failures, which fix the length of the affected leg. However, since legs with failed actuators remain free to rotate about their base attachment points, some pose optimization is possible. To examine how well the pose can be optimized in the event of actuator failures, a segmented telescope model has been developed. This model consists of a hexapod model, which relates the leg lengths to the segment pose; a linear optical model, which relates the pose to the segment WFE; and an optimization method that searches for the optimal pose consistent with the failed leg lengths.

A hexapod consists of three main components: a base, a platform, and six legs that can be adjusted in length. The hexapod model contains all of the kinematic equations necessary for describing the orientation and position of the platform relative to the base; with these equations, the hexapod pose can be converted into a set of six leg lengths and vice versa. The kinematics depend upon the hexapod type, which describes how the legs attach to the base and platform, and 3-6 hexapods have been selected for the model since they are similar to the hexapods used on JWST.[85] For 3-6 hexapods, the legs are grouped into three identical

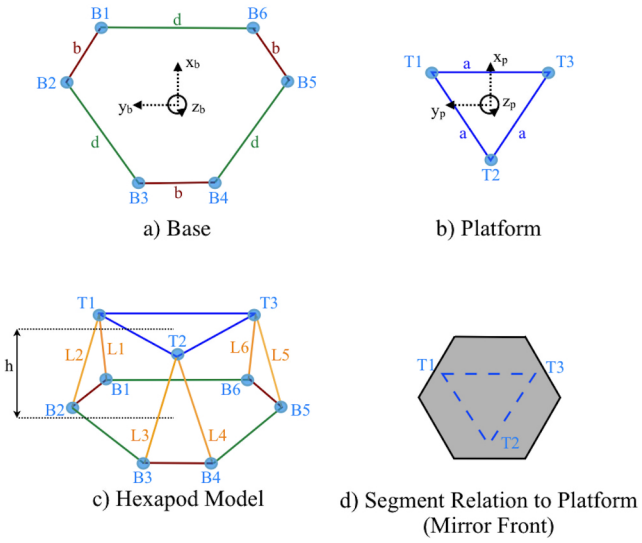

Figure 4.2: The geometry of a 3-6 hexapod. In the 3-6 hexapod model, the legs are paired into three identical bipods, $L1$-$L2$, $L3$-$L4$, and $L5$-$L6$. Four parameters describe the 3-6 hexapod geometry: the distance between the base points of a bipod, b; the distance between adjacent base points of different bipods, d; the lengths of the sides of the platform, a; and the nominal hexapod height, h. (The notation is consistent with that of Liu et al.[102]) It is assumed that the rigid-body motions of the hexapod platform and the mirror segment are identical.

bipods, and each bipod intersects the platform at one point and the base at two points, as shown in Figure 4.2. The six base points form a semi-regular hexagon, with the base points of a bipod separated by a distance b and with adjacent base points of different bipods separated by a distance d [Figure 4.2(a)]. This hexagon defines the plane and position of the base, which is assumed to be immobile since it is attached to the primary mirror backplane. Since the primary mirror is curved globally, each segment's base plane has its own unique orientation. The three platform points form an equilateral triangle with sides of length a, and this triangle defines the position and plane of the platform [Figure 4.2(b)]. Rather than modeling the attachments between the hexapod and the mirror segment explicitly, it is assumed that the rigid-body motions of the hexapod platform and the mirror segment are identical.

To describe the relative orientation and position of the hexapod base and platform, two reference frames and two coordinate systems are defined. One reference frame, B, is attached to the hexapod base, and it contains a coordinate system whose origin is located at the center of the base [Figure 4.2(a)]. The other reference frame, P, is attached to the hexapod platform, and it contains a coordinate system whose origin is located at the center of the platform [Figure 4.2(b)]. The nominal displacement between these coordinate systems is tracked by the vector O, which points from the origin of the base coordinates to the origin of the platform coordinates. For simplicity, it is assumed that in the nominal pose, the base and the platform are parallel and displaced only by a height h.

In this hexapod model, the decenters and tilts are defined in the base reference frame. The decenters measure changes in the location of the center of the hexapod platform, and the tilts track changes in the orientation of the platform frame. The conversion from platform coordinates to base coordinates is

$$ {}^{B}T_i = {}^{B}Q^{P}\,{}^{P}T_i + {}^{B}\Delta, \tag{4.1} $$

where

$$ {}^{B}Q^{P} = \begin{bmatrix} \cos\theta_y \cos\theta_z & -\cos\theta_y \sin\theta_z & \sin\theta_y \\ \cos\theta_x \sin\theta_z + \sin\theta_x \sin\theta_y \cos\theta_z & \cos\theta_x \cos\theta_z - \sin\theta_x \sin\theta_y \sin\theta_z & -\sin\theta_x \cos\theta_y \\ \sin\theta_x \sin\theta_z - \cos\theta_x \sin\theta_y \cos\theta_z & \sin\theta_x \cos\theta_z + \cos\theta_x \sin\theta_y \sin\theta_z & \cos\theta_x \cos\theta_y \end{bmatrix} \tag{4.2} $$

is the rotation matrix from P to B;

$$ {}^{B}\Delta = {}^{B}O + \begin{bmatrix} dx \\ dy \\ dz \end{bmatrix} \tag{4.3} $$

is the total translation; and the variables dx, dy, dz, θ_x, θ_y, and θ_z are the decenters and tilts. For convenience, the superscripts denote the choice of reference frame; ${}^{B}T_i$ is the

ith platform point expressed in base coordinates, and ${}^{P}T_i$ is the same point expressed in platform coordinates. The remaining variables in the hexapod model, the six leg lengths L_i, are simply the distances between the base points B_i and platform points T_i that define each leg:

$$L_i = \left\| {}^{B}T_i - {}^{B}B_i \right\|. \tag{4.4}$$

The pose optimization process consists of three steps: determining the leg lengths required to achieve the desired pose, calculating the lengths of legs with failed actuators, and identifying the optimal pose consistent with the failed lengths. The first step, known as solving the inverse kinematics problem, is trivial since the desired pose uniquely defines the required lengths. The desired location of the platform point for the ith leg, $T_{i,des}$, can be written in base coordinates by substituting the desired pose into Equation (4.1), and the location of the base point for the ith leg, B_i, is known since it is determined by the hexapod geometry. The required leg length, $L_{i,des}$, can be obtained by substituting the locations of these points into Equation (4.4). The second step, determining the lengths of legs with failed actuators, is also trivial. Since it is assumed that any actuator failures are hard failures, the actuator model is binary. If the actuator is working, it is assumed to work perfectly, and the leg length can vary. If the actuator fails, then the leg length is constrained to be a fixed value, which can be parameterized as a length error δ_i between the desired length and the fixed length:

$$L_i = L_{i,des} + \delta_i. \tag{4.5}$$

The final step, identifying the optimal pose consistent with the leg length constraints, is the most complex. Using the results of the previous steps, it is possible to generate a set of randomly perturbed leg lengths that satisfies the constraints imposed by any failed

actuators. However, these lengths must be converted into a set of decenters and tilts since the goal is to find the optimal pose. The conversion from a set of lengths to the pose, known as the forward kinematics problem, is nontrivial since the lengths do not determine the pose uniquely; for a 3-6 hexapod, as many as 16 valid poses exist for the same set of lengths.[98,99] However, unlike many hexapod control problems, which focus on finding the pose for a specific set of six leg lengths, the pose optimization problem is concerned with finding the optimal pose given a set of failed leg lengths; the optimizer evaluates poses based on a given merit function rather than their nearness to a previous or desired pose. As a result, the possibility of multiple solutions for a particular set of leg lengths is not an issue; the optimizer only requires that the forward kinematics solver find one valid pose consistent with the length constraints.

A wide variety of solutions to the forward kinematics problem exist, and these solutions fall into two categories: polynomial methods, which involve solving a 16th degree polynomial in a single variable,[98,100,101] and non-polynomial methods,[102–106] which involve solving a set of nonlinear multivariable equations. In general, the non-polynomial methods are more efficient than the polynomial methods, and the optimization method presented here uses a forward kinematics solver based on the algebraic equations presented by Liu et al.[102]

The pose optimization method outlined in Figure 4.3 avoids solving the forward kinematics problem at every iteration by using the decenters and tilts as the optimization variables instead of the six leg lengths. The method begins with a set of six randomly perturbed leg lengths that satisfies the constraints imposed by any failed actuators. These lengths are converted into a set of decenters and tilts that forms the initial guess for the optimization algorithm; this is the only time the forward kinematics problem is solved. At each iteration, the algorithm verifies that the failed leg length constraints are satisfied by solving the inverse

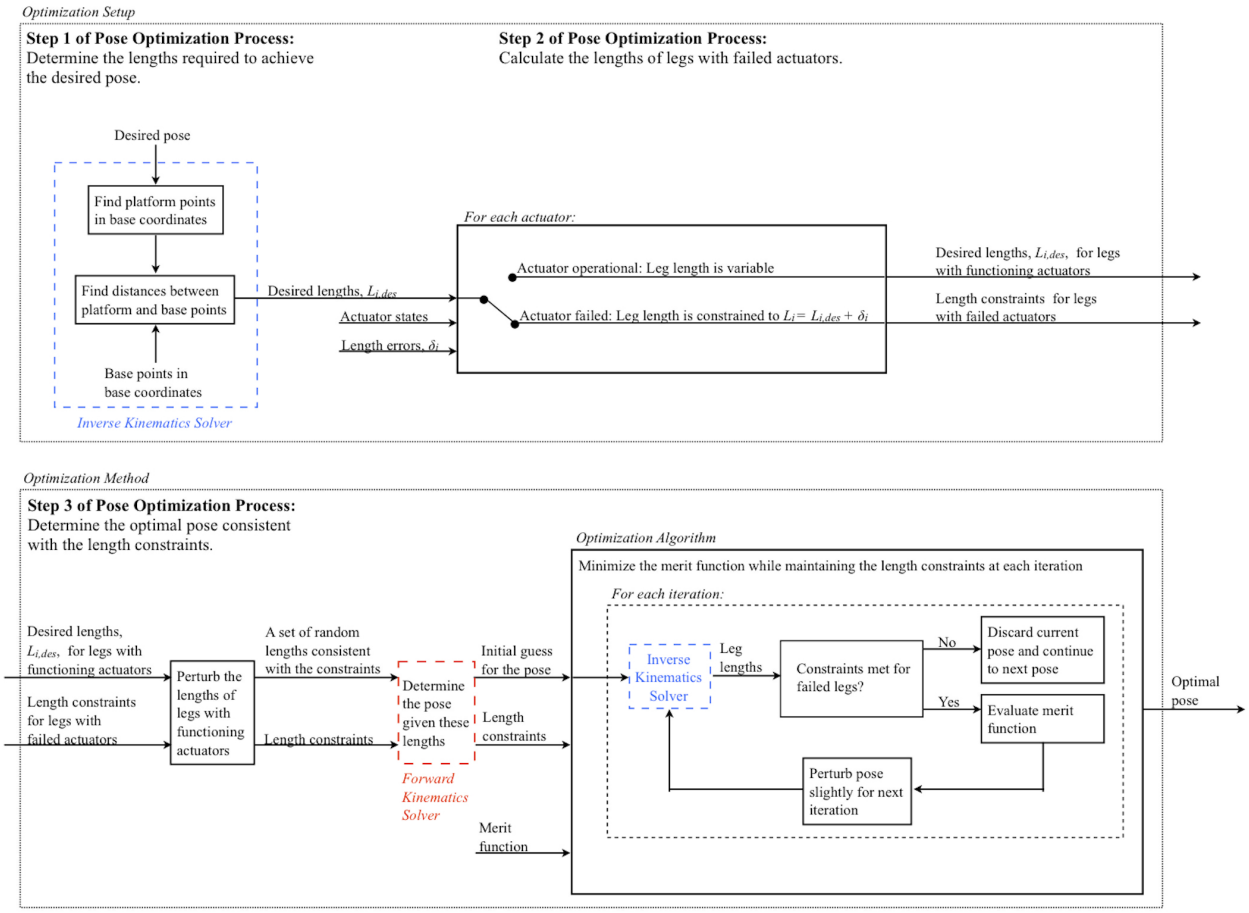

Figure 4.3: The pose optimization process.

kinematics problem and checking the length of each failed leg against its fixed value. The optimization algorithm searches for the pose that minimizes a given merit function, and in order to examine different aspects of the pose optimization problem, two merit functions have been defined.

The first merit function, the diagonal matrix merit function, uses a matrix product to assign weights to the residual tilts and decenters:

$$f_m = v^T M v, \tag{4.6}$$

where $v = \begin{bmatrix} dx_{res} & dy_{res} & dz_{res} & \theta_{x,res} & \theta_{y,res} & \theta_{z,res} \end{bmatrix}$ is a vector containing the residuals and

M is the diagonal weighting matrix. The weights are set to either 10^{10} or 1 depending upon which degrees of freedom are considered important or negligible. (The negligible degrees of freedom are assigned relatively small weights to prevent the optimizer from arbitrarily increasing their residuals in the search for infinitesimally better poses.) As a result, this merit function allows the optimizer to correct only select degrees of freedom.

The second merit function, the root-mean-square wavefront error (RMS WFE) merit function, allows the optimizer to minimize the segment WFE directly:

$$f_m = \left[\frac{\Sigma_{i,j} \left(r_i w^2 \right)}{\Sigma_{i,j} r_i} \right]^{1/2}, \tag{4.7}$$

where w is the WFE evaluated at the point (r_i, θ_j) on the segment. The WFE is calculated using a linear optical model that assumes there is no WFE when the segment is in its nominal pose.[107] When the segment is displaced from its nominal pose, the segment WFE is estimated using a linear combination of Zernike coefficients that capture the low-order WFE terms as a function of the segment's displacement.

In this paper, the hexapod model is used to investigate a specific set of cases. It is assumed that the primary mirror has been phased initially; the model is not intended for use in deployment failure scenarios. It is also assumed that any actuator failures are uncorrelated; single-point failures that affect multiple actuators preferentially are not considered. Finally, actuator range and segment motion limits are not included in the model.

4.3 Single Actuator Failures

In order to understand the effects of actuator failures, it is useful to begin by considering the case of a single failure per segment. For simplicity, it is assumed that the failure occurs on an arbitrary B segment. First, the diagonal matrix merit function is used to show that the leg length error introduced by an actuator failure can be placed into an arbitrary rigid-body degree of freedom. Then, a solution with zero WFE is derived. This solution places all of the error into a degree of freedom corresponding to rotation about the optical axis of the primary mirror.

4.3.1 Diagonal Matrix Merit Optimization

The impact of an actuator failure depends upon both the specific type of hexapod and the relationships between its geometric parameters. To demonstrate the importance of the relationships between the geometric parameters, two 3-6 hexapods with different geometries are considered. For each hexapod, the length of the failed leg is assigned a constant value, and the optimal pose is obtained by minimizing Equation (4.6) with one of the residuals receiving a near-zero weight. This process is repeated for each of the six rigid-body degrees of freedom.

The first hexapod considered is a unit hexapod, a hexapod with a, b, d, and the nominal leg lengths set to one. For this hexapod, the failed leg, $L1$, is assigned a length of 1.01, and the final residuals and leg length changes are shown in Table 4.1. In every case, the optimization algorithm concentrates the leg length error in the uncontrolled rigid-body degree of freedom–

Table 4.1: Diagonal matrix merit optimization results for single failures on a unit hexapod

	Uncontrolled Degree of Freedom					
	x-Decenter	y-Decenter	z-Decenter	x-Tilt	y-Tilt	z-Tilt
Residuals						
x-Decenter	**−0.0172**	$-3.86e^{-8}$	$-1.57e^{-8}$	$2.39e^{-10}$	$-3.71e^{-9}$	$5.70e^{-9}$
y-Decenter	$-3.43e^{-9}$	**−0.1418**	$4.27e^{-9}$	$3.46e^{-9}$	$-7.09e^{-10}$	$-7.07e^{-9}$
z-Decenter	$-2.57e^{-8}$	$2.12e^{-8}$	**0.0122**	$-5.80e^{-9}$	$-1.60e^{-10}$	$-2.30e^{-8}$
x-Tilt (rad)	$-7.72e^{-8}$	$2.59e^{-8}$	$1.06e^{-8}$	**0.0244**	$2.59e^{-9}$	$6.74e^{-9}$
y-Tilt (rad)	$3.76e^{-8}$	$-1.52e^{-8}$	$-6.22e^{-9}$	$2.16e^{-9}$	**−0.0417**	$2.36e^{-9}$
z-Tilt (rad)	$-1.71e^{-7}$	$1.05e^{-8}$	$5.55e^{-9}$	$-1.15e^{-9}$	$-5.04e^{-11}$	**0.0338**
Length Changes						
$L1$-$L1_{des}$ (fixed)	0.01	0.01	0.01	0.01	0.01	0.01
$L2$-$L2_{des}$	−0.0048	0.0779	0.01	0.0101	0.0098	−0.0095
$L3$-$L3_{des}$	−0.0048	0.0779	0.01	0	−0.0194	0.01
$L4$-$L4_{des}$	−0.0048	−0.0628	0.01	0	−0.0194	−0.0095
$L5$-$L5_{des}$	−0.0048	−0.0628	0.01	−0.0099	0.0098	0.01
$L6$-$L6_{des}$	0.01	0.01	0.01	−0.01	0.01	−0.0095

while the loss of a single actuator precludes controlling all six rigid-body degrees of freedom simultaneously, the five remaining actuators allow any five of the degrees of freedom to be controlled. The error in the uncontrolled degree of freedom is on the order of 1% in the majority of the cases, suggesting that while the leg length error can be placed in any degree of freedom, it limits how well that degree of freedom can be controlled. An exception is the case where $L1$ fails and the y-decenter is uncontrolled; in this case, the y-decenter error is on the order of 0.1. However, this result is specific to $L1$ and $L6$, legs whose projections onto the base plane are nominally parallel to the x-axis. For any of the other legs, the y-decenter error is on the order of 0.01.

The other hexapod considered is similar to the hexapods used on JWST[85] in that $d > b$. For this hexapod, the value of a is chosen such that when the platform is projected onto the base plane, each platform point falls on the line connecting the corresponding base points. The failed leg, $L1$, is assigned a length 1 μm longer than its nominal value, and the

Table 4.2: Diagonal matrix merit optimization results for single failures on a hexapod with $d > b$

	Uncontrolled Degree of Freedom					
	x-Decenter	y-Decenter	z-Decenter	x-Tilt	y-Tilt	z-Tilt
Residuals						
x-Decenter (mm)	**−0.0028**	$2.83e^{-11}$	$-3.42e^{-12}$	$-5.98e^{-12}$	$3.48e^{-12}$	$-1.51e^{-12}$
y-Decenter (mm)	$6.17e^{-12}$	**0.0048**	$-8.68e^{-12}$	$-7.61e^{-12}$	$3.29e^{-12}$	$1.44e^{-12}$
z-Decenter (mm)	$-7.22e^{-12}$	$1.39e^{-11}$	**0.0011**	$-1.72e^{-12}$	$2.12e^{-12}$	$2.54e^{-12}$
x-Tilt (rad)	$1.29e^{-8}$	$3.23e^{-8}$	$2.77e^{-9}$	$\mathbf{2.09e^{-4}}$	$-4.09e^{-12}$	$-2.62e^{-12}$
y-Tilt (rad)	$-1.09e^{-8}$	$-1.30e^{-8}$	$1.10e^{-9}$	$3.35e^{-11}$	$\mathbf{-3.62e^{-4}}$	$-6.53e^{-11}$
z-Tilt (rad)	$2.93e^{-9}$	$1.54e^{-8}$	$2.62e^{-10}$	$-7.96e^{-11}$	$-1.10e^{-11}$	$\mathbf{3.98e^{-4}}$
Length Changes (mm)						
$L1$-$L1_{des}$ (fixed)	0.001	0.001	0.001	0.001	0.001	0.001
$L2$-$L2_{des}$	−0.001	−0.001	0.001	0.001	0.001	−0.001
$L3$-$L3_{des}$	0	−0.002	0.001	0	−0.002	0.001
$L4$-$L4_{des}$	0	0.002	0.001	0	−0.002	−0.001
$L5$-$L5_{des}$	−0.001	0.001	0.001	−0.001	0.001	0.001
$L6$-$L6_{des}$	0.001	−0.001	0.001	−0.001	0.001	−0.001

final residuals and leg length changes are shown in Table 4.2. The optimization algorithm again concentrates the length error in the uncontrolled rigid-body degree of freedom, with the magnitude of the leg length error placing a lower bound on the error in this degree of freedom.

For both of the hexapods considered, the final leg length changes always occur in pairs. The pairing of length changes depends upon the hexapod geometry and which degree of freedom is uncontrolled. For the unit hexapod, adjacent legs from different bipods have the same length changes when a decenter is uncontrolled, and in the special case of piston, all of the changes are identical. However, when the x- or y-tilt is uncontrolled, legs on the same bipod have the same length changes, and when clocking is uncontrolled, every other leg has the same length change. Although the way that the length changes are paired depends upon which degree of freedom is uncontrolled, the pairing is always radially symmetric.

For the hexapod with $d > b$, the pairing patterns are identical to those of the unit hexapod except for the cases where the x- or y-decenter is uncontrolled. When the x-decenter is uncontrolled, the pairing is symmetric about the x-axis, as it is for the unit hexapod, but adjacent legs from different hexapods have different lengths. When the y-decenter is uncontrolled, the pattern bears no resemblance to the unit hexapod pairing. In this case, $L1$ and $L5$ have the same length change, and $L2$ and $L6$ have the same length change. The remaining legs, $L3$ and $L4$, are paired, but the length changes are antisymmetric. One explanation for the antisymmetry is that these legs have projections on the base plane that are nominally parallel to the y-axis with opposite signs.

These pairing patterns provide insight into the behavior of the optimizer when the diagonal matrix merit function is used. The paired legs are analogous to a "control unit": in order to achieve the optimal solution, the length changes must be paired in a certain way. A length change for one leg corresponds to either a symmetric or antisymmetric change in another leg. More generally, the pairing patterns describe how the lengths must change in order to move the hexapod in a particular degree of freedom. In the case of the unit hexapod, decenters require that adjacent legs from different bipods have symmetric length changes, and x- and y-tilt require that legs from the same bipod have symmetric length changes. Clocking, on the other hand, requires that adjacent legs have antisymmetric length changes. Similarly, for the hexapod with $d > b$, y-decenter requires that $L1$ and $L5$ have symmetric changes, $L2$ and $L6$ have symmetric changes, and $L3$ and $L4$ have antisymmetric changes.

4.3.2 Zero-WFE Solution

Although an actuator failure introduces a length error that prevents the hexapod from achieving the nominal pose, it does not prevent the hexapod from achieving a pose with zero WFE. Since the primary mirror is assumed to be rotationally symmetric about its optical axis, rotating a segment about the primary mirror center does not affect the WFE. As a result, an infinite number of poses exist for which the segment WFE is zero; these poses correspond to locations on a circle centered about the primary mirror vertex, as shown in Figure 4.4. Even if an actuator fails, the segment can still be positioned somewhere on this circle. This result does not depend on the optical axis being coaligned with the center of the primary; it holds for suitable rotation about the optical axis as long as the parent primary mirror is some conic surface, even an off-axis one. A method for determining the tilts and decenters required to achieve this position is presented below.

The derivation of the zero-WFE solution consists of four main steps. First, expressions for the decenters and tilts required to place the hexapod at an arbitrary location on the zero-WFE circle are derived. These expressions are then used to relate the length of the failed leg to the position along the circle. By comparing this length to the constraint, the position consistent with the length of the failed leg is identified. Finally, this position is back-substituted to obtain the required decenters and tilts.

The first step to identifying the decenters and tilts required to place the hexapod on the zero-WFE circle is to describe the motion in a global coordinate system in the plane of the circle. For an arbitrary B segment, the global coordinate system is chosen to be the base coordinate system rotated about its y-axis by an angle ϕ. The rotation from the global

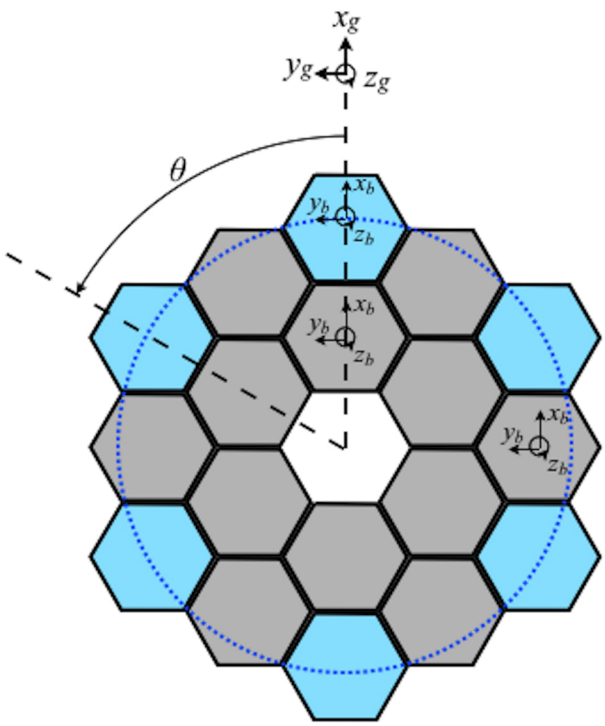

Figure 4.4: The zero-WFE circle. Since the primary mirror is radially symmetric, rotating a segment about the center of the primary mirror does not affect the WFE. For example, an arbitrary B segment can rotate from its position to any location along the dashed circle without changing the wavefront error. In order to describe motion along this circle, two reference frames are defined. The first frame is the hexapod base frame, and the second frame is a global reference frame in the plane of the circle. For convenience, this frame is chosen to be the base frame rotated about its y-axis by an angle ϕ. The base frames for sample A, B, and C segments and the global reference frame for an arbitrary B segment are shown.

reference frame g to the base frame B is described by the matrix

$$ {}^{B}Q^{g} = \begin{bmatrix} \cos\phi & 0 & \sin\phi \\ 0 & 1 & 0 \\ -\sin\phi & 0 & \cos\phi \end{bmatrix}. \tag{4.8} $$

In the global reference frame, the circular motion corresponds to a combination of rotation and x and y translation. To reach a position θ on the circle, the segment rotates by θ and

translates to the location

$$ {}^{g}\begin{bmatrix} dx \\ dy \\ dz \end{bmatrix} = \begin{bmatrix} R(\cos\theta - 1) \\ R\sin\theta \\ 0 \end{bmatrix}, \tag{4.9} $$

where R is the distance (in the plane of the circle) from the center of the segment to the center of the primary mirror. Since the global and base frames are related by ${}^{B}Q^{g}$, the decenters that place the segment on the circle are given by

$$ {}^{B}\begin{bmatrix} dx \\ dy \\ dz \end{bmatrix} = {}^{B}Q^{g} \, {}^{g}\begin{bmatrix} dx \\ dy \\ dz \end{bmatrix} = \begin{bmatrix} R(\cos\theta - 1)\cos\phi \\ R\sin\theta \\ -R(\cos\theta - 1)\sin\phi \end{bmatrix}. \tag{4.10} $$

The tilts are found by comparing two representations of the rotation matrix. Using the axis-angle representation, the matrix that describes rotation about the global z-axis in the B frame can be written as

$$ {}^{B}Q^{P} = \begin{bmatrix} \cos\theta + (1-\cos\theta)\sin^2\phi & -\cos\phi\sin\theta & -(\cos\theta - 1)\sin\phi\cos\phi \\ \cos\phi\sin\theta & \cos\theta & -\sin\phi\sin\theta \\ -(\cos\theta - 1)\sin\phi\cos\phi & \sin\phi\sin\theta & \cos\theta + (1-\cos\theta)\cos^2\phi \end{bmatrix}, \tag{4.11} $$

where

$$ {}^{B}\hat{z}_g = {}^{B}Q^{gg}\hat{z}_g = \begin{bmatrix} \sin\phi \\ 0 \\ \cos\phi \end{bmatrix} \tag{4.12} $$

is the global z-axis expressed in the base coordinates. The same rotation can also be written in terms of the tilts using Equation (4.2). Equating ratios of the elements of the matrices in

Equations (4.2) and (4.11) results in

$$\theta_x = \tan^{-1}\left[\frac{\sin\phi\sin\theta}{\cos\theta + (1-\cos\theta)\cos^2\phi}\right], \tag{4.13}$$

$$\theta_y = \sin^{-1}\left[-(\cos\theta - 1)\sin\phi\cos\phi\right], \tag{4.14}$$

$$\theta_z = \tan^{-1}\left[\frac{\cos\phi\sin\theta}{\cos\theta + (1-\cos\theta)\sin^2\phi}\right]. \tag{4.15}$$

These are the tilts required to maintain the orientation of the segment with respect to the circle. Equations (4.10) and (4.13)-(4.15) are also the expressions for the required tilts and decenters for an A segment since A and B segments have the same orientation. For C segments, the only differences are the expressions for the x- and y- decenters:

$$dx = R\sin\theta \tag{4.16}$$

$$dy = R(1-\cos\theta) \tag{4.17}$$

The leg length error can be related to the position on the circle by combining Equations (4.1), (4.3), (4.4), (4.10), and (4.11):

$$L_i = \left\| {}^{B}T_i - {}^{B}B_i \right\|, \tag{4.18}$$

where

$$\begin{aligned} {}^{B}T_i = &\begin{bmatrix} \cos\theta + (1-\cos\theta)\sin^2\phi & -\cos\phi\sin\theta & -(\cos\theta-1)\sin\phi\cos\phi \\ \cos\phi\sin\theta & \cos\theta & -\sin\phi\sin\theta \\ -(\cos\theta-1)\sin\phi\cos\phi & \sin\phi\sin\theta & \cos\theta + (1-\cos\theta)\cos^2\phi \end{bmatrix} {}^{P}T_i \\ &+ \begin{bmatrix} R(\cos\theta-1)\cos\phi \\ R\sin\theta \\ -R(\cos\theta-1)\sin\phi \end{bmatrix} + {}^{B}O. \end{aligned} \tag{4.19}$$

However, the length of a failed leg is defined as

$$L_i = L_{i,des} + \delta_i. \tag{4.20}$$

Since Equations (4.18) and (4.20) must be satisfied simultaneously, the position on the circle consistent with the fixed length is the value of θ for which

$$f_\theta = \left\| {}^B T_i - {}^B B_i \right\| - (L_{i,des} + \delta_i) = 0. \tag{4.21}$$

Finally, the corresponding decenters and tilts are found by substituting this value of θ into Equations (4.10), (4.13), (4.14), and (4.15). If multiple actuators fail, the segment cannot be placed on the circle of zero WFE unless the length errors all satisfy Equation (4.21) for the same value of θ.

To first order, motion along the circle of zero WFE consists entirely of y-decenter. As a result, in the linear regime, the zero-WFE solution places the majority of the leg length error in the least sensitive degree of freedom, and as the segment moves along the circle, the lengths change according to the pattern in the y-decenter column of Table 4.2. A positive θ corresponds to a positive y-decenter, and the lengths of $L1$, $L4$, and $L5$ increase, while the lengths of $L2$, $L3$, and $L6$ decrease, as shown in Figure 4.5.

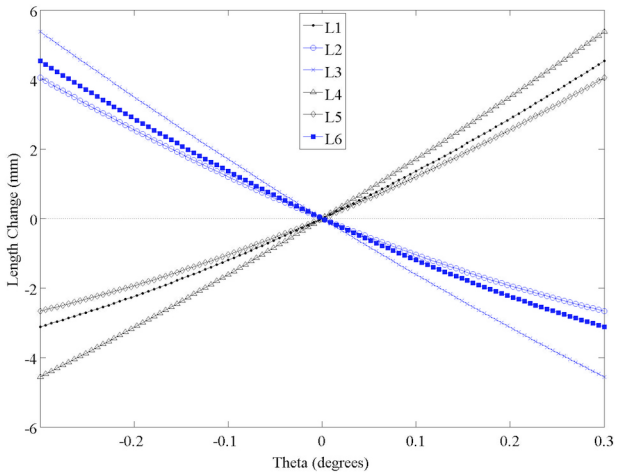

Figure 4.5: Leg length changes for the zero-WFE solution in the linear regime. As the segment moves along the circle of zero WFE, the leg lengths change according to the pattern in the y-decenter column of Table 4.2. The changes for $L1$, $L4$, and $L5$ have one sign, while the changes for $L2$, $L3$, and $L6$ have the other sign. The range of length changes shown here is orders of magnitude larger than the motions expected during wavefront maintenance. Because the solution space smoothly covers such a large range of leg length errors, for any given length of a single failed leg it is possible to find a solution that places the segment on the zero-WFE circle.

4.4 Two Failed Actuators

When two actuators fail on the same segment, the RMS of the optimized residual WFE depends upon which actuators fail and the leg length errors. For an arbitrary B segment, there are 15 total choices for the pair of failed actuators, but since the shape of the mirror surface is symmetric about the x-axis, there are only nine unique pairs. For each failed actuator, the range of possible leg length errors is bounded only by the actuator range and any segment motion limits. In order to understand how the failed pair and the length errors affect the optimized RMS WFE, a series of optimizations have been performed for each of the nine unique actuator pairs. In each case, the individual length errors varied from -25 μm to $+25$ μm, for a total of 625 scenarios per pair. This range was chosen to encompass much more motion than is expected to be needed for week-to-week wavefront control. The resulting optimized WFEs are presented in a series of contour plots in Figure 4.6, with the height of each contour representing the optimized RMS WFE in nanometers.

For each pair of failed actuators, much lower WFEs occur for either symmetric failures, in which both length errors have the same sign, or antisymmetric failures, in which the length errors have opposite signs. This preference can be explained by the pattern of length changes in Table 4.2. As demonstrated in Section 4.3, the leg length error introduced by a failed actuator can be placed in an arbitrary rigid-body degree of freedom, corresponding to a specific pattern of length changes. In the zero-WFE solution, the segment moves along a circle, and the majority of the error is placed in the least sensitive degree of freedom, y-decenter. Similarly, when two actuators fail, the error can be placed in two rigid-body degrees of freedom that share the same pattern for the failed legs. The smallest RMS WFE results when the error can be placed in y-decenter and either x-decenter or clocking; this

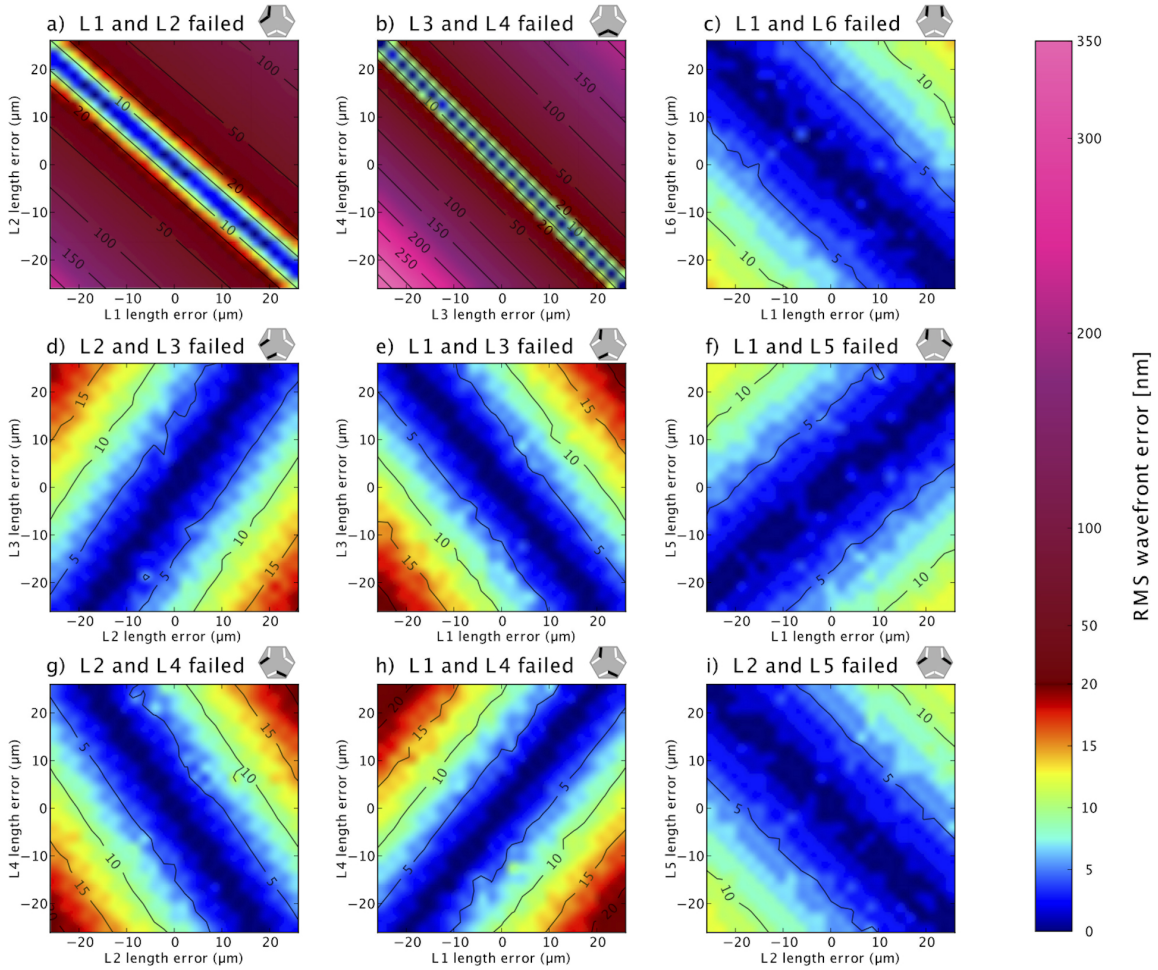

Figure 4.6: The optimized RMS WFE for pairs of failed actuators. For an arbitrary B segment, there are nine unique pairs of failed actuators. The worst pairs, (a) and (b), are cases where both legs fail on the same bipod. Pairs (c) and (d) are cases where adjacent legs of different bipods fail, and pairs (e), (f), and (g) are cases where two left or two right legs fail. Finally, pairs (h) and (i) are cases where diagonally opposite legs fail. In the contour plots, the x- and y-axes correspond to the leg length errors, and the height of the contours represents the optimized RMS WFE in nm. The leg numbering scheme is shown in Figure 4.2.

solution is similar to the zero-WFE solution, although the segment cannot be placed along the zero-WFE circle unless the length errors satisfy Equation (4.21) for the same value of θ. As a result, the length change pattern for y-decenter determines whether symmetric or antisymmetric failures are preferred.

By far, the worst failure cases are the cases in which two actuators on the same bipod fail symmetrically. These cases are an order of magnitude worse than the failure cases for any other actuator pair because they are the only cases in which the length errors correspond to the pattern for the three most sensitive degrees of freedom. When both actuators on a bipod fail, the corresponding platform point is constrained to move along a circle whose radius is perpendicular to the line connecting the two base points. As a result, motions of this platform point consist of piston, translation along a specific line in the xy-plane, and tilt about an axis perpendicular to this line. The segment is also free to pivot about this platform point. In the very worst case, symmetric failures of $L3$ and $L4$, motions of the platform point consist of piston, x-decenter, and y-tilt. While it is possible to concentrate the majority of the error into the x-decenter, the required motion is sufficiently large to affect the WFE. Since symmetric failures for actuators on the same bipod are an order of magnitude more damaging than comparable failures for any other actuator pair, a segmented space telescope would benefit from a design in which single-point failures affect legs on different bipods rather than legs on the same bipod.

4.5 A Segmented Telescope with Randomly Distributed Failures

Finally, we seek to understand how likely it is that multiple actuator failures will prevent a mission from achieving its scientific goals. Evaluating this requires both a hypothetical number of failed actuators and an estimate for the leg length errors. Let us assume the mirror is properly phased immediately after launch at time t_0, but N actuators fail immediately thereafter. Over time, the mirror will evolve away from the phased state and will require correction; the difference between the uncorrected mirror state at some time t_1 and its state at t_0 gives the total leg motions required, and hence the length errors for the failed legs.

The long-term evolution of a space telescope's optomechanical structure is a complex subject and beyond the scope of this paper. We thus consider two simple cases based on a notional change of 60 nm RMS per two weeks, loosely based on the JWST mission's expectation of <50 nm RMS drift per two week period.[85] Assuming that changes across many periods add in a random walk, after n periods the total change in wavefront grows as $\sqrt{n}$. For $t_1 - t_0 = 5$ years, this yields a total of 630 nm RMS. If we instead assume that the changes add linearly each period, then we arrive at 7200 nm RMS over five years. We emphasize that these are notional values only, not based on any detailed thermal or optomechanical modeling. While these two estimates are not particularly well-motivated physically, they do provide test cases spanning more than an order of magnitude in total WFE. We proceed with this conservative method and show that even given assumptions of very large drift and many failed actuators, it is often possible to achieve a well-corrected mirror.

For each of the two test cases, a set of segment motions that yield the desired total

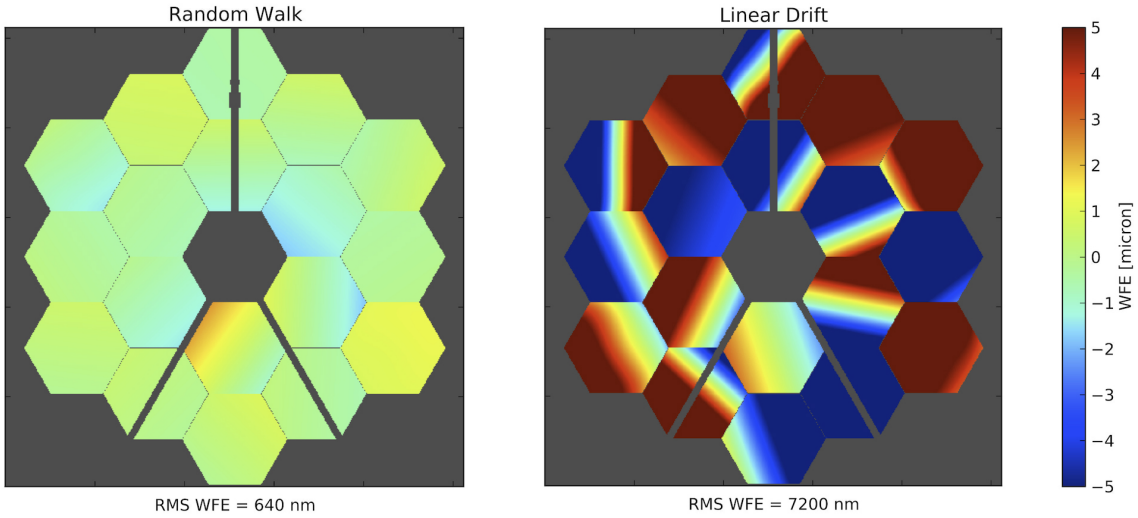

Figure 4.7: The primary mirror starting states. The primary mirror starting states assume that N actuators fail immediately after the primary mirror is phased. Over time, the mirror evolves away from its phased state, and the changes are assumed to grow either linearly (right) or as the square root of the number of two-week periods that pass (left).

delta WFE is generated. In effect, these datasets give the net motion each segment might hypothetically drift over a mission's lifetime. These starting states are shown in Figure 4.7. The problem of evaluating wavefront control at the end of the mission is then equivalent to asking how well we can flatten a mirror starting in one of these states, given some number of failed actuators.

For each starting state, 10 or 30 actuators (out of the total 108 actuators on the primary) randomly fail, and for each segment with at least one failed actuator, the nonlinear optimizer searches for the pose that minimizes the segment RMS WFE. No global optimizations are performed; that is to say, each segment is optimized independently, and overall motions of the primary mirror as a whole and adjustments to the secondary mirror are not considered. After all 18 segment poses are optimized, the RMS WFE for the entire primary mirror is calculated. Histograms of the primary mirror WFE after 300 trials are shown in Figure 4.8.

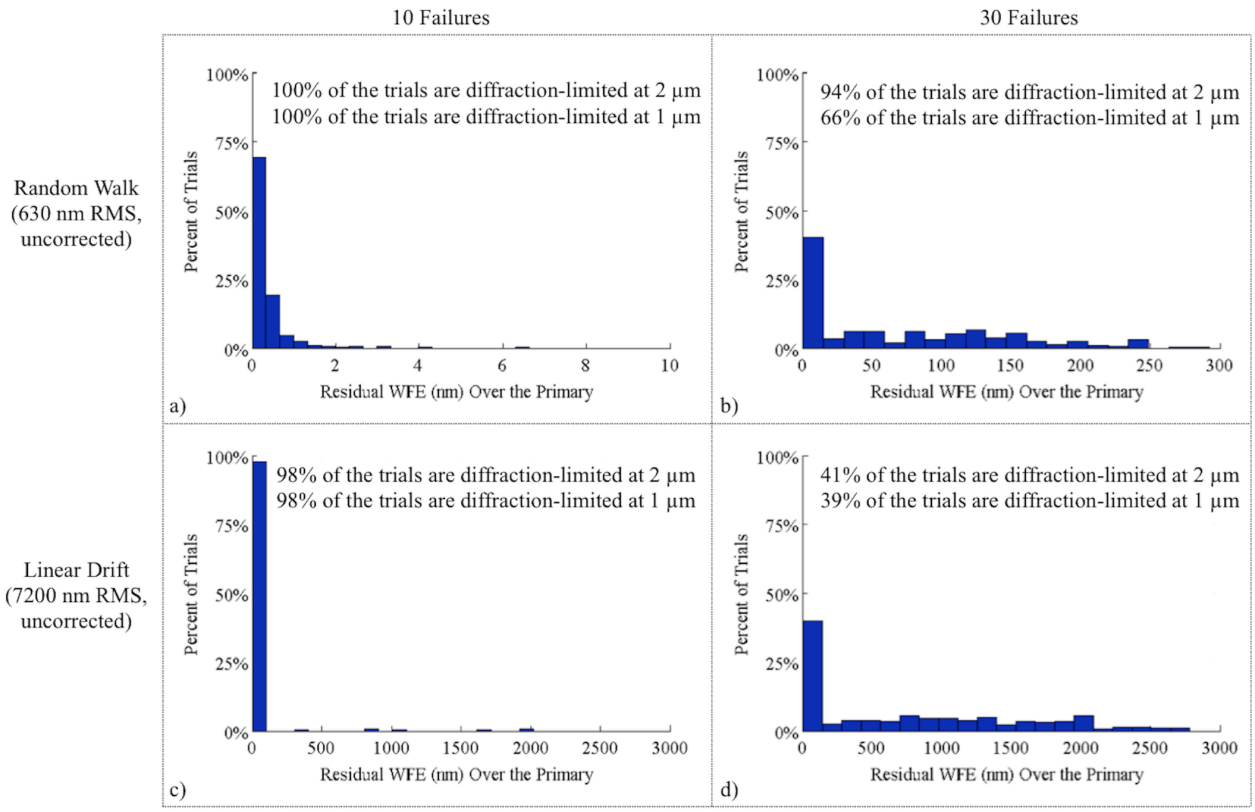

Figure 4.8: The optimized RMS WFE for randomly distributed failures.

The percentages of trials for which the primary mirror is diffraction-limited at wavelengths of 1 and 2 μm (100 and 200 nm of RMS WFE, respectively) are also shown.

Of the four scenarios, the linear drift case with 30 failures is the most pessimistic [Figure 4.8(d)]. In this case, 41% of the trials are diffraction-limited at a wavelength of 2 μm and 39% are diffraction-limited at a wavelength of 1 μm, even though nearly a third of the actuators failed and the total WFE correction needed was over 7000 nm RMS. When only 10 actuators fail, the percentage of trials diffraction-limited at 1 μm increases to 98% [Figure 4.8(c)]. In the most optimistic scenario, the random walk case with 10 failures, 100% of the trials are diffraction-limited at 1 μm, as shown in Figure 4.8(a). When the number of failures increases to 30, 94% of the trials are diffraction-limited at 2 μm and 66% are diffraction-limited at 1

μm, as shown in Figure 4.8(b).

The results of the Monte Carlo simulations are due in part to the expected distribution of actuator failures. When only 10 actuators fail, the RMS WFE distribution decays exponentially in both the random walk and linear drift cases since in the majority of the trials the segments have no more than one failed actuator and therefore do not contribute to the total WFE. In some trials, there are segments with two failed actuators, but as shown in Section 4.4, their contributions to the WFE are small. In the rare trials that contain segments with three or more failures, the contributions from these segments are reduced by a factor of $(1/18)^{1/2}$. In the worst trial in Figure 4.8(a), one segment had two failed bipods, and in the worst trial in Figure 4.8(c), one segment had five failed actuators. When 30 actuators fail, the RMS WFE distribution is bimodal; there is a sharp peak near zero followed by a roughly Gaussian distribution. The peak near zero is due to the fact that in many of the trials, the majority of the segments have at most two failed actuators, so their contributions to the total WFE are low. However, there is also a distribution of cases where several of the segments have at least three failures, leading to larger WFE contributions. In the worst trial in Figure 4.8(b), two segments had three failed actuators, one segment had four failed actuators, and one segment had five failed actuators. In the worst trial in Figure 4.8(d), two segments had four failed actuators.

These results show that a mission can tolerate as many as 10 failed actuators with essentially no degradation in optical performance, assuming that there are no actuator range or segment motion limits that interfere with the pose optimization. There is some risk of lost performance if nearly one-third of the actuators fail, but this is an extremely pessimistic case. Even in this scenario, there are still many actuator failure combinations for which good performance is achievable. Segmented mirrors controlled by 3-6 hexapods prove to be very

robust, and they degrade gracefully even in the case of substantial breakage.

4.6 Summary

While multiple segment actuator failures represent a potential threat to the science mission of a segmented space telescope, the effects of these failures can be mitigated by using the remaining actuators to optimize the pose of each affected segment. As shown in Section 4.3, the loss of a segment actuator corresponds to an inability to control all six rigid-body degrees of freedom simultaneously rather than an inability to control a particular degree of freedom. Furthermore, the uncontrolled degree of freedom can be chosen arbitrarily. Placing the error in a particular degree of freedom requires the leg lengths to change in a specific pattern, and these patterns provide insight into the ability to optimize the RMS WFE.

When only one actuator fails on a segment, there exists an optimal pose with no WFE; the leg length error can be related to a position on the zero-WFE circle. In this case, the majority of the length error is placed in the least sensitive rigid-body degree of freedom, y-decenter, and the length changes follow the y-decenter pattern. Similarly, when two actuators fail, the error can be placed in two rigid-body degrees of freedom that share the same pattern as the length errors. The smallest RMS WFE results when the length errors follow the y-decenter pattern; in this case, the error can be placed in a combination of the least sensitive degrees of freedom. The worst failures are when both actuators on a bipod fail symmetrically. These cases are an order of magnitude worse than the failure cases for any other actuator pair, and symmetric failures of the $L3$-$L4$ bipod are the worst since this bipod is symmetric about the x-axis. However, even in this case, the segment WFE is below 350 nm for length errors as

large as 25 μm, so the contribution to the total WFE is no more than 82 nm.

In the most pessimistic failure scenario considered, 30 randomly distributed actuators failed over a primary mirror that linearly drifted for five years. In this case, 41% of the trials were diffraction-limited at a wavelength of 2 μm, and 39% were diffraction-limited at a wavelength of 1 μm, even though nearly a third of the actuators failed. When the number of failures decreased to 10, 98% of the trials were diffraction-limited at a wavelength of 1 μm. These results suggest that a large number of actuator failures must occur in order to degrade the RMS WFE significantly.

The results of all these simulations show that segmented mirrors controlled by 3-6 hexapods are very robust and degrade gracefully even in the case of substantial breakage, assuming that the pose optimization process is not limited or precluded by actuator range limits, segment motion limits, or the control software handling of failed actuators. Future simulations will investigate the impact of actuator range and segment motion limits on the pose optimization process. Global optimization techniques, which consider overall motions of the primary mirror as a whole and adjustments to the secondary mirror, will also be explored.

REFERENCES

[1] P. A. Lightsey, C. Atkinson, M. Clampin, and L. D. Feinberg, "James Webb Space Telescope: large deployable cryogenic telescope in space," *Optical Engineering* **51**(1), 011003-1 – 011003-19 (2012).

[2] Arianespace, Ariane 5 User's Manual: Issue 5 Revision 1 (2011).

[3] M. Postman et al., "Advanced Technology Large-Aperture Space Telescope: science drivers and technology developments," *Optical Engineering* **51**(1), 011007-1 – 011007-11 (2012).

[4] D. Lester et al., "Science promise and conceptual mission design for SAFIR: the single aperture far-infrared observatory," *Proc SPIE* **6265**, 62651X–1 – 62651X–15 (2006).

[5] H. P. Stahl et al., "Optical manufacturing and testing requirements identified by the NASA Science Instruments, Observatories, and Sensor Systems Technology Assessment," *Proc SPIE* **8126**, 812603-1 – 812603-12 (2011).

[6] P. R. Lawson et al., "Terrestrial Planet Finder Interferometer (TPF-I) Whitepaper for the AAAC Exoplanet Task Force" (2007).

[7] E. M. C. Kong et al., "Electromagnetic formation flight for multisatellite arrays," *Journal of spacecraft and rockets* **41**(4), 659–666 (2004).

[8] L. Young, "Vibrations from power supply mean more trouble for Hubble," *Baltimore Sun* (November 7, 1990).

[9] P. Y. Bely, Ed., *The Design and Construction of Large Optical Telescopes*, New York: Springer-Verlag New York (2003).

[10] P. Y. Bely, O. L. Lupie, and J. L. Hershey, "The line-of-sight jitter of the Hubble Space Telescope," *Proc. SPIE* **1945**, 55–61 (1993).

[11] A. Danjon and A. Couder, *Lunettes et télescopes : Théorie, conditions d'emploi, description, réglage, histoire*, Paris: Editions de la Revue d'Optique Theorique et Instrumentale, 570 (1935).

[12] L. Cohan and D. W. Miller, "Launch Load Alleviation for Lightweight, Active Mirrors," 2010 AIAA SDM Student Symposium (2010).

[13] J. A. Gersh-Range, W. R. Arnold, M. A. Peck, and H, P. Stahl, "A flux-pinning mechanism for segment assembly and alignment," *Proc SPIE* **8150**, 815005-1 – 815005-7, (2011).

[14] W. R. Arnold, Sr., On Mirror Manufacturing Capabilities.

[15] ANSYS, ANSYS, Inc. Documentation for Release 12.0, Canonsburg, PA: ANSYS (2009).

[16] D. Leisawitz, "NASA's far-IR/submillimeter roadmap missions: SAFIR and SPECS," *Advances in Space Research* **34**(3), 631–636 (2004).

[17] H. A. Thronson, M. Postman, H. P. Stahl, and W. A. Traub, "Astronomy Enabled by Ares V Heavy Lift," Future In-Space Operations White Paper (2007).

[18] D. J. Benford et al., "Mission Concept for the Single Aperture Far-Infrared (SAFIR) Observatory," *Astrophysics and Space Science* **294**, 177–212 (2004).

[19] G. H. Rieke et al., "Charting the Winds that Change the Universe, II. The Single Aperture Far Infrared Observatory (SAFIR)," *Proceedings of the Second Workshop on New Concepts for Far-Infrared and Submillimeter Space Astronomy*, 157–166 (2002).

[20] J. C. Mather, "Prospects for Future Observations in the Mid/Far IR," *AIP Conf. Proc.* **666**, 347–354 (2003).

[21] G. L. Pilbratt, "Herschel Mission Overview and Key Programmes," *Proc. SPIE* **7010**, 701002-1–701002-12 (2008).

[22] L. Feinberg et al., "Space telescope design considerations," *Optical Engineering* **51**(1), 011006-1–011006-9 (2012).

[23] M. Levine and C. White, "Material Damping Experiments at Cryogenic Temperatures," *Proc. SPIE* **5179**, 165-176 (2003).

[24] O. Romberg, M. Tausche, C. Pereira, and L. Panning, "Passive Damping of Spacecraft Sandwich Panels," 10th European Conference on Spacecraft Structures, Materials, & Mechanical Testing, 1–8 (2007).

[25] H. P. Stahl and L. Feinberg, "Summary of NASA advanced telescope and observatory capability roadmap," *Aerospace Conference, 2007 IEEE*, 1–11 (2007).

[26] J. Gersh-Range, W. R. Arnold, Sr., and H. P. Stahl, "Edgewise Connectivity: An Approach to Improving Segmented Primary Mirror Performance," (2014).

[27] Can Superconductors, "Superconducting YBCO Levitation Disks," Can Superconductors, http://shop.can-superconductors.com/attachment.php?id_attachment=2 [accessed March 29, 2012].

[28] A. Kordyuk, "Magnetic levitation for hard superconductors," *Journal of Applied Physics* **83**(1), 610–612 (1998).

[29] J. P. Shoer and M. A. Peck, "Flux-Pinned Interfaces for the Assembly, Manipulation, and Reconfiguration of Modular Space Systems," *The Journal of the Astronautical Sciences* **57**(3), 667–688 (2009).

[30] L. C. Davis, "Lateral restoring force on a magnet levitated above a superconductor," *Journal of Applied Physics* **67**(5), 2631–2636 (1990).

[31] R. Williams and J. R. Matey, "Equilibrium of a magnet floating above a superconducting disk," *Applied Physics Letters* **52**(9), 751–753 (1988).

[32] J. R. Hull and A. Cansiz, "Vertical and lateral forces between a permanent magnet and a high-temperature superconductor," *Journal of Applied Physics* **86**(11), 6396–6404 (1999).

[33] S. A. Basinger, J. R. Hull, and T. M. Mulcahy, "Amplitude dependence of magnetic stiffness in bulk high-temperature superconductors," *Applied Physics Letters* **57**(27), 2942–2944 (1990).

[34] J. Shoer et al., "Microgravity Demonstrations of Flux Pinning for Station-Keeping and Reconfiguration of CubeSat-Sized Spacecraft," *Journal of Spacecraft and Rockets* **47**(6), 1066–1070 (2010).

[35] J. Shoer and M. Peck, "Reconfigurable Spacecraft as Kinematic Mechanisms Based on Flux-Pinning Interactions," *Journal of Spacecraft and Rockets* **46**(2), 466–469 (2009).

[36] H. P. Stahl, M. Postman, and W. S. Smith, "Engineering specification for large-aperture UVO space telescopes derived from science requirements," *Proc. SPIE* **8860**, 886006-1–886006-13 (2013).

[37] R. Nalbandian and A. E. Hatheway, "Extra Large Telescope Actuator (ELTA)," *Proc. SPIE* **4837**, 814–820 (2003).

[38] R. M. Warden, "Cryogenic Nano-Actuator for JWST," Proceedings of the 38th Aerospace Mechanisms Symposium, 239–252 (2006).

[39] L. Zago, P. Schwab, and D. Gallieni, "Development and testing of a high-precision, high-stiffness linear actuator for the focus-center mechanism of the SOFIA secondary mirror," *Proc. SPIE* **4014**, 392–398 (2000).

[40] SCHOTT North America, "Zerodur: Zero Expansion Glass Ceramic," SCHOTT North America, http://www.us.schott.com/advanced_optics/english/download/schott_zerodur_katalog_july_2011_us.pdf [accessed October 10, 2013].

[41] SCHOTT, "TIE-37: Thermal expansion of Zerodur" (2006).

[42] J. H. Burge, T. Peper, and S. F. Jacobs, "Thermal expansion of borosilicate glass, Zerodur, Zerodur M, and unceramized Zerodur at low temperatures," *Applied Optics* **38**, 7161–7162 (1999).

[43] P. Z. Chang, F. C. Moon, J. R. Hull, and T. M. Mulcahy, "Levitation force and magnetic stiffness in bulk high-temperature superconductors," *Journal of Applied Physics* **67**(9), 4358–4360.

[44] B. R. Weinberger, L. Lynds, and J. R. Hull, "Magnetic bearings using high-temperature superconductors: some practical considerations," *Superconductor Science and Technology*, **3**(7), 381–388 (1990).

[45] Correlated Magnetics, "SwirlCode^{TM}correlated pair," Correlated Magnetics, http://www.correlatedmagnetics.com/products/swirlcodetm-correlated-pair/ [accessed September 14, 2013].

[46] Correlated Magnetics, "Programmed Behavior," Correlated Magnetics, http://www.correlatedmagnetics.com/technology/maglatch/ [accessed September 14, 2013].

[47] Correlated Magnetics, "Correlated Magnetics" (2009).

[48] J. N. Juang and R. S. Pappa, "An eigensystem realization algorithm for modal parameter identification and model reduction," *Journal of guidance, control, and dynamics* **8**(5), 620–627 (1985).

[49] J. Shoer and M. Peck, "Stiffness Of A Flux-Pinned Virtual Structure For Modular Spacecraft," *Journal of the British Interplanetary Society*, **62**, 57–65 (2009).

[50] Correlated Magnetics, "Coded Magnetic Structures and the Shortest Path Effect" (2009).

[51] R. N. Wilson, F. Franza, and L. Noethe, "Active optics," *Journal of Modern Optics* **34**(4),485–509 (1987).

[52] R. N. Wilson and L. Noethe, "Closed-loop active optics: its advantages and limitations for correction of wind-buffet deformations of large flexible mirrors," *Proc. SPIE* **1114**, 290–301 (1989).

[53] R. C. Jared et al., "The W. M. Keck Telescope segmented primary mirror active control system," *Proc. SPIE* **1236**, 996–1008 (1990).

[54] S. Guisard, L. Noethe, and J. Spyromilio, "Performance of active optics at the VLT," *Proc. SPIE* **4003**, 154–164 (2000).

[55] A. R. Contos et al., "Aligning and maintaining the optics for the James Webb Space Telescope (JWST) on-orbit: the wavefront sensing and control concept of operations," *Proc. SPIE* **6265**, 62650X–1–62650X–16 (2006).

[56] D. S. Acton et al., "Wavefront sensing and controls for the James Webb Space Telescope," *Proc. SPIE* **8442**, 84422H–1–84422H–11 (2012).

[57] J. Gersh-Range, E. Elliott, M. Perrin, and R. van der Marel, "Minimizing the wavefront error degradation for primary mirror segments with failed hexapod actuators," *Optical Engineering* **51**(1), 011005–1–011005–12 (2012).

[58] D. Spergel et al., "Wide-Field InfraRed Survey Telescope-Astrophysics Focused Telescope Assets WFIRST-AFTA Final Report," *ArXiv e-prints* arXiv:1305.5422 [astro-ph.IM] (2013).

[59] M. Postman et al., "Advanced Technology Large-Aperture Space Telescope (ATLAST): A technology roadmap for the next decade," *ArXiv e-prints* arXiv:0904.0941 [astro-ph.IM] (2009).

[60] J. S. Knight, P. Lightsey, A. Barto, "Predicted JWST imaging performance", *Proc. SPIE*, **8442**, 84422G (2012).

[61] D. Di Nino et al., "HST Focus Variations with Temperature," Instrument Science Report ACS 2008-03 (2008).

[62] C. Perrygo et al., "Passive thermal control of the NGST," *Proc. SPIE* **3356**1102–1113 (1998).

[63] M. Werner, "The Spitzer Space Telescope," *Optical Engineering* **51**(1) 011008–1–011008–7 (2012).

[64] J. D. Johnston et al., "Integrated modeling activities for the James Webb Space Telescope: structural-thermal-optical analysis," *Proc. SPIE* **5487**, 600-610 (2004).

[65] W. M. Kinzel and R. E. Douglas, Jr., "JWST observation specification and expansion to support planning and scheduling," *Proc. SPIE* **8448**84480Z–1–84480Z–14 (2012).

[66] C. Ikpe, C. Congedo, C. Holmes, and M. McGinnis, "JWST observatory synchronized thermal study #1 (STS-1) Summary."

[67] L. Petro et al., "Planning to minimize angular momentum," STScI Technical Report JWST-STScI-000755, SM-12 (2005).

[68] K. D. Gordon et al., "Optimizing the observing efficiency of the James Webb Space Telescope," *Proc. SPIE* **8448**, 84481U–1–84481U–11 (2012).

[69] R. N. Wilson, F. Franza, L. Noethe, and G. Andreoni, "Active optics," *Journal of Modern Optics* **38**(2), 219–243 (1991).

[70] J. Llacer, R. C. Jared, and J. M. Fuertes, "Analysis of the W. M. Keck telescope primary mirror control loop," *Proc. SPIE* **1236**, 1024–1037 (1990).

[71] J. Rakoczy et al., "Primary mirror figure maintenance of the Hobby-Eberly Telescope using the Segment Alignment Maintenance System," *Proc. SPIE* **4837**, 702–713 (2003).

[72] P. M. Thompson, D. G. MacMynowski, and M. J. Sirota, "Control analysis of the TMT primary segment assembly," *Proc SPIE* **7012**, 70121N–1–70121N–14 (2008).

[73] P. J. Antsaklis, "A brief introduction to the theory and applications of hybrid systems," *Proc. IEEE* **88**(7), 879–887 (2000).

[74] M. D. Lemmon, K. X. He, and I. Markovsky, "Supervisory hybrid systems," *IEEE Control Systems* **19**(4), 42–55 (1999).

[75] R. Alur and D. L. Dill, "A theory of timed automata," *Theoretical Computer Science* **126**(2), 183–235 (1994).

[76] R. Alur, C. Courcoubetis, T. A. Henzinger, and P.-H. Ho, "Hybrid automata: an algorithmic approach to the specification and verification of hybrid systems," in *Hybrid systems*,

ed. R. L. Grossman, A. Nerode, A. P. Ravn, and H. Rischel, Springer-Verlag, 209-229 (1993).

[77] F. D. Torrisi and A. Bemporad, "HYSDEL–a tool for generating computational hybrid models for analysis and synthesis problems," *IEEE Transactions on Control Systems Technology* **12**(2), 235–249 (2004).

[78] A. Bemporad and M. Morari, "Control of systems integrating logic, dynamics, and constraints," *Automatica* **35**, 407–427 (1999).

[79] D. L. Pepyne and C. G. Cassandras, "Optimal control of hybrid systems in manufacturing," *Proc. IEEE* **88**(7), 1108–1123 (2000).

[80] C. Livadas, J. Lygeros, and N. A. Lynch, "High-level modeling and analysis of the traffic alert and collision avoidance system (TCAS)," *Proc.IEEE* **88**(7), 926–948 (2000).

[81] R. Horowitz and P. Varaiya, "Control design of an automated highway system," *Proc. IEEE* **88**(7), 913–925 (2000).

[82] A. Balluchi et al., "Automotive Engine Control and Hybrid Systems: Challenges and Opportunities," *Proc. IEEE* **88**(7), 888–912 (2000).

[83] D. Subramanian et al., "Control design for a hybrid dynamic system: A NASA life support system," in *Hybrid systems: computation and control*, ed. R. Alur and G. J. Pappas, Springer-Verlag, 570-584 (2004).

[84] B. Kerkez, S. D. Glaser, J. A. Dracup, and R. C. Bales, "A hybrid system model of seasonal snowpack water balance," *Proceedings of the 13th ACM International Conference on Hybrid Systems: Computation and Control*, 171–180 (2010).

[85] J. P. Gardner et al., "The James Webb Space Telescope," *Space Sci. Rev.* **123**(4), 485-606 (2006).

[86] P. J. Campo and M. Morari, "Robust model predictive control," *American Control Conference, 1987*, 1021–1026 (1987).

[87] P. A. Lightsey, A. A. Barto, and J. Contreras, "Optical performance for the James Webb Space Telescope," *Proc. SPIE* **5487**, 825–832 (2004).

[88] P. C. Leger et al., "Mars Exploration Rover surface operations: driving Spirit at Gusev Crater," in *Proc. 2005 IEEE Conf. Syst. Man. and Cybern.* **2**, 1815-1822 (2005).

[89] H. Kuninaka and J. Kawaguchi, "Lessons learned from round trip of HAYABUSA asteroid explorer in deep space," in *Proc. 2011 IEEE Aerospace Conf.*, 1-8 (2011).

[90] K. Sembach et al., "HST two-gyro mode," in *The 2005 HST Calibration Workshop: Hubble after the Transition to Two-gyro Mode*, A. M. Koekemoer, P. Goudfrooij, and L. L. Dressel, Eds., pp. 375-383, National Aeronautics and Space Administration, Goddard Space Flight Center, Greenbelt, MD (2005).

[91] J. Contreras and P. Lightsey, "Optical design and analysis of the James Webb Space Telescope: optical telescope element," *Proc. SPIE* **5524**, 30-41 (2004).

[92] G. C. Cole et al., "An overview of optical fabrication of the JWST mirror segments at Tinsley," *Proc. SPIE* **6265**, 62650V-1 – 62650V-9 (2006).

[93] V. L. Krabbendam, T. A. Sebring, F. B. Ray, and J. R. Fowler, "Development and performance of Hobby Eberly Telescope 11 meter segmented mirror," *Proc. SPIE* **3352**, 436-445 (1998).

[94] D. A. H. Buckley, "The Southern African Large Telescope: an alternative paradigm for an 8-m class telescope," *New Astron. Rev.* **45**(1-2), 13-16 (2001).

[95] B. Lefort and J. Castro, "The GTC primary mirror control system," *Proc. SPIE* **7019**, 70190I-1 – 70190I-12 (2008).

[96] T. S. Mast and J. E. Nelson, "Segmented mirror control system hardware for CELT," *Proc. SPIE* **4003**, 226-240 (2000).

[97] G. Cortés-Medellín, "Active surface segmentation analysis of CCAT," *Proc. SPIE* **6267**, 62672X-1 - 62672X-11 (2006).

[98] C. Innocenti and V. Parenti-Castelli, "Direct position analysis of the Stewart platform mechanism," *Mech. Mach. Theor.* **25**(6), 611-621 (1990).

[99] J. C. Faugère and D. Lazard, "Combinatorial classes of parallel manipulators," *Mech. Mach. Theor.* **30**(6), 765-776 (1995).

[100] P. Nanua, K. J. Waldron, and V. Murthy, "Direct kinematic solution of a Stewart platform," *IEEE Trans. Robot. Autom.* **6**(4), 438-444 (1990).

[101] M. L. Husty, "An algorithm for solving the direct kinematics of general Stewart-Gough platforms," *Mech. Mach. Theor.* **31**(4), 365-380 (1996).

[102] K. Liu, J. M. Fitzgerald, and F. L. Lewis, "Kinematic analysis of a Stewart platform manipulator," *IEEE Trans. Ind. Electron.* **40**(2), 282-293 (1993).

[103] J.-P. Merlet, "Direct kinematics of parallel manipulators," *IEEE Trans. Robot. Autom.* **9**(6), 842-846 (1993).

[104] O. Didrit, M. Petitot, and E. Walter, "Guaranteed solution of direct kinematic problems for general configurations of parallel manipulators," *IEEE Trans. Robot. Autom.* **14**(2), 259-266 (1998).

[105] S.-K. Song and D.-S. Kwon, "Efficient formulation approach for the forward kinematics of 3-6 parallel mechanisms," *Adv. Robot.* **16**(2), 191-215 (2002).

[106] J.-P. Merlet, "Solving the forward kinematics of a Gough-type parallel manipulator with interval analysis," *Int. J. Robot. Res.* **23**(3), 221-235 (2004).

[107] E. Elliot, "Sensitivity of wavefront error to segment motions in the JWST primary mirror," STScI Technical Report JWST-STScI-002356 (2011).